2001

Studies of Ultrathin Magnetic Films Using Synchrotron Radiation: Resonant Photoemission, Circular and Linear Magnetic Dichroism.

Alexey Nikolaevich Koveshnikov
Louisiana State University and Agricultural & Mechanical College

INFORMATION TO USERS

This manuscript has been reproduced from the microfilm master. UMI films the text directly from the original or copy submitted. Thus, some thesis and dissertation copies are in typewriter face, while others may be from any type of computer printer.

The quality of this reproduction is dependent upon the quality of the copy submitted. Broken or indistinct print, colored or poor quality illustrations and photographs, print bleedthrough, substandard margins, and improper alignment can adversely affect reproduction.

In the unlikely event that the author did not send UMI a complete manuscript and there are missing pages, these will be noted. Also, if unauthorized copyright material had to be removed, a note will indicate the deletion.

Oversize materials (e.g., maps, drawings, charts) are reproduced by sectioning the original, beginning at the upper left-hand corner and continuing from left to right in equal sections with small overlaps.

Photographs included in the original manuscript have been reproduced xerographically in this copy. Higher quality 6" x 9" black and white photographic prints are available for any photographs or illustrations appearing in this copy for an additional charge. Contact UMI directly to order.

ProQuest Information and Learning
300 North Zeeb Road, Ann Arbor, MI 48106-1346 USA
800-521-0600

STUDIES OF ULTRATHIN MAGNETIC FILMS USING SYNCHROTRON RADIATION: RESONANT PHOTOEMISSION, CIRCULAR AND LINEAR MAGNETIC DICHROISM

A Dissertation

Submitted to the Graduate Faculty of the
Louisiana State University and
Agricultural and Mechanical College
in partial fulfillment of the
requirements for the degree of
Doctor of Philosophy

in

The Department of Physics and Astronomy

by
Alexey Koveshnikov
M.S., Moscow Institute of Physics and Technology, Russia, 1988
M.S., Louisiana State University, 1998
August, 2001

To my wife, Irina, and my sons, Ilya and Daniel

Acknowledgements

I am deeply grateful to my advisers, Professors Richard L. Kurtz and Roger L. Stockbauer, for their suggestion of this problem, for their close guidance and great patience, and for their editorial help during writing of papers and this dissertation. Their advice on research and writing skill has been quintessential for completing this work and will be inestimable to my future scientific career. I have benefited a great deal from their deep insight into physics, their experimental skills, their broad knowledge and from their numerous comments and suggestions on this dissertation.

Many thanks goes to the current and former members of the surface science group, Reginaldt Madjoe, Krishnan Subramanian, Roger Wendell, Xingyu Gao, Jeevananda Karunamuni, Alice Acatrinei, and Garry Mankey for many helpful discussions and shared ideas, for all the help they offered.

A special thanks goes to the staff of the Center for Advanced Microstructures and Devices (CAMD) and the staff of PGM Beamline at CAMD where most of my experiments were performed.

The technical assistance received from the physics department machine shop and electronic shop has been of great value.

I would like especially to thank my beloved wife Irina for her devoted support and understanding during the whole time of my graduate study here and to thank my sons for their great patience. I owe them all the time I did not spend with my family.

Table of Contents

List of Tables

List of Figures

Abstract

The work described in this dissertation is a study of the relationship between structural, electronic, and magnetic properties of ultrathin films of 3*d*-transition metals grown epitaxially on Cu substrate. The two systems that we have studied are films of fcc-Co on Cu(100) and Cu(111) and Fe and oxidized Fe films on Cu(100). Both systems are either employed or have potential applications in the data storage industry.

In order to provide information on the inter-relationship between the electronic structure and magnetic properties, we present results of magnetic dichroism observed in photoemission from the valence-bands and the shallow 3*p* core levels of ultrathin films grown on Cu. We have used both linearly and circularly polarized light from the Center for Advanced Microstrucutres and Devices (CAMD) synchrotron source and observe the angular distributions of the photoemitted electrons using a display type analyzer. Magnetic Circular Dichroism (MCD) and Magnetic Linear Dichroism (MLD) phenomena in UV and "soft" X-ray photoemission were observed in the core and valence-band structures of atomically thin Co/Cu(100), Fe/Cu(100) and Co/Cu(111). The patterns of the magnetic dichroism asymmetry in angular distributions of the photoelectrons in the valence-band photoemission will be discussed.

A broad array of techniques including ARUPS, constant initial state (CIS) resonant PES and STM were used to characterize Fe/Cu(100) interface oxidized at elevated temperature. The specific oxide phase, whether FeO(111) or Fe_3O_4(111) that forms depends on the initial Fe thickness. Both core level and valence band photoemission data will be presented. Difference spectra show that the interfaces of these films have a metallic density of states at E_F, unlike any of the bulk phases of iron oxide. Core level photoemission from Fe 3*p* levels shows the existence of two distinct Fe oxidation states. CIS resonant photoemission data show that the DOS close Fermi

edge can be identified as is mostly due to a contribution of iron oxide states, but not due to Cu states. MCD/MLD data suggest a significant degree of spin polarization at the Fermi edge and a presence of a surface magnetization for these films.

Chapter 1

Introduction

Progress in the semiconductor industry as well as in the magnetic data storage industry has been closely coupled with progress in surface science. In the 1970's new efforts to significantly reduce the sizes of devices required that new thin film technology be developed. At that time structures with lateral dimensions in the few micron regime were targeted. In the early 1980's the targets were in the sub-micron regime and efforts throughout the 1990's have made that a reality in commercial devices. The reduction in lateral dimensions requires an additional reduction in the thin film thickness, a parameter which has become under exquisite control through the development of several techniques. Current demands to reduce device sizes imply that structures on the nanometer scale be produced.

The computer industry has experienced rapid changes in the past few years as well, since the need to "stay connected" lead to a huge public demand for portable communication devices like very small laptops, palmheld PCs, etc. Current electronic devices such as compact camcoders, digital cameras, playback TV boxes, and the phenomena of software bloat demand additional data storage capacity. Furthermore, consumers demand that the storage industry provide these high capacity drives with a reduced form factor and shorter seek times. This demand has led to a dramatic reduction in the size but also cost of computer components

In part, this rapid development in magnetic hard drive sensor technology necessitates the need for new materials to be considered to accommodate these shrinking dimensions. In the past few years we have seen great developments in the field of magnetic thin films and multilayers, due to potential technical applications in magnetic devices such as magnetic RAM memories and sensors.

Magnetic properties of materials have long been the subject of studies of a substantial part of the physical science and engineering community, with understanding based on concepts arising from classical electrodynamics, and later quantum theory. This knowledge was used at the early days of the magnetic recording and following the common trend of miniaturization, data storage industry first tried to adopt "classical" approaches to reducing the data bit sizes.

Recently there has been a fundamental breakthrough in the technology of data sensing, due in part to achievements in surface science and multilayer film growth. This breakthrough was the discovery of giant magnetoresistance (GMR) in 1988 by Baibich *et al.*[1] in which quantum-well states that are locked into the now atomically-thin films produce novel new magnetic behavior. This effect was quickly used by the data storage industry to design a new generation of reading sensors which allowed them to increase storage density by two orders of magnitude just within the past five years. Although the fundamental mechanism for GMR is now generally understood, there remain many details of the behavior of these magnetic and non-magnetic multilayered structures which are not fully understood yet.[2, 3] Over the last decade, researchers found that depending on the thickness of the nonmagnetic spacer either ferromagnetic (FM) or antiferromagnetic (AF) coupling of magnetic layers are possible. This is due to the presence of the potential barrier between the magnetic/nonmagnetic interfaces. These barriers are closely localized spatially (~10Å) and interference from scattering off of this potential sets up a quantum well state in the nonmagnetic thin film. Depending on the phase of that state, it can induces either FM or AF coupling. Electrons traveling in the plane of the multilayer experience spin selective conductivity due to spin-dependent scattering at the interface. That is why studies of the electronic and magnetic properties of Fe/Cu and Co/Cu interfaces are of great importance.

During the past few decades many thin film deposition techniques such as molecular beam epitaxy (MBE), magnetron sputtering (MS), pulsed laser deposition (PLD) were developed and all of them require advanced vacuum technology. Some of these techniques, i.e. magnetron spattering, are routinely used in the semiconductor and magnetic storage industries. Others, due to their relatively high cost and lower throughput have limited manufacturing potential. Nevertheless, the success of techniques such as MBE at growing magnetic structures is based on the ability to epitaxially grow a wide variety of systems. A range of high quality metastable phases can be synthesized, as well as bulk phases with modified lattice parameters. The strain induced by epitaxial growth on a single crystal substrate also provides a way of stabilizing new crystallographic structures at room temperature. Bulk phase diagrams suggest that some of these structures can be achieved by applying a high pressure or temperature but by growing these artificial structures on surfaces we may find that they exhibit unique magnetic properties without having to resort to extreme conditions.[4]

The systems we are studying are ultrathin films of 3*d*-transition metals (Co, Fe) grown epitaxially on the *fcc* substrate (Cu). By growing thin magnetic films on non-magnetic substrate, we are able to study the evolution of the electronic and magnetic properties from sub-monolayer thicknesses all the way to thick films that exhibit bulk-like behavior. The structure and magnetic properties of these systems have been extensively studied but questions still remain due to the complicated surface phases that form. This study was expanded to include iron oxides grown on Cu(100) because of the practical importance of that system for industrial applications.

There are two main theoretical approaches invoked while describing thin film magnetism. The Heisenberg magnet model, which was used by number of authors, deals with stable magnetic moments resulting from localized uncompensated electron

spins.[5, 6] The interaction of these moments is dominated by exchange interaction. This model works well to describe magnetism in 3*d* metal oxides and 4*f* metals, but does not give a satisfactory description of the itinerant ferromagnets such as Fe, Co, and Ni.[7, 8] The Stoner model is restricted to the uncorrelated electron gas, as in Drude model of metals, in combination with exchange interaction in periodic potential. The ferromagnetic behavior occurs due to Coulomb repulsion between electrons of opposite spin, resulting in different density of states for spin-up and spin-down bands. The Stoner criteria for ferromagnetism is given by the expression:

$$J \bullet n_o(E_F) > 1 \qquad (1.1)$$

where J is the exchange constant and $n_o(E_F)$ is density of states at the Fermi edge.[8] The presence of the magnetic anisotropy can not be explained without taking into consideration spin-orbit coupling. The thickness dependent studies of Co/Cu(001) films show strong enhancement of the ratio of orbital to spin (itinerant) magnetic moments with reduced thickness (from ~8% to ~12%).[9]

The previous studies of Co/Cu(001) shows an almost perfect layer-by-layer growth except, for the first 2 ML when the deposited atoms tend to nucleate into three-dimensional islands, of *fcc* Co films.[10] STM studies of submonolayer coverages reveal some signs of surface alloying after been annealed to 180°C, but at room temperature there is no evidence for such behavior.[11, 12] These two elements are not miscible in the bulk and at the interface the small lattice mismatch, creates a tetragonal distortion of the grown film structure of ~4%. This favors the plane of the film as an "easy" axis for the magnetization direction and it has a strong four-fold in-plane anisotropy.[13] After about 8 ML there is observed a strong deviation from the *fcc* phase eventually reverting to *bcc*.[14] The system was extensively studied in the past by using PES techniques including ARUPS, inverse PES, etc.[15-17] A very interesting attempt to map the Fermi surface was performed by M. Hochstrasser, *et al.*

at Advanced Light Sorce (ALS) where the PES spectra were taken at 190 eV for the different emission angles and latter symmetrized to create FS contours.[18]

Co films on Cu(111) have been studied in the past with the following results. Up to two ML, Co films grow as a tetragonaly distorted *fcc* structure. Above 2 ML, it incorporates *hcp* stacking faults. By means of X-ray forward scattering and a CO titration it was shown that up to about 40 Å thick Co/Cu(111) the ratio of *hcp* to *fcc* phases is almost constant and close to 35%.[14] Similar results were observed on Co/Cu(111) superstructures grown on GaAs.[19]

One method to get spin-sensitive information on the electronic properties of these films is to use magnetic dichroism. Dichroism occurs when the electron excitation probability depends on the polarization of the incident photon. In general, it is a complex phenomenon that depends on the electron's initial state, the direction of the sample magnetization, the polarization of the light, and the electron's emission direction. In many cases, the effect can be simplified by selecting specific experimental geometries where the various vector quantities are either parallel or perpendicular and many of these geometries have been explored both experimentally and theoretically.

Theoretical descriptions of magnetic dichroism from solids are usually based on an atomistic approach and most models predict dichroism on an angle-integrated basis. Most predictions have been used to fit dichroism data in the XR absorption and core-level photoemission. As was pointed out by Venus [20], and to the best knowledge of the author, no angle-integrated data of the magnetic dichroism in valence-band photoemission has been published. This dissertation presents techniques that combine both angle-integrated energy distribution curves (EDC's) and angle-resolved PES to study the magnetic dichroism from the valence bands of ultrathin magnetic films. This work is unique in that it examines both the high symmetry *and*

low symmetry regions of the Brillouin zone. A similar approach was used to map asymmetry in the angular distributions in the valence-band photoemission from the non-magnetic TaS_2 [21] and we will extend this technique to magnetic systems.

Both Co/Cu(001) and Co/Cu(111) were studied in a variety of magnetic dichroism experiments including magnetic dichroism in the valence band photoemission.[22-24] The fact that the magnetic dichroism was reported in the geometry where both the atomic model and three-step model of PES predicts zero dichroism tells that we are still far from a complete understanding of this phenomenon.[25] This is the reason we have studied Co/Cu(001) and Co/Cu(111) with an instrument which allows us to combine both the advantage of ARUPS and angle integrated PES.

In addition to studying Co films, we have also investigated Fe films and their oxides since they are potentially useful in spin-dependent transport devices. Prinz [26] in a recent Science review article entitled "Magnetoelectronics" reported on how spin dependent transport can lead to more interesting devices and revolutionize the design of computational instrumentation. This conjecture is based on the potential development of materials that exhibit strongly spin polarized transport. Should the ability to build a device be developed, a new area of research and technology would arise called *'Spintronics'*. Spin-polarized transport will occur naturally for materials (like ferromagnets Fe, Co and Ni) in which there is an imbalance (40-50%) of the spin-population at the Fermi level due to the unequal filling of the bands.[26] The ideal type of material needed for spin-dependent transport will be a 100% spin-polarized conducting material. Half-metallic compounds are such materials, since they have only one spin orientation at the Fermi level. Two classes of materials that have been proposed to exhibit half-metallic behavior include the Heusler alloys (such as $Ni_{1-x}Mn_xSb$) and some oxides of transition metal elements, like CrO_2 and Fe_3O_4.[27]

The difficulty in using Heusler alloys in devices is that it is difficult to control the stoichiometry in thin films. Computations by Zhang and Satpathy in 1991 suggested that Fe_3O_4 is completely minority spin polarized at the Fermi level.[28] Early spin-resolved secondary-electron measurements by Alvarado *et al.* [29] observed a 40% spin-polarization in the empty states near the Fermi level. Other advantages of using Fe_3O_4 in devices is the fact that the Curie temperature is well above room temperature at 858 K and it also has a relatively high electrical conductivity of 100 $(\Omega\,cm)^{-1}$ at room temperature.[27]

Previous studies of ultrathin Fe layers on Cu(001) reported interesting structural and magnetic transitions occurring at different film thicknesses.[30 - 33] From 0 to about 5 ML the MBE-grown Fe films are ferromagnetic (FM) with a tetragonally distorted *fcc* structure, corresponding to an increased atomic volume of ~6%.[31, 32, 34] At 5 ML, there is a precipitous drop in the perpendicular magnetization, which is thought to reside in a "live" surface layer. From 5 to 11 ML the Fe film is undistorted *fcc* and, except for the surface "live" layer, is antiferromagnetic (AFM). For Fe coverages of more than 12 ML *fcc* Fe becomes unstable and transforms into the bulk FM *bcc* Fe.[31] Therefore, one goal of this work is to establish a link between the thickness-dependent structural and magnetic changes, and the electronic properties of the Fe/Cu(001) system.

The experiments described here were mostly conducted in an ellipsoidal-mirror analyzer that is described in Chapter 2. Prior experiments have shown that this instrument can produce images that reflect the contours of constant-energy electronic states. These contours are directly related to the band structures within the material's Brillouin zone. The only property of the electronic structure that is not available from such a measurement is the spin of the detected electron, and this is a particularly important property of our magnetic materials. Since this parameter cannot be

measured directly with the current 2D detector, we have used dichroism to provide this information.

Due to the design of the ellipsoidal-mirror analyzer, we are restricted to a limited selection of experimental conditions. For this reason, we are going to explore only two basic geometries of the magnetic dichroism experiment, longitudinal and transverse and we will investigate the influence of the light polarization on dichroic response. The detailed description of the experimental set up is given in Chapter 2. In part, some of our experiments were motivated by the desire to uncover the strongest dichroism response. The goal of our research was to study correlation of the structural, electronic and magnetic properties of ultrathin magnetic films, and their interfaces with their Cu substrate. In chapter 2, I will discuss the basics of photoemission spectroscopy as well as phenomena of magnetic dichroism accompanied by an outline of our experimental setup at the synchrotron. Chapters 3 and 4 will describe our studies of ultrathin films of Co deposited on Cu(001) and Cu(111) by mean of PES, magnetic linear and circular dichroism. Chapter 5 presents our data from thin (a few monolayers) Fe films, and oxidized iron films on Cu(001) substrate. The final chapter is a summary of our experimental studies.

Chapter 2

The Experimental Technique

The emergence of the semiconductor industry in late 1950's which was a great success of physics in general and helped to spur developments in both solid state physics and in materials and surface analysis. Due, in part, to their focus on phenomena within devices the focus of scientific research started to shift from phenomena in bulk materials to those in systems with reduced symmetry and dimensionality. This trend propelled the development of a number of new experimental techniques which deal mostly with properties of the surfaces, both structural and chemical. These techniques were combined with new theoretical descriptions and became known as the new scientific field of surface science.

Among the techniques developed to extract information on surfaces, photoelectron spectroscopy (PES) plays very distinct role. Initial experiments showed it to be quite successful in studies of exited states of atoms and molecules in the gas phase. Further developments showed that PES was a useful method to extract the electronic properties of both surfaces as well as extract the bulk electronic band structure of solids. In the early days of PES, scientists were limited in their choice of radiation source to conventional (He I, He II, Ne I, etc.) UV lamps or typical (Mg K_α or Al K_α) X-ray sources. In the 1970's, however, a new tool was developed – synchrotron radiation. This radiation provides researchers with a variable wavelength source of radiation in the range from about few eV to several keV. This opened the door to a number of different experiments identified in general terms by the photon energy used: ultraviolet photoemission spectroscopy (UPS) and X-ray photoemission spectroscopy (XPS).

This chapter describes the experimental method and instrumentation used in the photoemission research. Most of the photoemission studies were performed at Louisiana State University's (LSU's) Center for Advanced Microstructures and Devices (CAMD) synchrotron source. The uniquely designed display type ellipsoidal mirror analyzer (EMA) was used as an end station on the plane grating monochromator (PGM) beamline at the CAMD.[35, 36] The CAMD storage ring has a diameter of ~16.75 meters and consists of 8 bending magnets, each of which can accommodate two beamline ports. The bending magnet radius is ~2.93 meters, and the operating energy for the ring is 1.3-1.5 GeV giving critical wavelengths of ~ 4.85 Å and ~ 7.45 Å for two energies of and typical storage currents after electron injection are ~ 150-200 mA with lifetimes ~7-12 hours. Synchrotron radiation is produced when electrons are accelerated in a curved trajectory as occurs in the bending magnets of the synchrotron storage ring. The radiation that is produced is plane (linearly) polarized in the plane of the electron's orbit, and elliptically (circularly) polarized above or below the plane.

2.1 Photoelectron Emission Spectroscopy (PES)

Photoemission spectroscopy is based on the phenomenon of the photoelectric effect. The explanation of this earned Albert Einstein the Nobel prize in Physics in 1922. Einstein's formula for photoelectric effect can be written as following:

$$E_{kin} = h\nu - \phi \qquad (2.1)$$

where $h\nu$ is the incident photon energy and ϕ is the work function of the metal. The wavelength of the photon λ is related to its frequency ν through well-known relation: $\lambda = c/\nu$, where c is the speed of light. The energy E_{kin}, is the kinetic energy of the escaping electron, the work function is the energy needed by electron to overcome the potential barrier at the surface and propagate into the vacuum.

In the first half of the 20th century photoemission research was mostly concentrated on understanding phenomena related to the work function, as well as on developing materials with varying photocathode properties.[37, 38] By the 1960's, experimental techniques and the improvement of vacuum technology allowed Berglund and Spicer to obtain the first angle-integrated photoemission spectra from Cu and Ag. Their first data showed *d*-band edges at 2 and 4 eV respectively below the Fermi edge.[39, 40] Kane, in his breakthrough publication[41], showed that the band structure of solids could indeed be mapped by angle-resolved photoemission. In the early 1970's the ability to acquire angular distributions of photoemitted electrons led to the development of the powerful tool of angular resolved ultraviolet photoemission spectroscopy (ARUPS). This technique can be used to provide direct experimental information about the momentum dependent electronic bulk and surface band structure of materials. The schematic diagram of the photoelectron spectroscopy is shown in figure 2.1. The sample is irradiated with photons of a specific energy. The electrons in the solid absorb the photons and are emitted from the solid, if the photon energy exceeds the work function (ϕ) of the material (typically ~ 4 - 6 eV for most surfaces). The electron kinetic energies depend on their binding energy within the solid.

The relation between binding and kinetic energies of the electron is:

$$E_B = h\nu - \phi - E_{kin} \qquad (2.2)$$

where $h\nu$ is the incident photon energy, ϕ is the work function, E_B is the binding energy with respect to the Fermi level (E_F), and E_{kin} is the kinetic energy of the photoelectron relative to vacuum level.

The photoelectron detector (energy analyzer) measures the number of photoelectrons emitted within a narrow energy acceptance window. It accelerates the emitted electrons to a fixed energy called the pass energy in order to ensure that the

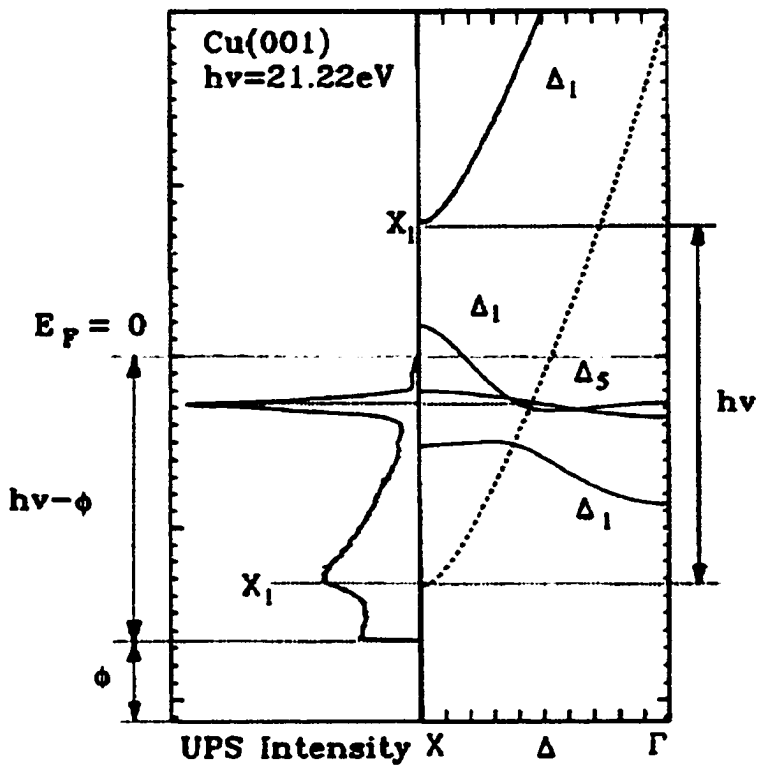

Figure 2.1 Band mapping by PES. Left panel shows PE spectrum in normal photoemission from Cu(001). In the right panel the the calculated band structure of Cu in XΓ direction shown in red. The black line corresponds to excited free electron like state.

detector resolution does not depend on the electron's original kinetic energy. The energy window that is selected determines the energy resolution of the analyzer. The total energy resolution is determined by both the analyzer resolution and by spectral characteristic of the source (in our case by the photon line width which is determined by the configuration of the beam-line).

The magnitude of the wavevector $\vec{k}$ (from momentum $\vec{p} = \hbar\vec{k}$) of the outgoing photoelectron can be determined by:

$$E_{kin} = \frac{\hbar^2 k_f^{\,2}}{2m} \qquad \text{or} \qquad |\vec{k}| = \sqrt{\frac{2mE_{kin}}{\hbar^2}} \qquad (2.3)$$

From equations (2.2) and (2.3) follows that information about the electronic levels of the valence band in a material $E(\vec{k})$ can be obtained by determining the momentum of the excited electron and its kinetic energy.

A photoelectron spectrum is a plot of the number of detected photoelectrons on the y-axis, as a function of their kinetic energy (or binding energy) along the x-axis. Energy distribution curve (EDC) is a term which is often used to describe this type of spectrum. An EDC can be compared to the occupied density of electronic states within the solid. The EDC is, in fact, the convolution of the density of states (DOS) and the Fermi function, coupled with the transition matrix elements for photoexcitation to the final state. The primary photoelectron peaks that are seen in the EDC originate from electron transitions from the various energy levels or bands that the electrons occupy. There are also additional peaks which are due to other processes such as Auger features resulting from the relaxation of an excited state, satellite peaks due to the many-body nature of the transition state, surface resonances, etc. These spectral features are all located on top of an inelastically scattered background of secondary electrons which also escape the solid.

Electron band mapping requires knowledge of not only the electron's energy, but also information about the electron's momentum. This information can be gathered from the angle that the electron is emitted from the sample surface. Obviously, it can be performed only on single crystalline samples, since polycrystalline material contains the crystallites of different orientations and will yield angle- or momentum- averaged spectra.

A three-step model is the most commonly used method to describe the photoemission process.[42] Several other models have been proposed, but here the discussion will be restricted to this one due to its simplicity. In this model, the photoemission process is separated into three independent steps:

(1) First step: optical excitation of an electron from the initial valence band state, $|i\rangle$, into a final unoccupied band state, $\langle f|$, within the crystal. Since the photon's momentum can be neglected compare to lattice momentum, only direct (or vertical) transitions are allowed. From first order perturbation theory the transition probabilities from the initial into final states are given by coupling the electron to the electric field,

$$P_{if} \propto |\langle f|\mathbf{A}\cdot\mathbf{p}+\mathbf{p}\cdot\mathbf{A}|i\rangle|^2 + |\langle f|\mathbf{A}^2|i\rangle|^2, \qquad (2.4)$$

where $\vec{\mathbf{A}}$ is the vector potential of the incident radiation and $\vec{\mathbf{p}}$ is the momentum operator. For photon energies in UV range, we can assume that the photon field varies slowly in space (at $h\nu = 30$ eV, $\lambda = \sim 400$Å, compare to interatomic distances of order ~3Å). In this case **A** may be treated as a constant, so the second term in equation 2.4 becomes zero. The commutativity of **A** and **p** is ensured, even without imposing **A** to be a constant, by choosing the Coulomb gauge. Now, the equation 2.4 becomes

$$P_{if} \propto |\langle f|\mathbf{A}\cdot\mathbf{p}|i\rangle|^2 \qquad (2.5)$$

because $\nabla \bullet \mathbf{A} = 0$, since **A** is constant. Equation 2.5 describes the photoemission process and the operator **A•p** is the dipole operator.

The final state |f> is uniquely defined by $\vec{k}$ and E (through equation 2.3).[43]. Furthermore, by combining this final state information with the photon's energy and polarization, one can derive important properties of the initial state, |i>. This will be illustrated in the next chapter.

(2) Second step: the propagation of the photoexcited electron to the surface/vacuum interface. Photon energies used in PES experiments normally range between 20 and 200 eV giving a light penetration depth of ~100 – 1000 Å. Though the photoexcitation process takes place within this depth but only the small fraction of excited electrons reaches the surface due to inelastic losses during electron-electron interactions. The sampling depth is limited by electron mean free path, λ, which is on the order of a few Å.

(3) Step three: escape from the solid into the vacuum. At this point the electron from inside the crystal passes trough the surface potential barrier and becomes a free electron outside the crystal. Boundary conditions imply that the wavevector component parallel to the surface be conserved while the normal component does not change.

The photoelectron's momentum, $\vec{k}_f$, may be decomposed into two components $k_f^{\parallel}$ and $k_f^{\perp}$ parallel and perpendicular to sample surface. If θ is the polar angle of the photoelectron's trajectory, measured with respect to the sample normal, then

$$k_f^{\parallel} = k_f \sin\theta \qquad (2.6)$$

and

$$k_f^{\perp} = k_f \cos\theta \qquad (2.7)$$

Since at the vacuum-solid interface, the parallel component of the momentum is conserved we can write for the parallel component of the electron's momentum inside the solid k_{in}.

$$k^{\parallel}_{f(inside)} = k^{\parallel}_{f} \tag{2.8}$$

Therefore,

$$k^{\parallel}_{f(inside)} = \left(\sqrt{\frac{2mE_f}{\hbar^2}}\right) sin\theta \tag{2.9}$$

The perpendicular component of momentum is not conserved as it encounters the potential barrier at the surface and this result in refraction of the electron as it escapes the crystal. Mapping this to $k^{\perp}_{f(inside)}$ is not as straightforward. The "free electron final state" model provides an approach to solving this problem [44]. This phenomenological model assumes that the final state to which the electron is excited in the first step of the three-step model, is one that disperses parabolically, despite of the calculated band structure. In this way, one can bring in the effect of the existence of the surface which is crucial in modeling photoemission. The excitation to a free electron like final state occurs within the solid. Figure 2.2 shows a schematic view of the free electron-like final state intersecting the *fcc* Brillouin zone along the ΓX direction as occurs in PES from (001) surfaces. The perpendicular momentum is reduced when passing through the potential barrier at the surface so,

$$k^{\perp}_{f(inside)} > k^{\perp}_{f} \tag{2.10}$$

and

$$k^{\perp}_{f(inside)} = \left(\sqrt{\frac{2mE_f}{\hbar^2} + V_o}\right) cos\theta \tag{2.11}$$

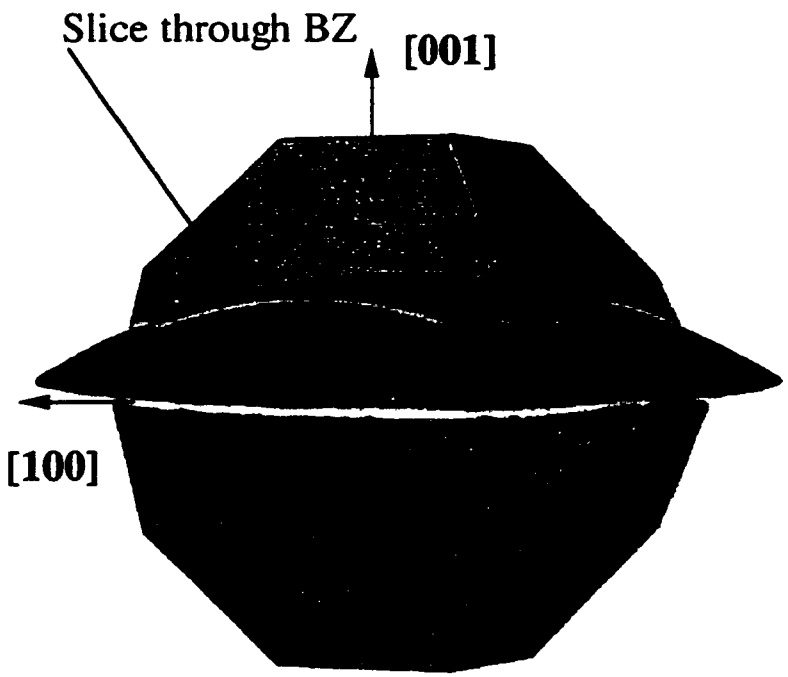

Figure 2.2 A schematic view of the free electron-like final state intersecting an *fcc* Brillouin zone along ΓX.

where V_0 is the inner potential, which usually refers to the binding energy of the bottom of the valence band in metals. For most materials it is an empirical parameter used to fit the data. Thus equations 2.9 and 2.11 are the central equations used to map electronic band-structures.

In order to study the spin-polarized band structure, one needs to be able to measure the photoelectron's spin orientation in addition to its energy and momentum, i.e. determine if the emitted photoelectron originated from a majority or minority band. The conventional and direct way is to use a spin detector which uses spin-orbit or Mott scattering to separately detect spin-up and spin down electrons.[45] This method, although direct, is difficult because of the extremely low count rates. In comparison with a typical spin-integrated measurement, a spin-resolved measurement deals with count rates that are about three to four orders of magnitude lower. New techniques have been developed in the past decade that probe the spin-dependent band structure in magnetic systems. Two of them are Magnetic Linear Dichroism (MLD) and Magnetic Circular Dichroism (MCD). These techniques are powerful tools to study magnetic properties, because, by studying the core levels of magnetic systems, one can combine magnetic sensitivity with element specificity.[46 - 48] However these may also be applied to investigate the valence bands of magnetic systems.[20, 22, 49, 50] This is the focus of my work.

2.2 Phenomena of Dichroism

In this section the phenomenology of the dichroic effects as well as experimental set up for magnetic dichroism measurements will be discussed.

Historically, the nomenclature of the dichroic effects is rather complicated and with multiple authors using differing notation, is sometimes rather confusing. For nonmagnetic systems, depending on polarization character of the incident light, the

terms of linear and circular dichroism (LD and CD) are widely used. Magnetic dichroism is the phenomenon related to the magnetic properties of materials and reflects the asymmetry in PES or XAS spectra due to decreased symmetry of the sample by the presence of a remnant magnetization or external magnetic field. It was predicted in the early 1980's and first observed by G. van der Laaan *et al.* in 1986 in X-ray absorption from rare-earth compounds.[51]. In this paper the authors call the technique "MXD" for magnetic X-ray dichroism. That is why the acronyms MLD (magnetic linear dichroism), MCD (magnetic circular dichroism), MXCD (magnetic x-ray circular dichroism), MLDAD (magnetic linear dichroism in photoelectron angular distributions), etc. are referred to for the different implementations of the magnetic dichroism. Gerrit van der Laan has contributed significantly to the description and classification of various dichroic phenomena.[52, 53] In his classification based on an atomistic approach to the photoemission from solids he introduced three main factors (moments) defining the symmetry of angular distribution in a core-level photoemission experiment. A schematic one electron picture for the angular dependence in polarized photoemission is shown in figure 2.3. The moments *a*, *b*, and *x* acting on the function of angular distribution $\mathbf{U}^{abx}(\mathbf{P},\varepsilon,\mathbf{M})$ in core-level photoemission are defined by light polarization **P**, direction of the photoemission ε, and the magnetization **M**. A generalized expression for the angular dependent photoemission $\mathbf{J}^a$ in the direction ε from an atom with a magnetic multipole along the direction $\vec{\mathbf{M}}$ may be written as:

$$\mathbf{J}^a(P,\varepsilon,M)=\frac{1}{4\pi}\sum_x I^x \sum_b \mathbf{U}^{abx}(P,\varepsilon,M)\sum_{cc'} A^{cc'}_{abx} R^c R^{c'} e^{i(\delta_c-\delta_{c'})} \qquad (2.12)$$

where $\mathbf{R}^c$ is the radial dipole matrix element and δ_c is the phase shift for excitation to the continuum state with orbital momentum $c = l \pm 1$. The indexes *c* and *c'* indicate the presence of more than one possible channel and the interference among them. The

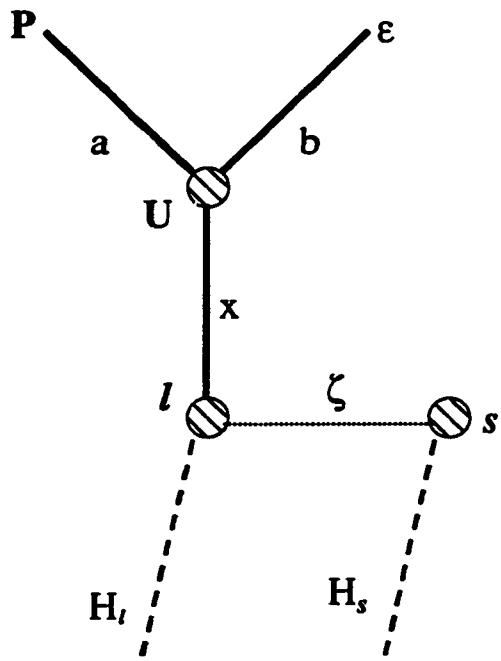

Figure 2.3 Angular dependence in photoemission $U^{abx}(\mathbf{P},\varepsilon,\mathbf{M})$ with spin-orbit interaction (ζ), orbit field (H_l) and spin field (H_s) acting on orbital momentum $\boldsymbol{l}$ and spin $\boldsymbol{s}$ of the electron along **M**. The light polarization **P**, the photoelectron direction ε, and the orbital momentum have moments a, b, and x respectively.

I^x gives the spectral intensity. For each I^x a limited number of angular distributions or "waves" U^{abx} with a numerical factor A for each channel can be produced. With this in mind the four different types of dichroism for core-level photoemission from *p* orbitals with circular (for two opposite directions of polarization, a=1) and linear (for two orthogonal directions of polarization, a=2) polarized light are summarized in the table 2.1 according to their symmetry. The spectra with prefix M can be also obtained by reversing the magnetic moment (x = odd).

Table 2.1 Classification of the dichroic effects in core-level photoemission from *p* orbital according to their symmetry in chiral (not complanar) geometry (after G. van der Laan).

Acronym	J^a	I^x	$A+b+x$	U^{abx}
MCD	J^1	I^1	Even	$U^{101}+U^{121}$
CDAD	J^1	I^2	Odd	U^{122}
MLDAD	J^2	I^1	Odd	U^{221}
LD	J^2	I^2	Even	$U^{202}+U^{222}+U^{242}$

It should be mentioned that this approach, although implemented quite successfully for core-level photoemission, is more than questionable in the case of valence band photoemission since it does not reflect the nature and symmetry of the electronic bands in a crystalline lattice field.

A slightly different approach for the classification of dichroism in the angular distributions of photoelectrons from surfaces was chosen by Venus.[20] His classification is based on the mutual orientation of the four principal vectors in the experimental geometry: photon momentum $\vec{q}$, emitted photoelectron momentum $\vec{k}$, sample magnetization $\vec{M}$, and normal to the crystal surface $\vec{n}$. The dichroism asymmetry is observed by the reversal of light helicity in the case of circular polarized light ($r \rightarrow 1/r$), ellipse ($\alpha = \beta - \gamma \rightarrow \beta + \gamma$) for two orthogonal planes of polarization of

linearly polarized light, or magnetization direction ($M \rightarrow -M$). Suggested nomenclature for magnetic dichroism in the angular distribution of photoelectrons after Venus is reproduced in the table 2.2. According to this author the change of light helicity by using photons above or below the synchrotron plane cause creates a superposition of two kinds of dichroism, both circular and linear.

Table 2.2 Nomenclature for magnetic dichroism in the angular distribution of photoelectrons (after D. Venus).

Acronym	Magnetic/ Nonmagnetic	Dichroism due to reversal of...	Polarization Sensitivity
CDAD	N	Helicity; $r \rightarrow 1/r$	CP
LDAD	N	Ellipse; $\alpha = \beta - \gamma \rightarrow \beta + \gamma$	LP
MCDAD	M	Helicity; $r \rightarrow 1/r$	CP
MLDAD	M	Ellipse; $\alpha = \beta - \gamma \rightarrow \beta + \gamma$	LP
MDAD	M	Magnetization; $M \rightarrow -M$	CP, LP, unpolarized
		Above/below sync. plane; $r \rightarrow 1/r$ and $\alpha = \beta - \gamma \rightarrow \beta + \gamma$	CP, LP

In the sense of this classification, the reversal of the magnetization direction is equivalent to the reversal of light helicity only in the case when $\vec{q}$ belongs to the mirror plane of the crystal. In order to obtain MLD or MCD, the MLDAD/MCDAD should be integrated over all possible $\vec{k}$.

Most of the experimental works on magnetic dichroism from the valence bands are focused on normal emission.[22, 54] Therefore, the analysis given by J. Henk and B. Johansson for magnetic dichroism in off-normal valence band photoemission is very important.[55] It is almost obvious that an arbitrary noncomplanar choice of $\vec{q}$, $\vec{k}$, and $\vec{n}$ will lead to some kind of dichroism, even for nonmagnetic materials. This

general case has a severe shortcoming: one does not learn much about the electronic states involved unless the measurement is coupled with more complete theoretical predictions based on band structure calculations. That is why the experimental geometry should be carefully examined to determine the key factors influencing the observed asymmetries.

In order to be self-consistent throughout the volume of present work and to avoid any misconceptions, it is very useful to specify terms we are going to use to denote different experimental geometries. For asymmetries observed in angle integrated valence band photoemission with circular/liner polarized light the acronym MCD/MLD will be used. Most of the time the dichroism observed was obtained by the reversal of the magnetization direction. Otherwise, it will be expressly specified. Two typical geometries were borrowed from the magneto-optic Kerr effect (MOKE) experiment: transverse and longitudinal. The schemes for these two experimental set ups with linearly polarized synchrotron radiation are shown in figure 2.4. A similar configuration was used with circularly polarized light. When we discuss the angular distributions in valence band photoemission with circular/linear polarized light, we will use the acronym MCDAD/MLDAD.

2.3 PGM Beam-Line at CAMD

The experiments were performed in an ultra high vacuum (UHV) end-station at LSU's Plane Grating Monochromator (PGM) beamline at CAMD.[56] A schematic view of PGM beam-line is presented in figure 2.5. It has two gratings, one with 360 and another with 1221 lines per mm designed to span the range from 20 eV - 1600 eV. The horizontal acceptance is ~ 7 mrad. The measurements presented here were all acquired using the lower energy grating with 360 lines per mm. The beamline may be operated at resolving powers of about 10^4, but for the purpose of higher count rates

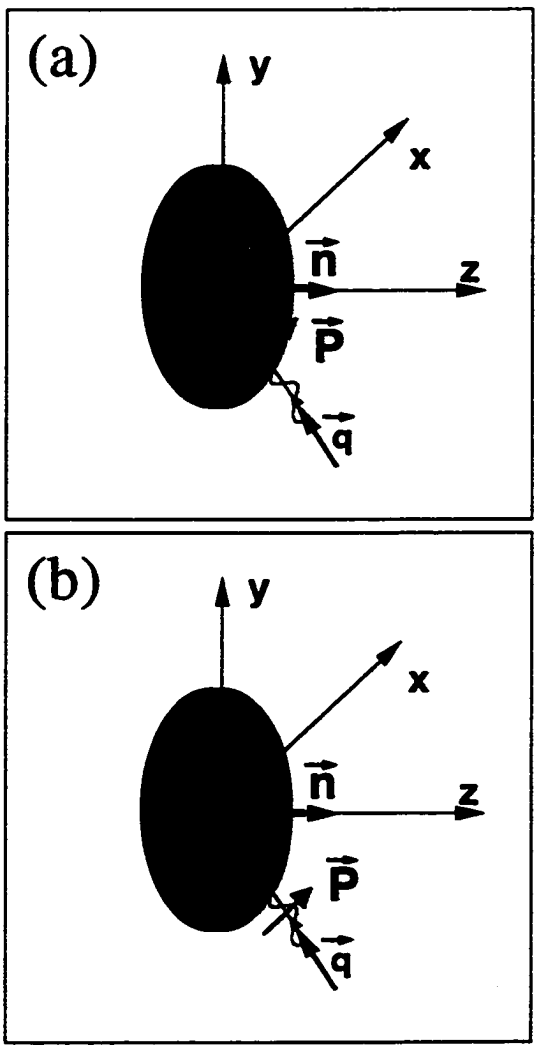

Figure 2.4 MLD experimental geometries: (a) transverse and (b) longitudinal. Vectors **P** and **q** belong to *XZ* plane.

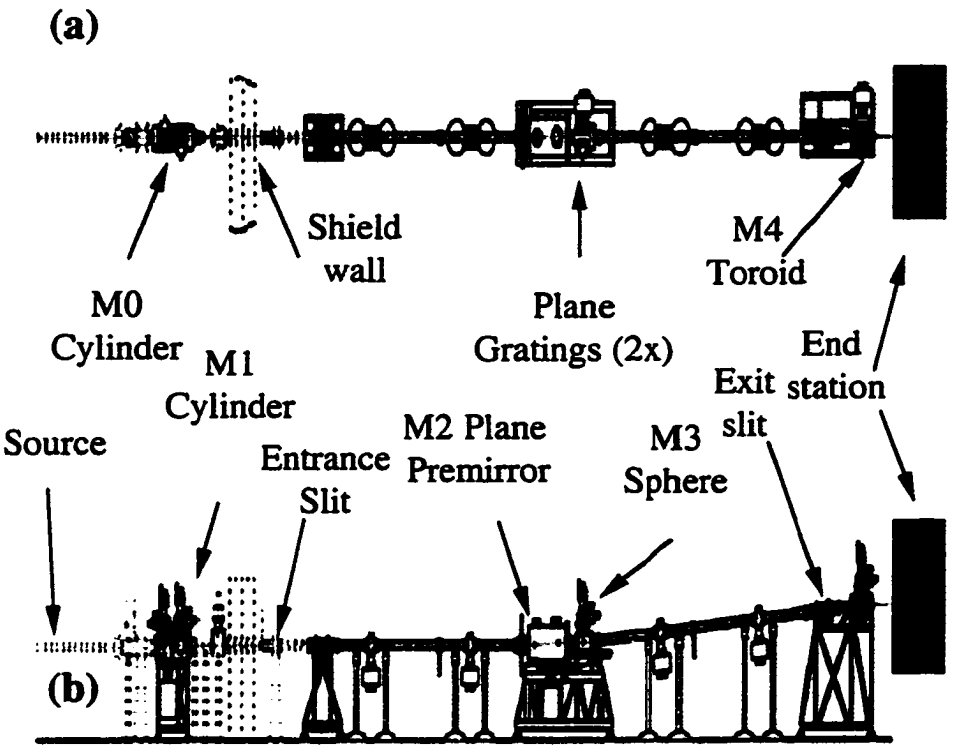

Figure 2.5 Schematic view of PGM beam line at CAMD LSU. (a) top view, (b) side view.

and better statistics, typical resolving power used here is ~ 800. The beam spot size at the end station was typically 0.5 mm. The PGM beamline was originally designed to accept the full vertical solid angle of light from the synchrotron storage ring delivering plane-polarized light to the user's end station. It was modified to access circularly polarized light from the synchrotron source by using water cooled Cu baffles to select light from above and below the plane of the synchrotron orbit. This way, left and right circularly polarized light could be obtained.

Calibration of the PGM beam-line was performed shortly after its installation at CAMD in 1994.[57] Still, each time before the start of an experimental run it is important to calibrate the photon energy and flux. The photon flux is measured with a tungsten mesh photodiode located just before gate valve G5 of PGM beam-line, which is immediately after M4 in figure 2.5. A plot of photon flux as a function of the premirror angle is shown on figure 2.6. Calibration of the photon energy in the range 20-100eV was accomplished by measuring the transmitted radiation through an Al foil filter that was placed in front the photodiode. The ionization thresholds for Al $2p_{1/2}$ and $2p_{3/2}$ are 72.5 eV and 72.9eV respectively. They are not resolved in our calibration procedure, so the average value of 72.7 eV was chosen. A much less intense absorption edge is observed at ~ 36.4 eV due to second order diffraction (i.e. when n = 2 in $n\lambda = 2d\mathit{Sin}\theta$, giving structure at a setting of 36.4 eV due to photons with half that wavelength or twice the energy (72.7 eV). Data for different premirror angles are shown in figure 2.7. Since the photon energy distribution depends strongly on the premirror setting we had to chose three fixed angles 77°, 80°, and 83° to get reasonable intensity in different parts of the spectrum. The energy calibration was performed using the Al absorption edges and angle corrections were applied in the EMA control software.

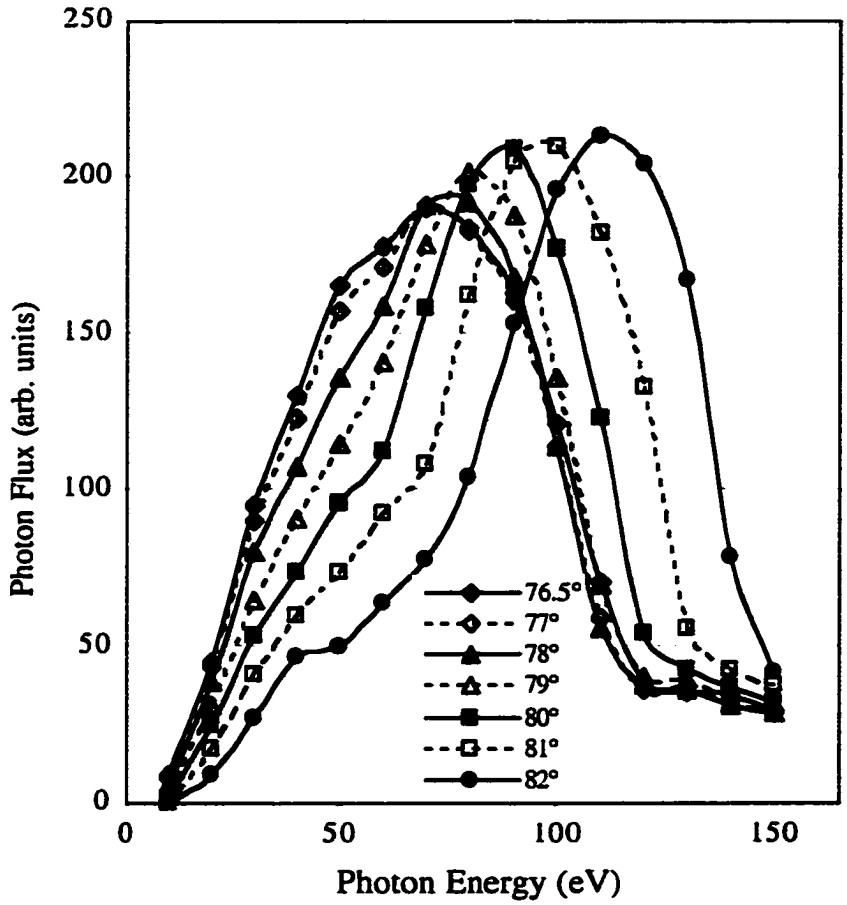

Figure 2.6 Spectral characteristic of the source. Photon flux *vs.* photon energy for different values of premirror angle.

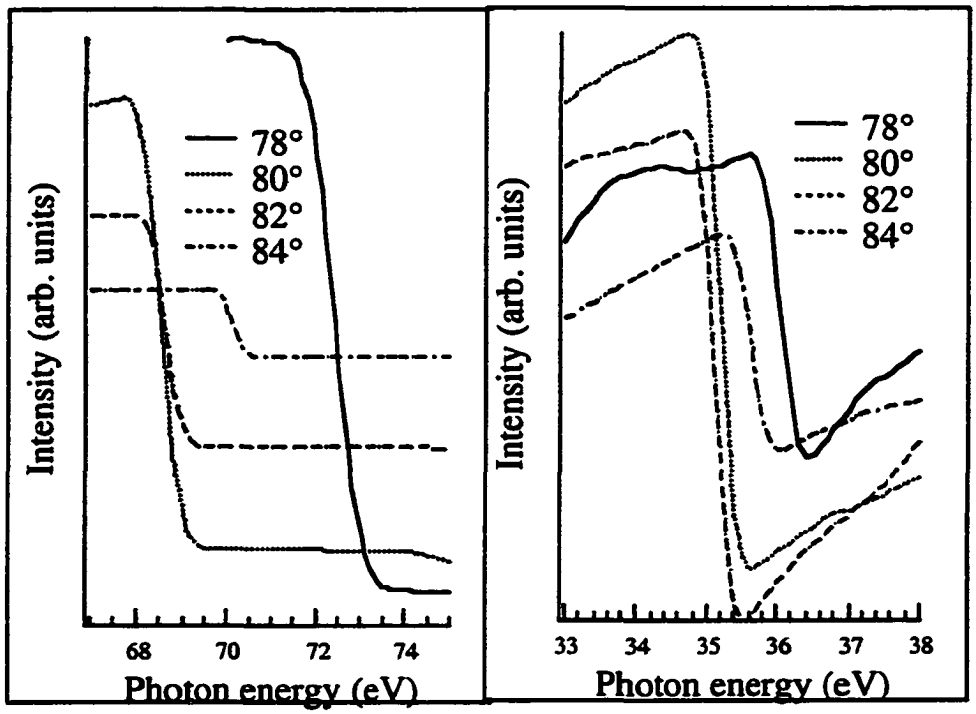

Figure 2.7 Calibration PGM beamline. Absorption of transmitted light by Al foil (a) $L_{II,III}$ edge, table value 72.7eV. (b) second harmonic at 36.4eV.

2.4 Ellipsoidal Mirror Analyzer (EMA)

An Ellipsoidal Mirror Analyzer (EMA) end-station is connected to the PGM through a gate valve and a bellows. A schematic view of the EMA end-station is presented in figure 2.8. This station consists of two chambers: a main ultra-high vacuum (UHV) chamber where the EMA is located, and a sample preparation chamber where we clean and prepare substrate surfaces and deposit films. The sample preparation chamber, which was designed in-house, is connected to the main chamber through a gate valve and houses all the equipment needed for cleaning of the crystal (sputtering and annealing) as well as our MBE source to evaporate Co and Fe films onto the Cu substrates. A magnetically coupled transfer arm allows the transfer of samples between the preparation and the main chambers. The isolation of the main instrument chamber from the film growth chamber prevents the coating of the delicate optics in the spectrometer and allows it to maintain higher vacuum than in the growth chamber. Both chambers are maintained in ultra-high vacuum.

The base pressure in the main chamber is typically below $1x10^{-10}$ Torr, and that in the preparation chamber was better than $3x10^{-9}$ Torr during film deposition. The EMA is magnetically shielded by 3 layers of μ-metal to reduce the influence of stray magnetic fields on the electron trajectories.

The ellipsoidal mirror is a display-type analyzer, which performs electron energy analysis while preserving the angle information of the photoemitted electrons. It is a very unique analyzer and only a handful of these spectrometers exist. The EMA was designed and built at the National Institute of Standards and Technology (NIST) by Stockbauer *et al.*[35] In this work, the EMA is used primarily for momentum resolved PES and the data is displayed as two dimensional images of photoelectron angular distributions.

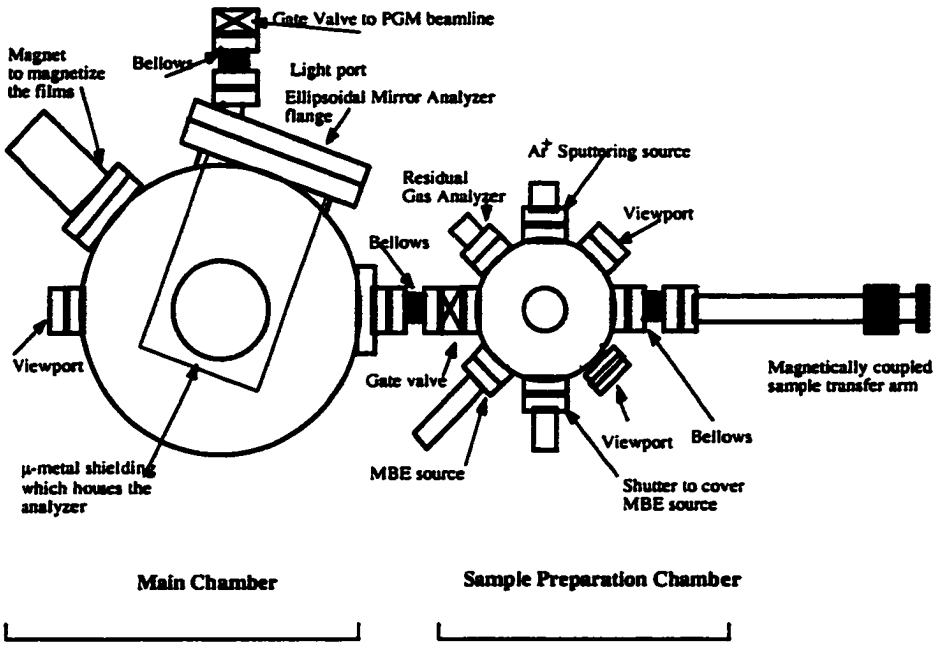

Figure 2.8 Schematic view of EMA end-station at CAMD.

Figure 2.9 shows a schematic of the EMA [35]. The heart of it consists of an ellipsoidal electrostatic mirror which has two focal points, with the sample placed at the first focal point. When illuminated with radiation, photoelectrons, emitted from the sample are selectively reflected off the mirror and are refocused at the second focal point, as is the property of an ellipse. A potential applied across G1 and G2 serves to retard/accelerate electrons to constant pass energy, giving a constant energy resolution for all kinetic energies. In our case the value for pass energy was usually set to 25 eV. The potential between the mirror and G3 acts as a low pass energy filter; i.e. it only allows electrons with less than a selected energy, to reflect off the mirror. The mirror will absorb the more energetic electrons. The grids centered on the other focal point (G4 – G6) act as a high pass energy filter and only allow electrons above certain energy to pass through. Thus, together, differetial energy analysis is achieved while keeping the angular information intact.

There may be minor distortions in the optics of this instrument. Most of the grids have a spherical curvature, and so always present a perpendicular surface to the electron trajectories. The three trajectories shown in figure 2.9 illustrate this. The mirror and G3 are the only components that have ellipsoidal curvature. The main source of the distortion is spherical symmetry of G6 and the planar geometry of G7. That is why the angular information close to the edges of acceptance window is less accurate compare to the central area. The electron detector consists of dual 5 inch microchannel plate arrays coupled to a resistive anode area detector. The anode is a uniform resistivity sheet with four contacts at the corners. A pulse of charge generated when a single electron enters the microchannel plates at any point on this detector produces a charge signal that is divided among the anodes. The amount of charge reaching each anode depends on the point of impact of the pulse. For example, equal signals at the four anodes imply that the pulse occurred in the center of the anode. The

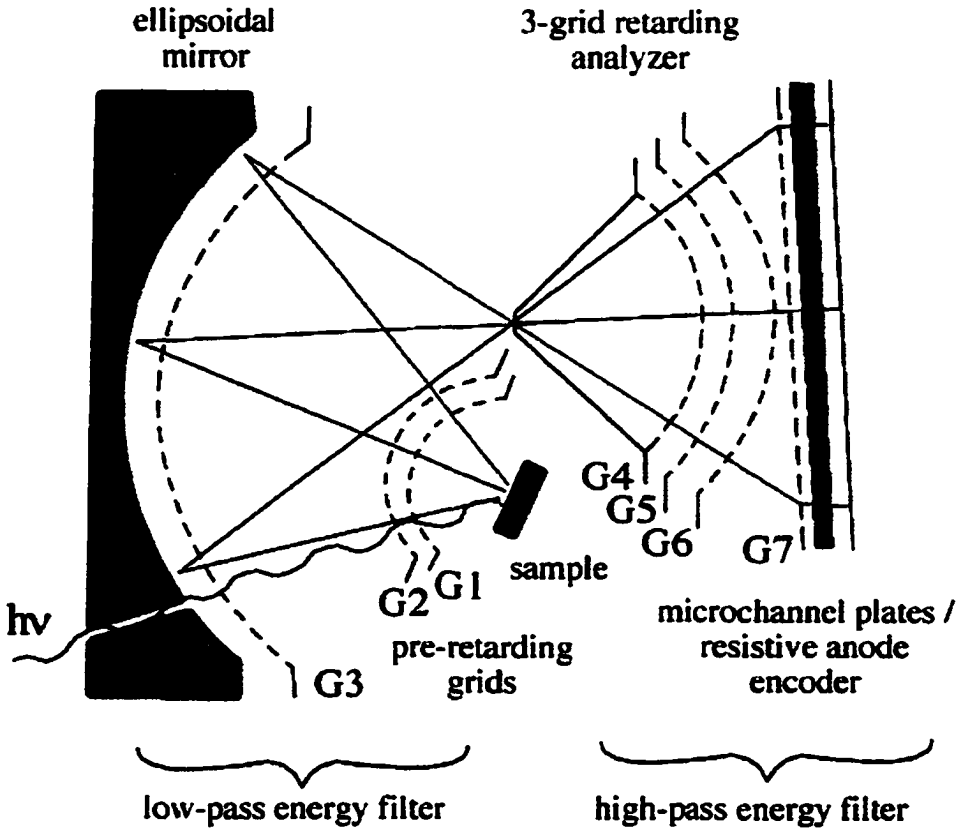

Figure 2.9 Schematic cross section of Elipsoidal Mirror Analizer (EMA).

actual X and Y position is decoded using a position computer (*Surface Science Labs*, now *Quantar Technologies*) which digitizes the position signal into a X-Y pair of 8 bit numbers and the images are displayed on the oscilloscope and a computer screen. The full width of the images corresponds to an angular acceptance of 64°. The typical angular resolution is better than 2°. The energy resolution of the instrument is ~ 200 meV for the settings we used.

A block-diagram of the EMA experimental set up is shown in figure 2.10. EMA control work-station sends control signals depicted by green arrows to the data acquisition hardware via a CAMAC interface crate and sets all required voltages on the grids of the EMA. It also communicates (blue arrows) to the PGM control work-station, which sets the premirror angle and the photon energy. Angle-integrated data are returned directly to the EMA control workstation and stored as EDC's. Angle resolved information from the position computer is collected by a separate image acquisition work-station through a digital PCI interface from *National Instruments*. The raw image data are acquired as 16 bit 256 × 256 images.

2.5 Interpretation of Angle-Resolved Photoemission Images

The free-electron final state model, described above, relates the angle at which the electron is emitted to the original $\vec{k}$-vector within the sample. This means that our image of the angular distribution is a measure of the locations in k-space where transitions occur. Since we image this at a well-defined initial state energy, our image can be related to a horizontal slice through the sample's $E(\vec{k})$, its band structure. In fact, this "horizontal slice" is actually a spherical slice through the Brillouin zone, as it shown previously in figure 2.2, with the radius of the free-electron spherical final state given by equation 2.3.

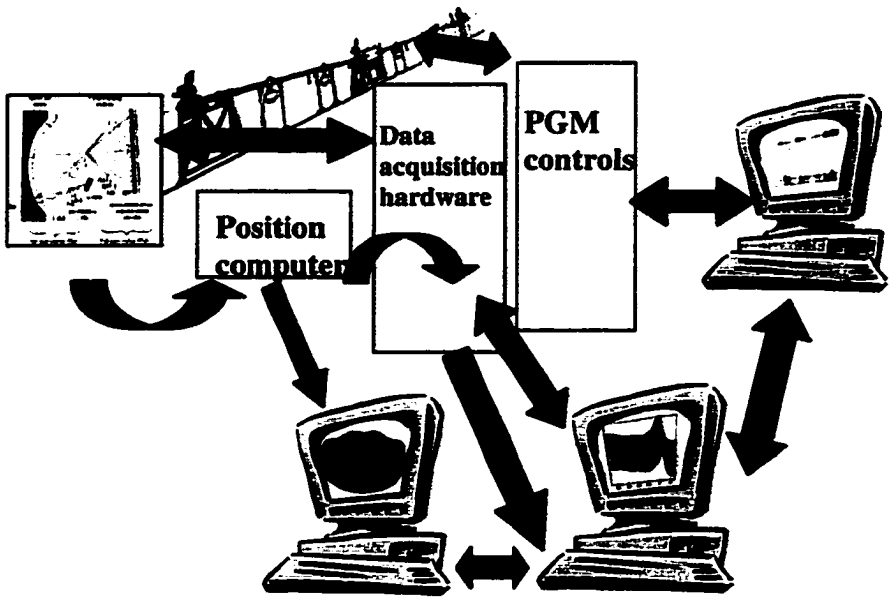

Figure 2.10 Block-scheme of the experimental set up.

Conventional hemispherical analyzers measure a spectrum at a fixed angle, and each peak in the spectrum can be identified with a single $\vec{k}$. The binding energy of a peak in that spectrum provides a single point on the band structure. Our imaging technique, however, provides a distinct advantage by sampling many k-values at a single constant initial energy. This is ideal when a constant energy surface such as a Fermi surface must be determined.

Figure 2.11 (a) shows calculated Fermi surface of Cu. Panel (b) represents actual PE data of the angular distribution from a Cu(001) surface at a photon energy of 90 eV. Image (c) is a cartoon of the Fermi surface of Cu [58] consisting of a nearly spherical surface in the *fcc* Brillouin zone (copper colored in center of image) that is connected to similar surfaces in adjacent zones through necks along the (111) direction. The large blue circle represents the free electron sphere corresponding to 90 eV photons. The intersection of this sphere with the Fermi surface is shown in a lighter shade. One would then expect to see a central intensity and four arcs corresponding to emission from adjacent zones as is seen in (b). The central feature in (b) comes from a cut through a sphere in the second Brillouin zone. The contours observed in the image correspond to the intersection of the free electron final state sphere with the constant energy Fermi surface.

Images like one shown in figure 2.11 must be corrected for non-uniformity in the gain of the channel plates and for variations in the transmission of the analyzer. This is done by taking a background image at an energy where there is no structure in the angular distributions such as on the secondary electron background. Dividing the raw data by this background results in the removal of the non-uniform gain, thus rendering the true angular intensities. This is the only correction that has been applied to any of the image data. The typical image normally takes 10-15 minutes to acquire with a similar time needed for background image.

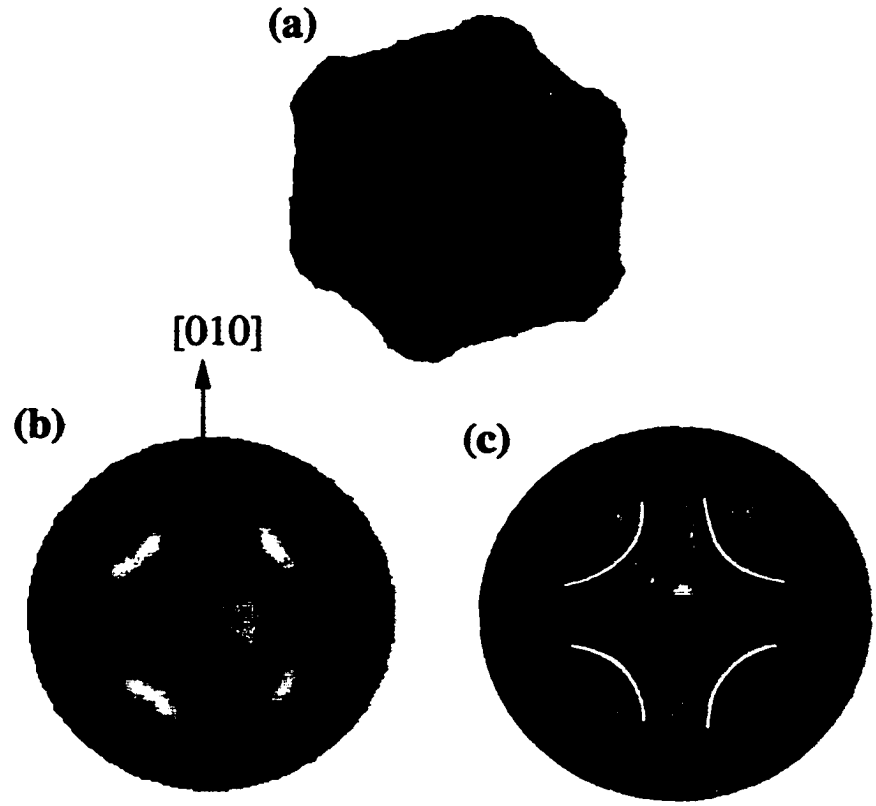

Figure 2.11 Fermi surface contours extracted in photoemission From Cu(001). (a) shows calculated FS of Cu, (b) angular distribution in PE from Cu(001) at hν=90 eV, (c) cartoon with ball model of Cu FS in extended BZ as cut through by a free electron sphere.

By changing the kinetic energy one can acquire images of the angular distributions in PE from different initial states. For example, at a binding energy of E_B=2 eV, one finds the top of the 3*d* band of Cu. Figure 2.12 (a) shows the calculated FS of Cu as seen along [001] direction, overlaid by a projection of 3D *fcc* BZ into the ΓKWX plane. The calculated constant energy surface for a binding energy of 2eV is shown in figure 2.12 (b). Figure 2.12 (c) shows data in PE with hν= 90 eV. To discuss polarization effects derived from the dipole approximation selection rules it is handy to use summarized table 2.3 (after [59]).

Table 2.3 Mirror plane selection rules according to the reference [59].

Mirror Plane	|f>	A•p	|i>	Intensity
(010)	even	even	even	yes
	even	even	odd	no
(001)	even	even + odd	even	yes
	even	even + odd	odd	no

For the experimental geometry when incident light is incident at 45° with respect to sample surface, and the reaction plane coincides with (010) mirror plane of the sample one can deduce the symmetry of the initial state based on the symmetry of the photoemission pattern. The final state, $|\,f\,\rangle$ has to be even under mirror plane reflection for emission in a mirror plane.[60] If the state is odd under reflection, then it acquires a negative sign and, therefore, must necessarily be zero. In other words one cannot have a node in the wavefunction at the detector. If we can say something about the symmetry of the photoemission operator, we can directly conclude the symmetry of the initial state. For emission in the (001) plane, the transition operator has even symmetry. This is because the vector potential, $\vec{A}$, has even symmetry under reflection about this plane. So, if emission is observed, then the initial states that give

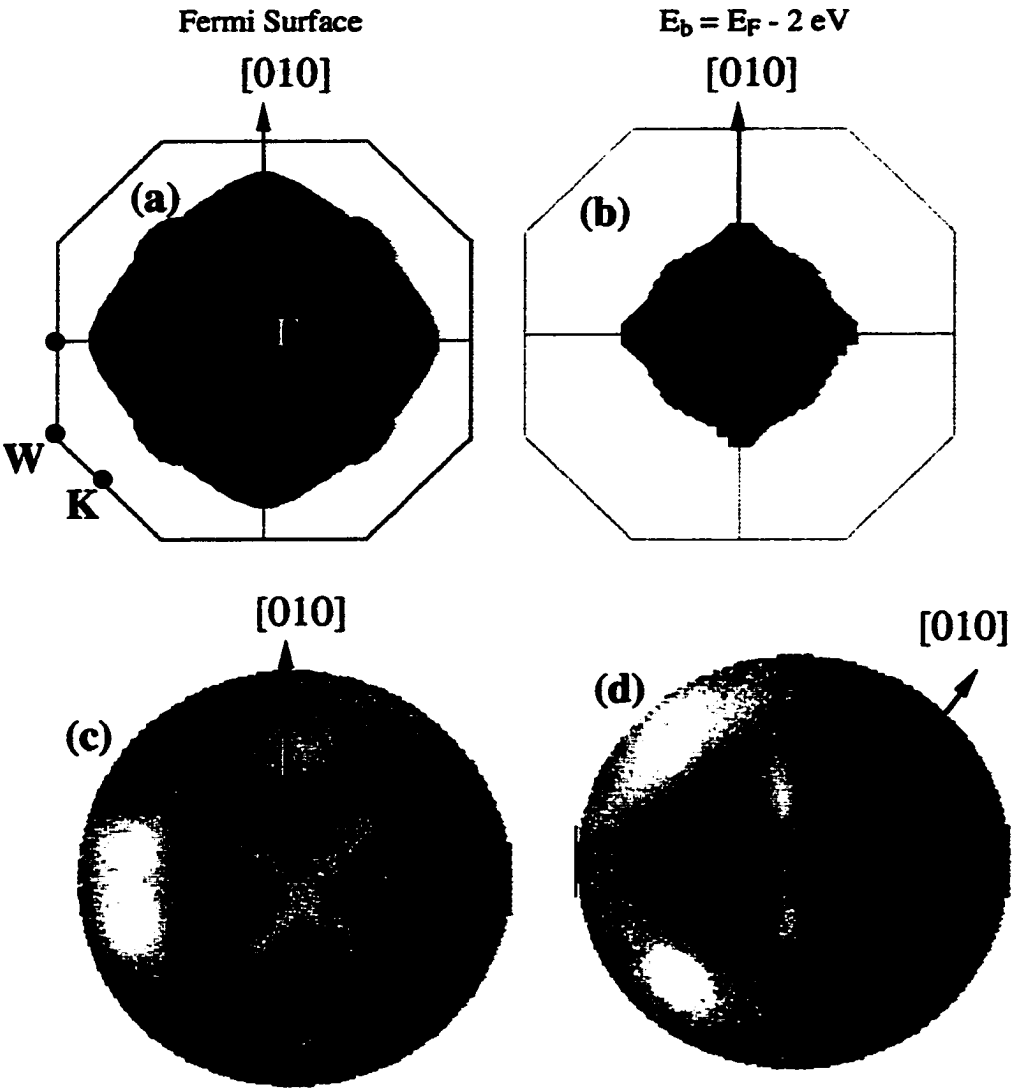

Figure 2.12 Panel (a) shows Cu FS as seen along [001] direction overlaid with a projection of 3D BZ into ΓKWX plane. (b) calculated isosurface for initial state E_F - 2.0 eV which corresponds to Cu 3*d* band. (c) and (d) data on angular distribution in PE from the constant energy surface in (b). Panel (d) emphasizes the role of polarization effect.

rise to this have to be even symmetry with respect to mirror plane reflection. If no emission is observed, then the initial state must have odd symmetry. In the case of photoemission in the (010) mirror plane, the emission operator has both an even and odd component. This is because the incident direction is at 45° to the sample normal, and we are dealing both with *s*- and *p*-polarized light. The component of $\vec{A}$ parallel to the sample normal is even under the reflection and the component perpendicular to the sample normal is odd under reflection. So, the emission from both odd and even initial states should be seen in this case. In a similar way the selection rules can be derived for the case when reaction plane coincides with (110) mirror plane of the sample (Table 2.4). The effect of polarization dependence may be illustrated by rotating the sample by 45°. These data are shown in figure 2.12 (d). One of the bars of the "X" in the middle of the image, which is parallel to the reaction plane, disappears, while perpendicular bar is clearly visible.

Table 2.4 Mirror plane selection rules for d_{xy} initial state in the experiment geometry when $\vec{A}$ is parallel to (110) plane

Mirror Plane	|f>	A•p	|i>	Intensity
(110)	even	even	even	yes
	even	even	odd	no
(110)	even	odd	even	no
	even	odd	odd	yes

Obviously, a change in the symmetry of surface should cause the symmetry change in the images of the photoelectron angular distributions. Figure 2.13 represents calculated FS of Cu as seen along [111] direction together with angular distribution taken from a Cu(111) surface. Panel (b) shows data at hν = 75 eV, and (c) at hν= 90eV. As shown above, the angular distribution pattern is very sensitive

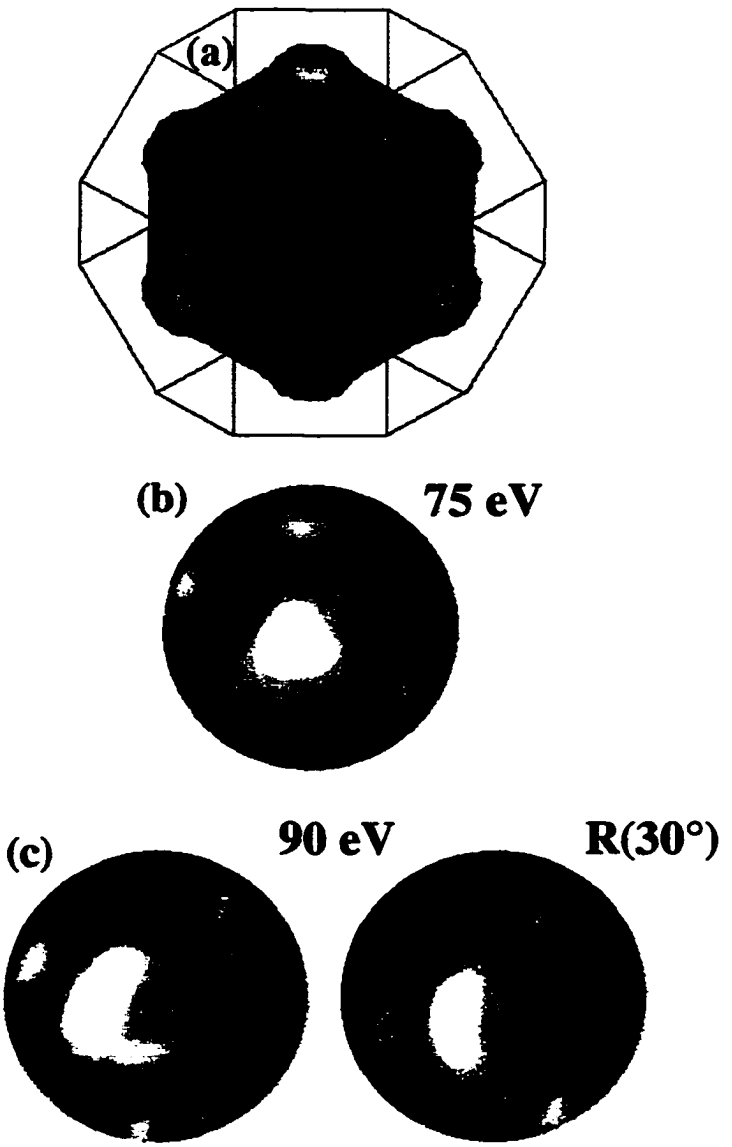

Figure 2.13 Angular distributions in PE from Cu(111). (a) calculated FS of Cu as seen along [111] direction. (b) FS contours at hν = 75 eV, and (c) at hν = 90 eV. Second image from panel (c) has been taken after sample rotation by 30°.

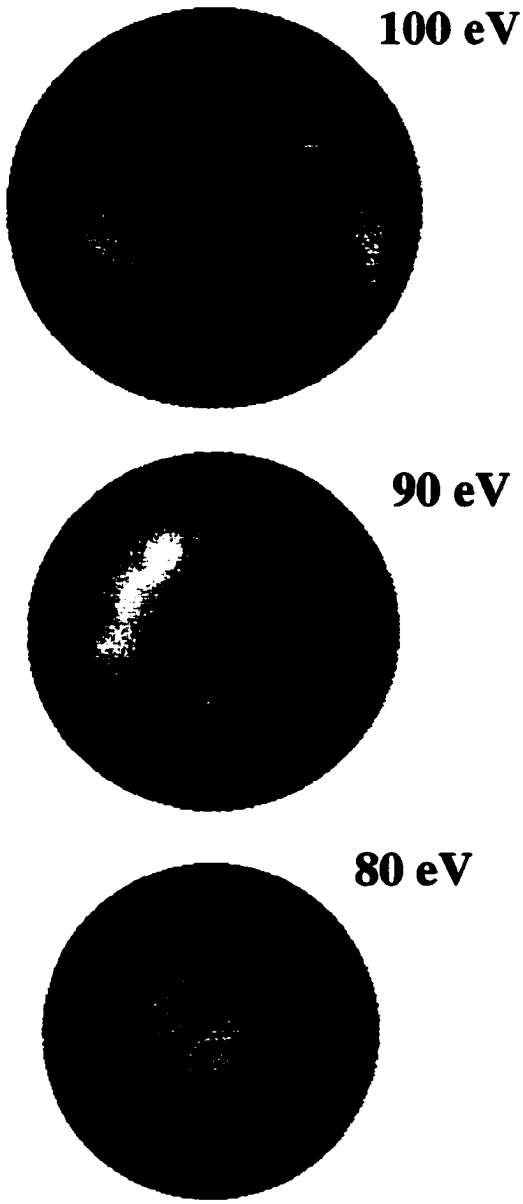

Figure 2.14 Imaging of the "neck" of Cu FS
in PE from Cu(111) by varying the photon energy.

towards the mutual orientation of the sample surface and the incident light polarization vector. This fact is illustrated in figure 2.13 (c).

For a fixed binding energy, say for a Fermi edge, by changing photon energy one can study the distribution of the bands through the BZ. In the case of Cu(111) this change will correspond to moving along the "neck" of Cu Fermi surface. Data on angular distribution in PE from Cu(111) at photon energies 80, 90, and 100 eV are shown in figure 2.14. The parallel component of $\vec{k}_F$ for specified energies can be measured directly.

Chapter 3

Thin Films of Co/Cu(001)

3.1 Introduction

For the past two decades structural, electronic and magnetic properties of 3*d* transition metals have been the subject of both experimental and theoretical research. The most studied of them are Fe, Co, Ni, and Cu. This fact can be easily explained by their importance in a variety of industrial applications. Furthermore, it is no longer surprising that the bulk properties of the materials differ significantly from those of thin films of the same materials. The "natural" crystallographic structure for Fe is body centered cube (*bcc*), for Co it is hexagonal closed packed (*hcp*), and Ni and Cu are face centered cube (*fcc*). The structure of thin films of these metals will depend on the substrate on which they are grown. Variables such as lattice parameter, ratio of surface free energies, conditions of film growth, immisibility of the film material and substrate, substrate roughness, etc. all play important roles in determining this structure.

Single-crystal Cu was chosen as a substrate for a number of reasons. First of all, Cu is well characterized by different techniques, including LEED, STM, PES.[61] Second, it has a lattice parameter (a=3.61Å) close to that of Ni (a=3.57Å), and *fcc* pseudomorphs of Co (a=3.55Å) and Fe (a=3.58Å), which provides a good lattice match between substrate and film. Being a noble metal, Cu is less reactive than other transition metals. And finally, which is the most important, since it is nonmagnetic, Cu allows the study of magnetic properties of films without strongly influencing them.

Co/Cu systems are of great interest since discovery of the phenomena of giant magnetoresistance, which was observed in Co/Cu multilayered structures.

3.2 Experiments

The studies of ultrathin films of cobalt on Cu monocrystals with (001) and (111) orientation where performed on the PGM beam-line at CAMD. The surface of the substrate was cleaned and ordered by multiple cycles of sputtering and annealing to 600°C in UHV conditions. Details of substrate preparation are described in Appendix A1. Films were deposited at room temperature in a side chamber by means of an electron beam-heated wire evaporator. The temperature of the crystal was monitored with a standard J-type thermocouple. The body of the evaporator was cooled by liquid nitrogen to maintain the base pressure in the side chamber in the 10^{-9} Torr range during deposition. For details see Appendix A2. After deposition, the sample was transferred to the EMA chamber where the experiments were performed. The thickness of the film was estimated by comparison of the intensities of Co 3*p* and Cu 3*p* as described in Appendix A3.

Energy distribution curves (EDC's) integrated over the acceptance angle of the analyzer (~0.71π sterad) were recorded for different values of photon energy. The pass energy was 25 eV and the energy window selected resulted in a resolution of ~200 meV.

It is known that Co films initially grow on Cu(001) substrate as an *fcc* pseudomorph, but very thin films undergo surface alloying, and some deviation from perfect epitaxial growth. After about 10-12 ML the films develop *hcp* stacking faults, and later grow as an *hcp*. In our studies we concentrated our efforts on growing mostly 8-10 ML thick films which have almost perfect *fcc* Co structure.

LEED studies of these films reveal long-range *fcc* structures. In figure 3.1 we show a set of LEED patterns taken from 8 ML Co/Cu(001) for different values of incident electron energy. In the 132 V image LEED spots are labeled in 2D notation

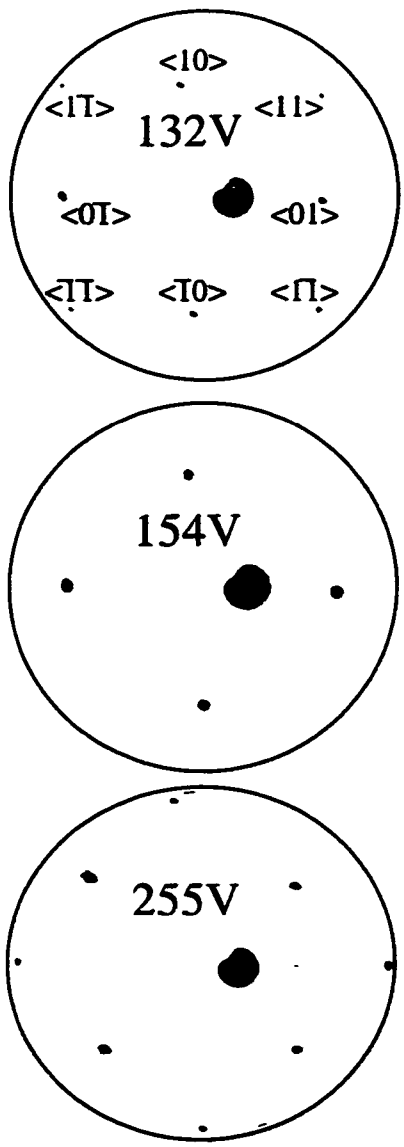

Figure 3.1 LEED patterns of 8 ML Co/Cu(001) film taken at different electron energies which reveals its *fcc* structure. Distortion from square is due to angular distortion close to the edge of LEED screen, and due to parallax between CCD camera and LEED optics. Bright spots in the center of images are due to light emission from the back side of the electron gun.

according to their order. One can see that the intensities of spots located along the projections of main axes into Ewald sphere are brighter than the higher-order spots. With a slight increase in electron energy, those spots are almost disappearing. At higher energies, the pattern contracts and we clearly see those and higher order spots along main axes. These patterns are in excellent agreement with LEED data for *fcc* structures obtained elsewhere.[17]

3.2.1 Resonant Photoemission

Figure 3.2 shows a typical set of EDC's taken from ~12 ML Co/Cu(001) sample as a function of photon energy. By changing the photon energy we increase the perpendicular component $\vec{k}_{\perp}$ of outgoing photoelectron and thereby sample different regions of the Brillouin zone. The spectra are aligned with respect to Fermi level and offset in the vertical direction for easy visualization. At 60 eV the shape of the spectrum is differs substantially from those taken at lower photon energies. This is due to photoemission resonance. This phenomenon is known as a resonant enhancement in photoelectron emission and was reported for Co by Weaver.[62] Further studies by Barth *et al.* in the mid 1980's characterized this process in a number of transition metals.[63] This resonance occurs when the photon energy is high enough to "knock out" one of the core electrons. Due to electron-core hole interactions an electron from the valence band can resonantly decay into the 3*p* level and energy is conserved by emission of an electron in an Auger-like process. Another words, an additional channel for electron emission has opened up for photon energies just exceeding the 3*p* excitation threshold. Schematically, ordinary photoemission process can be described by equation 3.1, while occurrence of the extra channel follows equation 3.2:

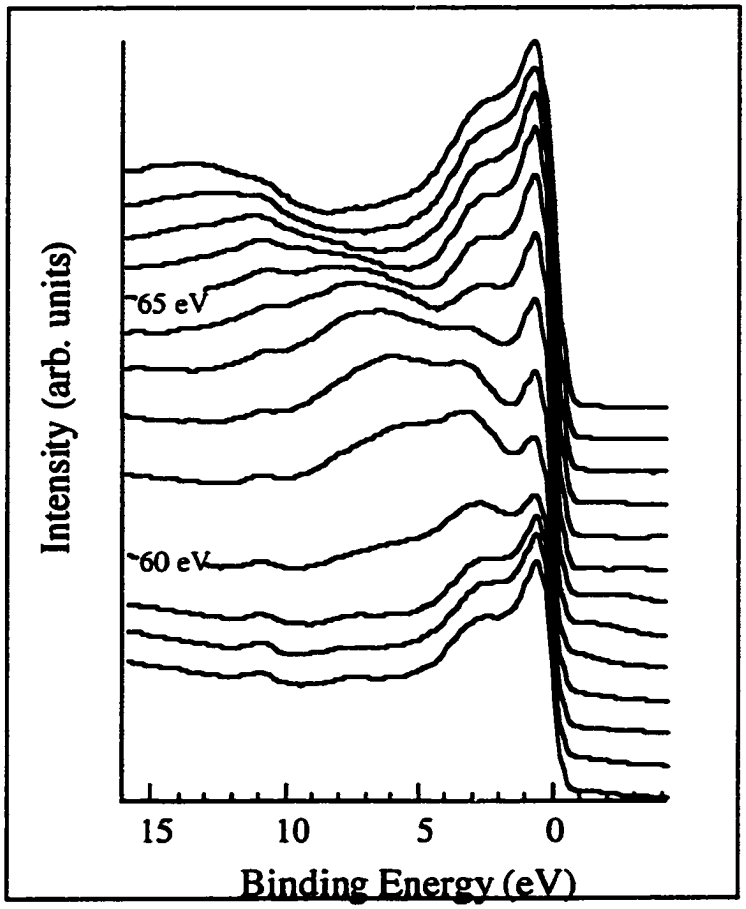

Figure 3.2 Resonant enhancement in valence band photoemission from ~12ML Co/Cu(001). At the 3*p* excitation threshold, an additional channel for *d*-electron emission becomes available resulting in satellite peaks as well as normal Auger processes. EDC's were taken with 1 eV step size in photon energy.

$$[Ar]3d^7 4s^2 + h\nu \rightarrow [Ar]3d^6 4s^2 + e^- \quad (3.1)$$

$$[Ar]3d^7 4s^2 + h\nu \rightarrow ([Ne]3s^2 3p^5 3d^7 4s^2 + e^-)^* \rightarrow [Ar]3d^6 4s^2 + e^- \quad (3.2)$$

In the intermediate excited state, the e^- can reside in a *d* state or another nearby Rydberg level.

Resonant photoemission allows one to extract extra information about the electronic structure of a sample. Excited states, core-hole lifetimes, and *d*-electron correlation energies, which are not available from PES data, can be obtained. In our studies of magnetic dichroism in the valence band PE we did not want to complicate overall pattern by necessity to consider these interactions and we have chosen photon energies well below the 3*p* core level excitation threshold.

Figure 3.3 (a) presents photoemission spectrum from the same 12 ML Co/Cu(001) taken at a photon energy of 45 eV. The dotted line is for Shirley-type spline background, and dot-dashed line shows the spectrum with the background subtracted. Panels (b) and (c) of this figure are calculated total, minority, and majority densities of states for *hcp* and *fcc* Co respectively. The ratio of PES intensity at the maximum of 3*d* band, which is located about 0.7 eV below Fermi level, to background intensity is higher for the thick film (*fcc-hcp*) than for the thin *fcc* film. This is in agreement with calculated DOS. The presence of a visible feature in spectrum at a binding energy of 1.5 eV is not present in calculated *hcp* DOS; it clearly indicates the presence of the *fcc* phase.

Angle integrated photoemission spectroscopy provides the best comparison with computed densities-of-states but even this method has its limitations. At different photon energies, one is sampling different regions of the Brillouin zone, which can affect the spectral line shape. Furthermore, the photoexcitation matrix elements will depend on photon energy as well, making quantitative comparisons difficult.

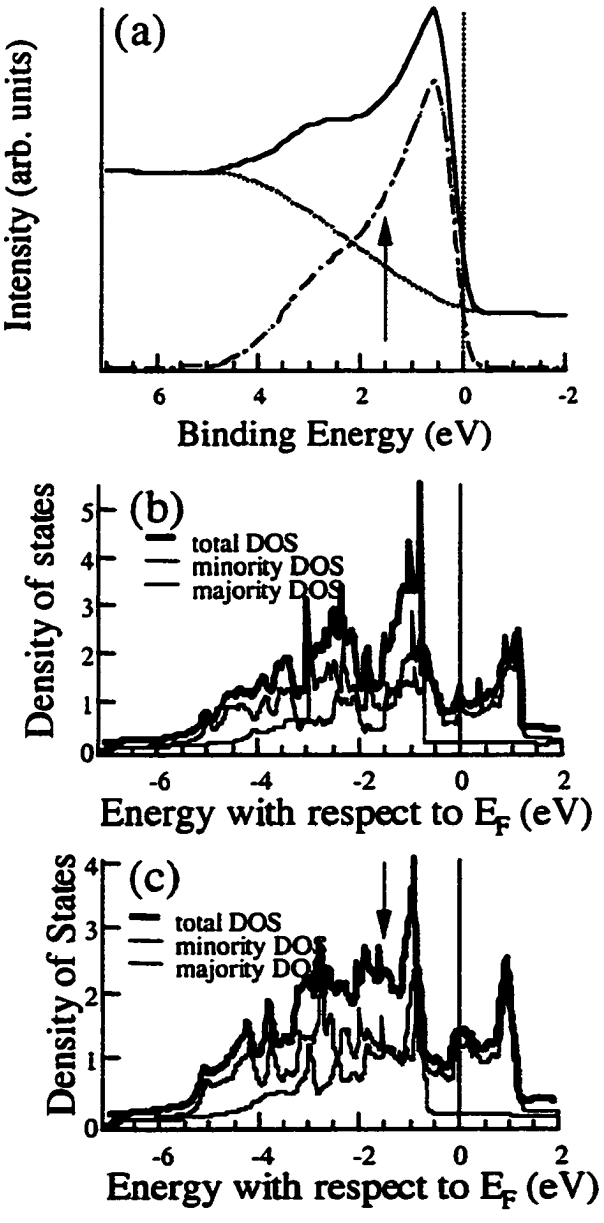

Figure 3.3 Photoemission spectrum from 12 ML Co/Cu(001) taken at hν = 45 eV (a). Solid line represents raw data, dotted line is a spline Shirley type background, and dash-dotted one stands for the difference. (b) shows calculated DOS for *hcp* Co, and (c) for *fcc* Co.

We can make quantitative comparisons if we measure the angular distributions of the photoelectron spectra. In this case, each $\vec{k}$ vector can be identified and if a Mott-type detector is used, the spin state can be determined as well. The photoelectron angular distributions from Co films on Cu(001) are discussed in the next section.

3.2.2. Angular Distributions in Valence Band PES from Co/Cu(001)

In contrast with angle-integrated spectra, our technique of imaging of photoelectron distributions preserves angular specific information. Therefore, in this case we are dealing with angular resolved photoelectron spectroscopy (ARPES). Figure 3.4 shows calculated Fermi surfaces for majority band electrons (a) and minority band electrons (b) of bulk *fcc* Co as they seen along [001] direction. These calculated surfaces will be helpful in the future while discussing patterns in angular distributions of the photoemitted electrons.

Previous studies of angular distributions in photoemission from bulk Cu(001) [58] and from Ni/Cu(001) films [64] provided a good background for this study of *fcc* Co surfaces. In figure 3.5 we show an EDC taken with linearly polarized light with hν = 45 eV from ~3.25 ML Co/Cu(001). This photon energy corresponds to a $\vec{k}$ value which, in the center of the image, samples the Γ point of second Brillouin zone (BZ).[59] The light is incident at the angle of 45° with respect to sample normal and the $\vec{A}$ vector is in the horizontal plane. The inserts are images of the angular distributions in PES for two different values of binding energy. The top image taken at E_b = 2.3 eV is the angular distribution from the 3*d* bands of Cu. The bottom image taken at E_b = 0.25 eV corresponds to the 3*d* bands of Co. The center of the images corresponds to the Γ point of the BZ, while left, right, top, and bottom of the images correspond to the intersection of BZ by free electron sphere between X and W points.

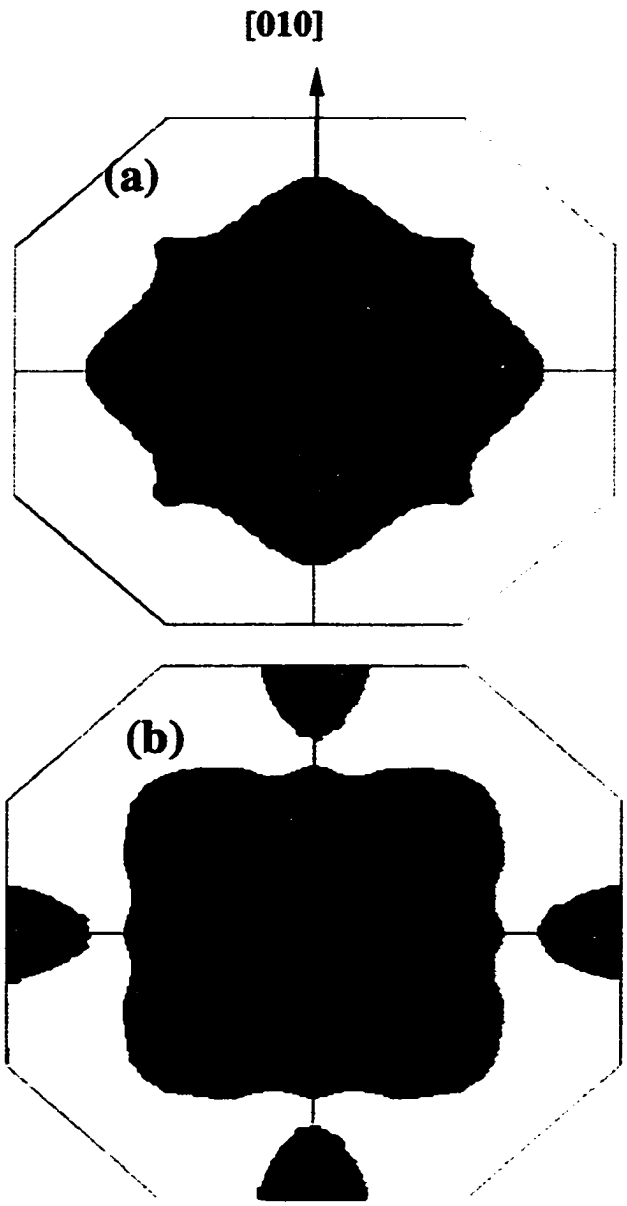

Figure 3.4 Calculated Fermi surfaces for *fcc* Co. Panels (a) and (b) show majority and minority electron isosurfaces as seen along [001] direction. Green contours represent *fcc* BZ.

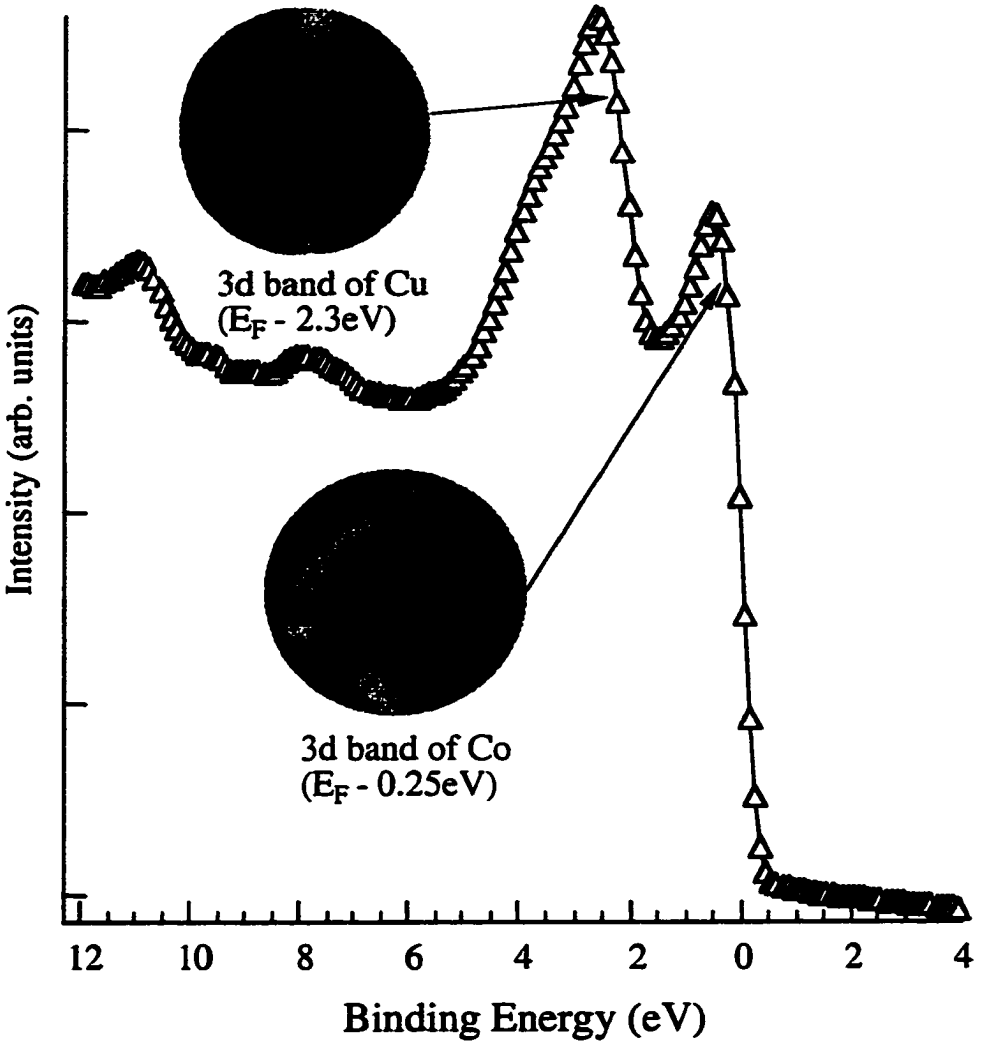

Figure 3.5 EDC for ~3.25 ML Co/Cu(001) at photon energy hν = 45 eV. The top image corresponds to the *3d* bands of Cu, taken at E_F -2.3 eV binding energy, the bottom image is the *3d* band of Co, taken at E_F -0.25 eV binding energy.

One can see that these images are very similar which is a consequence of both Cu and Co having the same *fcc* crystalline structure. Still there are some differences. First, the "half diamond" on the left side of the images is larger for Co than for Cu. Also, the "circular" features at the corners of the diamond in Cu are almost absent in Co; instead we see a distinct "gap" in the left corner for Co. In addition, the emission intensity in the center of image from the Co 3*d* band shows a partial cross-like feature, which is absent in Cu. This is due to the fact that Cu atom has filled 3*d* orbitals of the M shell while Co has 3 uncoupled vacancies. The electronic structure of the Cu atom is $[Ar]3d^{10}4s^1$, compare to that of Co $[Ar]3d^7 4s^2$. Therefore, the 3*d* e_g-component ($d_{x^2-y^2}$, d_{z^2}) in the total DOS for Cu has a lower value than the corresponding component for Co at measured values of binding energies.

As mentioned previously, the angular distribution of the photoelectron depends on symmetry of initial and final states, and the relative orientation of $\vec{E}$ ($\vec{A}$) vectors of incident light with the crystallographic direction of the sample. One must be careful in interpreting the intensities of these images, since even a small change in alignment of the crystal with respect to the analyzer and the polarization vector of the light will give noticeable changes in intensity. As was mentioned before, the reaction plane is the plane defined by vectors $\vec{q}$ and $\vec{n}$, where $\vec{q}$ is a momentum of incident photon, and $\vec{n}$ is the normal to the sample surface. The crystal surface (001) has C_{4v} symmetry. Due to polarization effects and offnormal photon incidence, the photoelectron distributions from this surface, in the case of [110] or [001] alignment of the sample, parallel to the reaction plane, has reduced C_{2v} symmetry. Therefore, a rotation by an arbitrary angle, which does not belong to the surface point group symmetry operation, will produce a pattern of reduced symmetry in the photoelectron distribution. An illustration of this effect is shown in figure 3.6 where the sample was rotated by 12°. Panel (a) shows the angular distribution in photoemission from the Fermi edge of 8ML Co/Cu(001) with

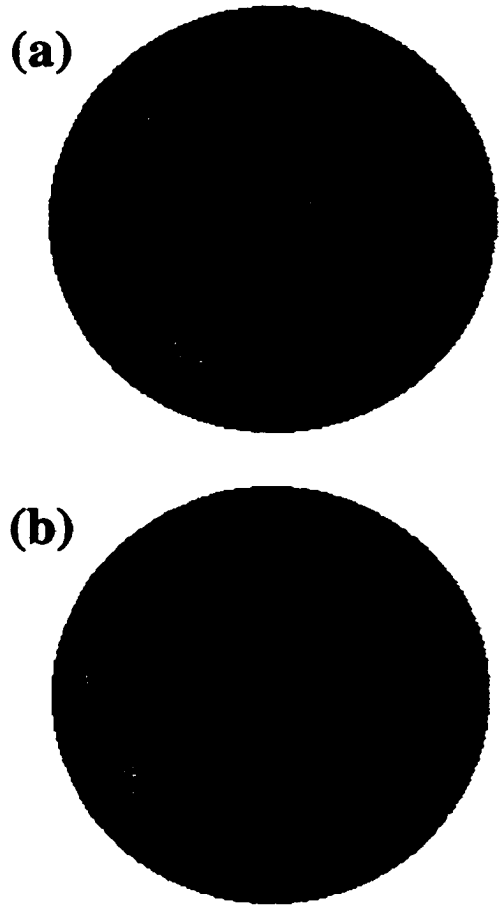

Figure 3.6 Effect of sample rotation with respect to reaction plane. Top images show angular distribution of escaping photoelectrons in PES with linearly polarized light (hν = 45eV) from 8 ML Co/Cu(001) while (a) sample is aligned, and (b) rotated by ~12°.

linearly polarized light (hν = 45 eV) when the [001] axis of the sample is parallel to the reaction plane. Panel (b) of this figure is an angular distribution in photoemission from the same sample under the same conditions except the sample was rotated by ~12° in the plane of the image. In the case of parallel alignment of the reaction plane and crystallographic axis of the sample, the image of angular distribution is symmetric with respect to reaction plane, in this case, the horizontal plane. The left-right asymmetry in (a) is a consequence of the 45° orientation of $\vec{q}$ with respect to $\vec{n}$, giving a combination of *s*- and *p*-polarized light. Even though the initial and final states remain the same in figures 3.6 (a) and (b), the probabilities of $|i> \rightarrow <f|$ transition are different due to the difference in the alignment $\vec{A}$ vector with sample axes.

A photoemitted (free) electron, in the first approximation, can be described as a sphere in reciprocal space with a radius of

$$|\vec{k}| = \sqrt{\frac{2E_{kin}}{m}} \qquad (3.3)$$

where E_{kin} is a kinetic energy of the electron and m the mass of the electron.

By increasing the photon energy, the photoemitted electrons' energies increase. In *k*-space this corresponds to increasing the radius of the electron sphere. Since excitations occur at the intersection in reciprocal space, of this sphere with occupied initial states, by changing the photon energy we can probe different regions of the BZ.

An photon energy of 90 eV corresponds to the point of intersection of the BZ along the ΓX line with the FES close to X point. Obviously, the final state for PES is quite different than at hν = 45 eV. Indeed, the angular distribution of photoelectrons from 10 ML Co/Cu(001), shown in figure 3.7, has distinct, X-like pattern instead of cross-like. The top image is taken at E_b =1.3 eV, the Co 3*d* band, while the bottom image is acquired at E_F. Both show the symmetry of angular distribution which correspond to 3*d*-t_{2g} (d_{xy}, d_{xz}, d_{yz}) electron orbitals.

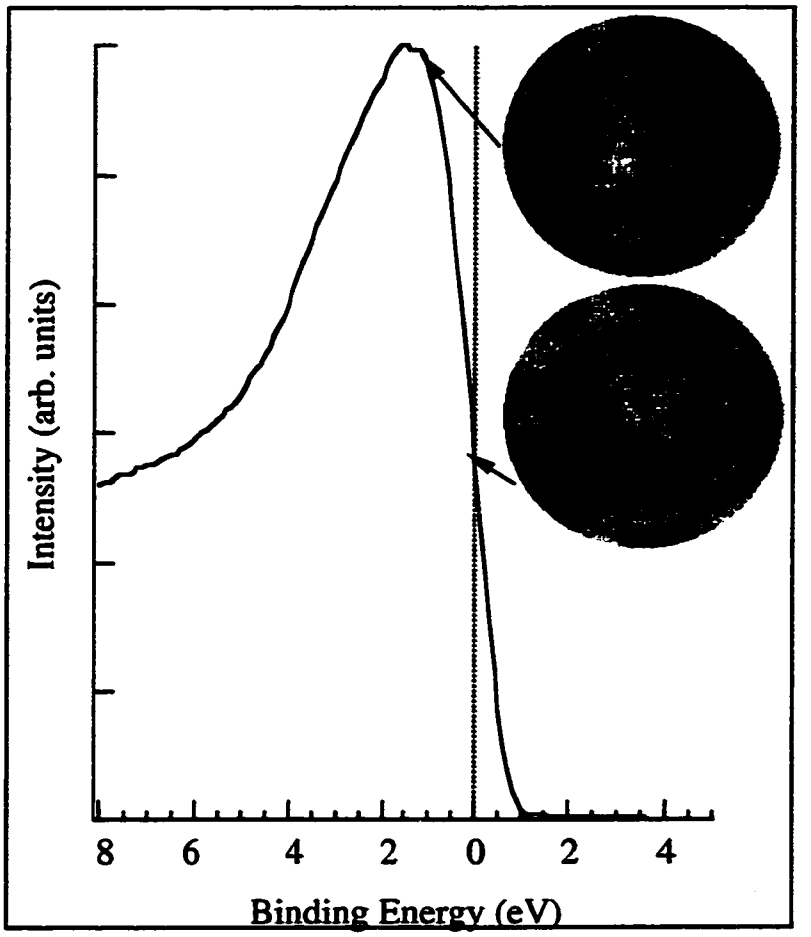

Figure 3.7 EDC in photoemission from 10 ML Co/Cu(001) at hν = 90 eV. Inserts show angular distribution of the photo-electrons at Fermi edge and at the top of Co *d* -band.

So far we have discussed two quite distinct regimes for studying symmetries of the electronic bands by using EMA display type analyzer. **First,** one can acquire angular distributions of the photoelectrons for fixed photon energy. By varying the kinetic energy of detected photoelectrons we probe different initial states with different binding energies, while the final state in the free electron approximation remains nearly constant. Therefore, this regiment is similar to constant final state (CFS) spectroscopy in conventional PES. Figure 3.8 illustrates this approach showing the evolution of photoelectron angular distributions from 8 ML Co/Cu(001) at hν =45eV. It should be mentioned that at this Co film thickness the intensity of photoelectron emission from the Cu substrate is on the order of 5% at 2 eV binding energy. Therefore, we are primarily imaging photoelectrons from Co 3*d* bands.

The **second** regiment is accomplished by changing the photon energy and keeping the binding energy constant. In this case we fix the initial state energy and vary the final state. This is equivalent to constant initial state (CIS) spectroscopy in conventional photoemission. This allows us to probe the symmetry and parity of the final states in different regions of Brillouin zone. Effectively, the intersection of the FES with the z axis moves along $\bar{X}\Gamma X$ direction of *fcc* BZ. The evolution of the angular distributions from the Fermi edge (E_b = 0 eV) of 10 ML Co/Cu(001) are shown in figures 3.9 and 3.10 for photon energies from 21 eV to 77 eV. It should be mentioned that in these images the same angular acceptance is shown. In reciprocal space, $|\vec{k}|$ scales with a factor proportional to $E_{ph}^{1/2}$. When scaled to display constant $\vec{k}$-vector, the images will look like a set of circular patterns of increasing radius (see figure 3.11). The X like feature which has t_{2g} symmetry and may be attributed to Co 3*d* t_{2g} orbitals is the only visible feature on the image acquired at photon energy 21 eV. But around 23 eV the symmetry of images changes drastically. The main feature in the next images has e_g like character. As photon energy increases, the patterns become

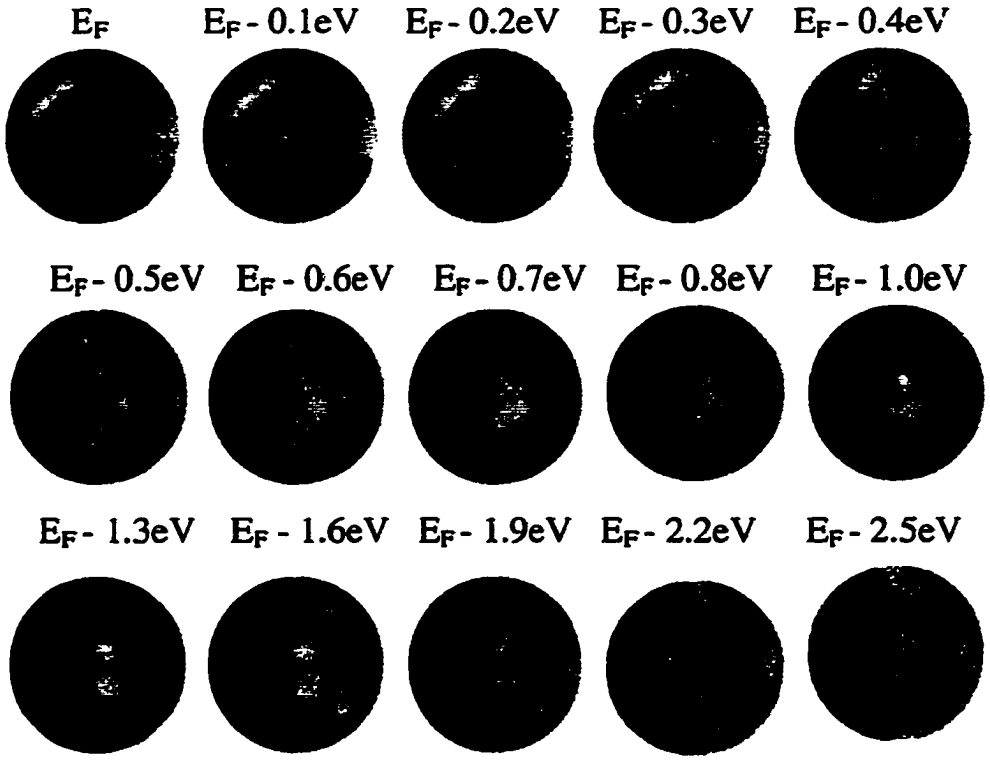

Figure 3.8 Evolution of the photoelectron angular distribution in photoemission from ~8 ML Co/Cu(001) taken for different values of kinetic energy at hν = 45 eV .

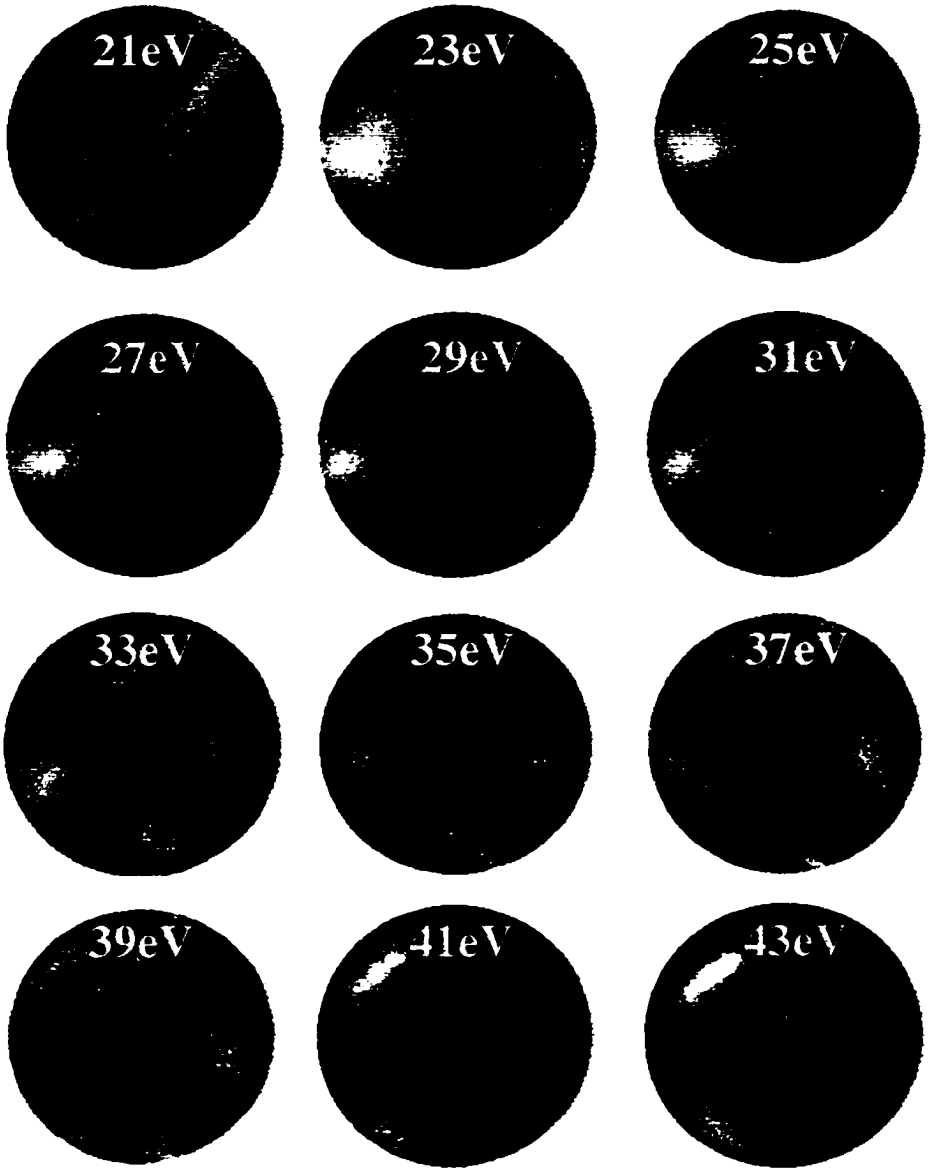

Figure 3.9 Evolution of angular distribution of the photoelectrons in photoemission from Fermi edge of ~10 ML Co/Cu(001) as a function of Photon Energy. Part I.

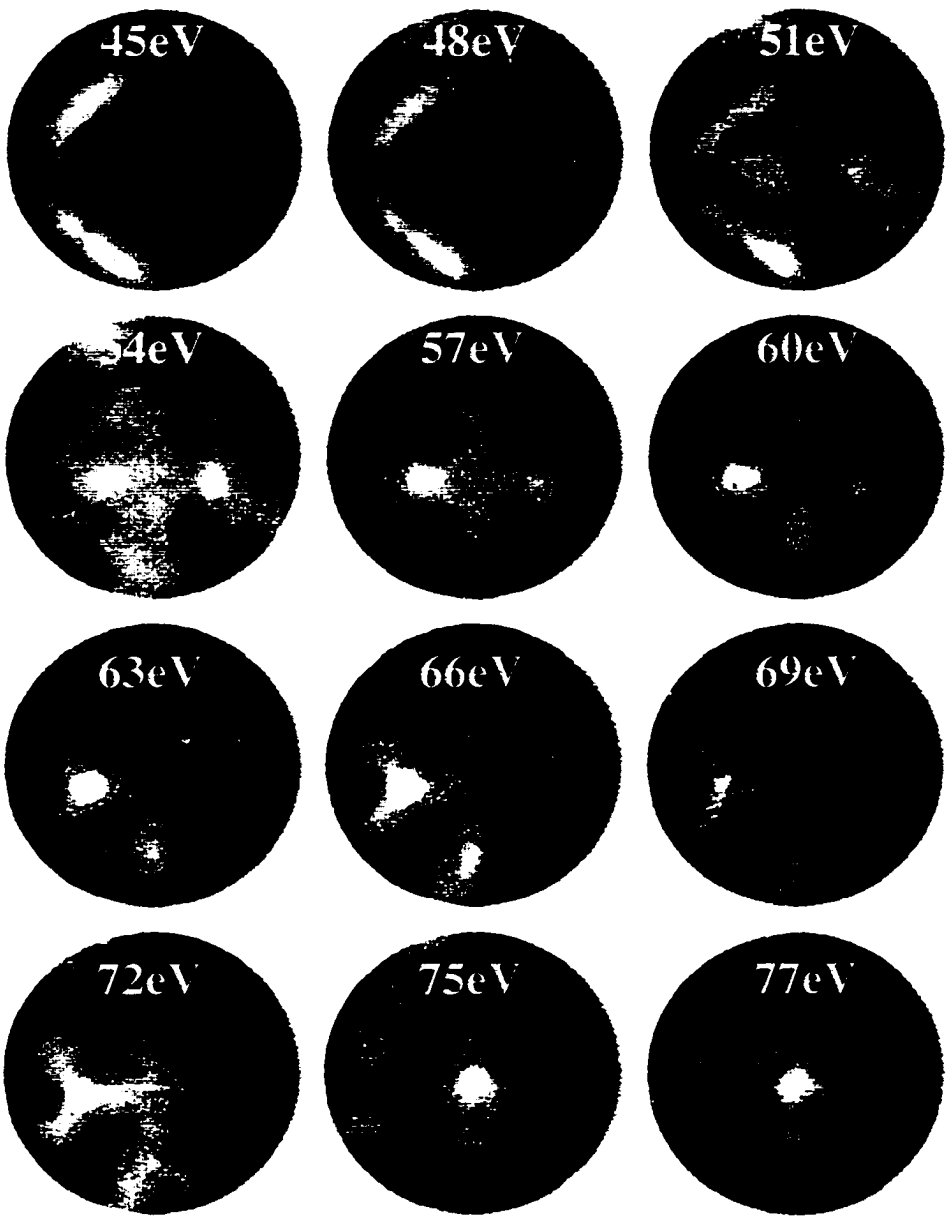

Figure 3.10 Evolution of angular distribution of the photoelectrons in photoemission from Fermi edge of ~10 ML Co/Cu(001) as a function of Photon Energy. PartII.

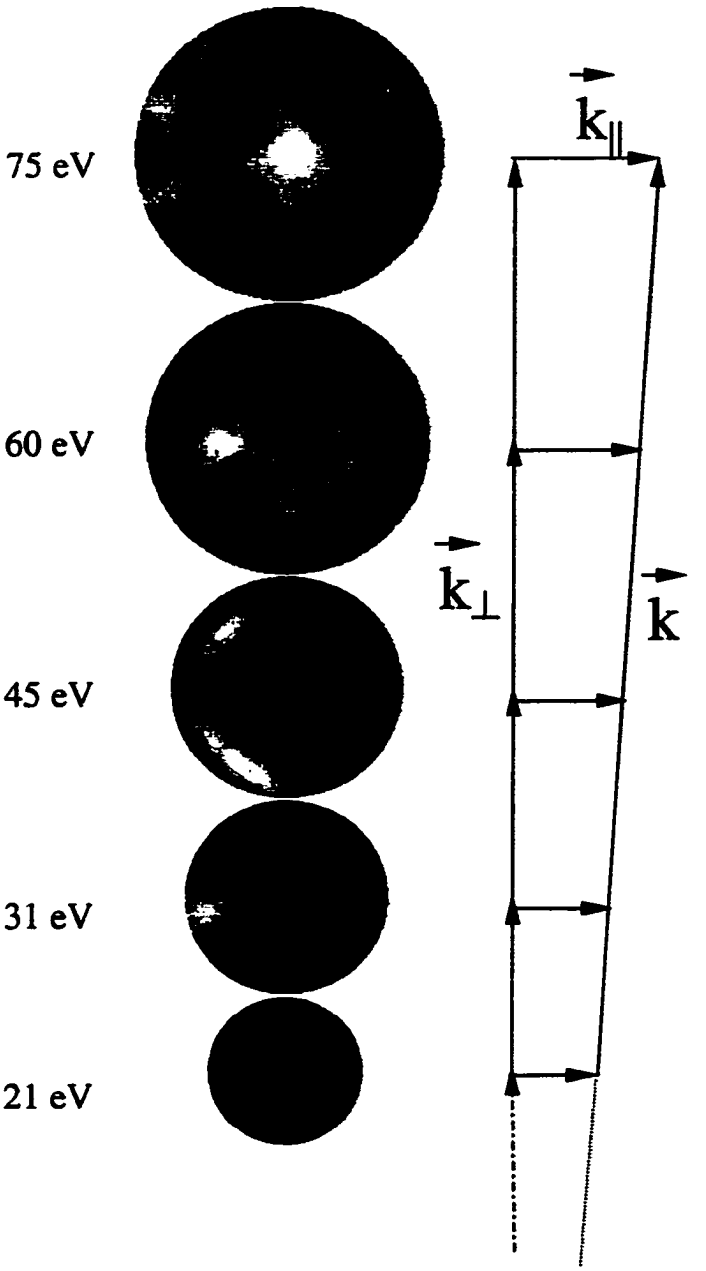

Figure 3.11 Evolution of angular distribution of the photoelectrons in photoemission from Fermi edge of ~10 ML Co/Cu(001) as a function of Photon Energy. Part III.

more complex and in order to explain them, calculation of the transition matrix elements for a specific experimental geometry is required. Nevertheless, it is possible to identify the Fermi surface contours, which appear in the images at photon energies about 37-39 eV as arcs and persist to be a dominant feature in the angular distributions up to about 51 eV. The character of dispersion with increase of photon energy, shape, and symmetry of this feature uniquely points on 4*sp* hybridized band of *fcc* Co. At photon energies around 57-59 eV the 3 $d_{x^2-y^2}$ feature is dominant, at 75-77 eV -- 3 d_{z^2}. Finally, around 90eV, the dominant feature in angular distribution has again t_{2g} character, similar to figure 3.7.

3.3 Magnetic Dichroism in PES from Valence Band of Co/Cu(001)

Many experimental studies involving magnetic linear dichroism (MLD) and magnetic circular dichroism (MCD) have been done on magnetic films in X-ray absorption experiments at the $L_{II,III}$ edges of 3*d* transition metals.[65, 66] In addition, there are numerous studies of MXCD/MXLD in photoemission from core 2*p* levels.[23, 67, 68] The selection of these core levels is quite understandable since the splitting between $2p_{1/2}$ and $2p_{3/2}$ is of order of ~20 eV. This large spin-orbit splitting makes it easy to do measurements and to explain the results using sum rules.[66] Experiments on dichroism from shallow 3*p* core levels show that the reduced spin-orbit splitting of order of ~1 eV, coupled with the broader linewidth result in smaller dichroism effect compared with those in the 2*p* core levels.[52, 69]

Very few studies of dichroism in the valence bands have been performed, in part, due to the small (~ few %) effect.[54, 24] The studies that have been performed have used conventional (hemispherical) analyzers, often in normal emission configurations. This means that only restricted regions of the Brillouin zone have been sampled, and usually those have been along high-symmetry directions.

With our display analyzer, we can simultaneously sample large regions of the Brillouin zone, including regions of low symmetry. This means that we can observe dichroism in angular distributions that may be a small effect when angle-integrated but larger when observed as angle-resolved. For example, an effect that increases intensity in one direction and lowers it in another could give a negligible effect in angle-integrated mode. This same phenomenon could be significant when viewed with the display analyzer. This is the rationale behind the our studies presented here.

In our experiments with Co/Cu(001) we have used 8-10 ML thick films of Co deposited on a Cu substrate and magnetized in-plane along the [010], "easy" magnetization-axis direction. Magnetization reversal was achieved either by direct remagnetization of the sample or by rotating the sample azimuthally by 180°. This rotation is accomplished using a unique mini rotational stage designed by Professor Phillip Adams, and made by the Physics and Astronomy machine shop.

The data in figure 3.12 show the comparison of MCD observed in a longitudinal geometry, where the sample magnetization vector, $\vec{M}$, lies in the reaction plane and is parallel to the polarization plane of the light. In general, linearly polarized light (LPL) may be viewed as equal contribution of left-hand and right-hand circularly polarized (LCP and RCP) photons. In this case the direction of $\vec{E}$ for the incoming electromagnetic wave is perpendicular to $\vec{q}$, the photon momentum, and fixed in space defining the plane of the light polarization. Circularly polarized light was obtained by blocking ~ 66% of incoming photon flux coming from the synchrotron storage ring with water-cooled baffles, giving only photons coming above or below the plane of the synchrotron.

The MCD asymmetry is defined as:

$$\text{Asymmetry}_{MCD} = (I_{RCP} - I_{LCP})/(I_{RCP} + I_{LCP}) \qquad (3.4)$$

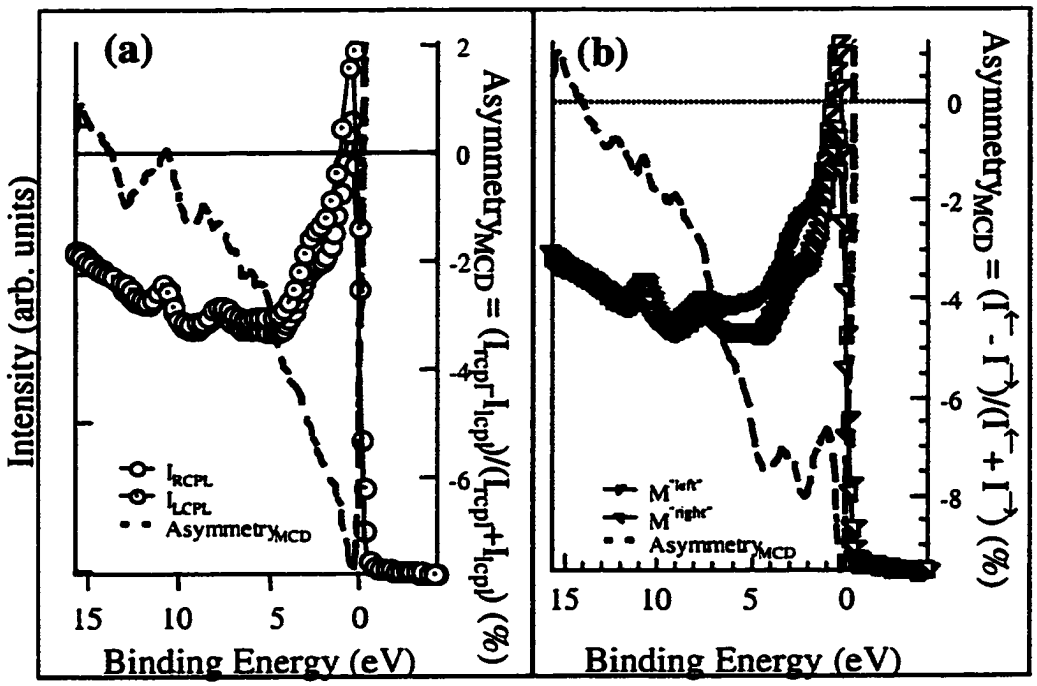

Figure 3.12 Comparison of angular integrated MCD in photoemission from the valence band of ~8ML Co/Cu(001) film (a) by changing the helicity of the circular polarized light from RCP to LCP, and (b) by switching the direction of magnetization from "left" to "right". In both cases M is parallel to the plane of incidence and $h\nu$ = 45 eV.

where I_{RCP} and I_{LCP} denote intensities in photoemission for right and left circularly polarized light. In panel (a) one can see changes in the EDC's from the valence bands of 8 ML Co taken at hν = 45 eV when the light helicity is changed from RCP to LCP. No background was subtracted. Panel (b) shows the results of the MCD experiment with the same film when, at fixed helicity (RCP) of the light, the sample was rotated by 180°. Qualitatively the results look very similar. Nevertheless, there is a difference in the fine structure of the asymmetry curves. This difference in terms of the symmetry properties for the different dichroism configurations given by Venus.[20] The helicity reversal of CP light by taking photons above/below synchrotron plane also gives rise to the linear dichroism term and should be considered as a superposition of MCD and MLD. It should be mentioned that the current experimental setup does not allow one to obtain RCP and LCP light with the same intensity and degree of polarization which also may affect the shape of the MCD asymmetry curve obtained by helicity reversal.

Figure 3.13 compares data obtained with RCP light at hν = 45 eV in both longitudinal and transverse geometries. Panel (a) is the same as panel (b) of the previous figure. Panel (b) shows data obtained when the magnetization $\vec{M}$ is perpendicular to the reaction plane. The value of the asymmetry is lower by a factor of 3.5 in the transverse geometry, compared to the longitudinal one.

Due to the nature of MCD/MLD in PES, the value, and even the sign of the asymmetry is dependent on photon energy. By choosing the photon energy we can probe initial states of a specific symmetry. As it was shown in previous section, at a photon energy equal to 21eV, the dominant feature in the angular distribution of photoelectrons is from bands with t_{2g} symmetry. The 3*d* bands of this symmetry are responsible for appearance of X-like features in angular distributions close to X points of the BZ. That is the reason we have concentrated our efforts at this value of hν. In

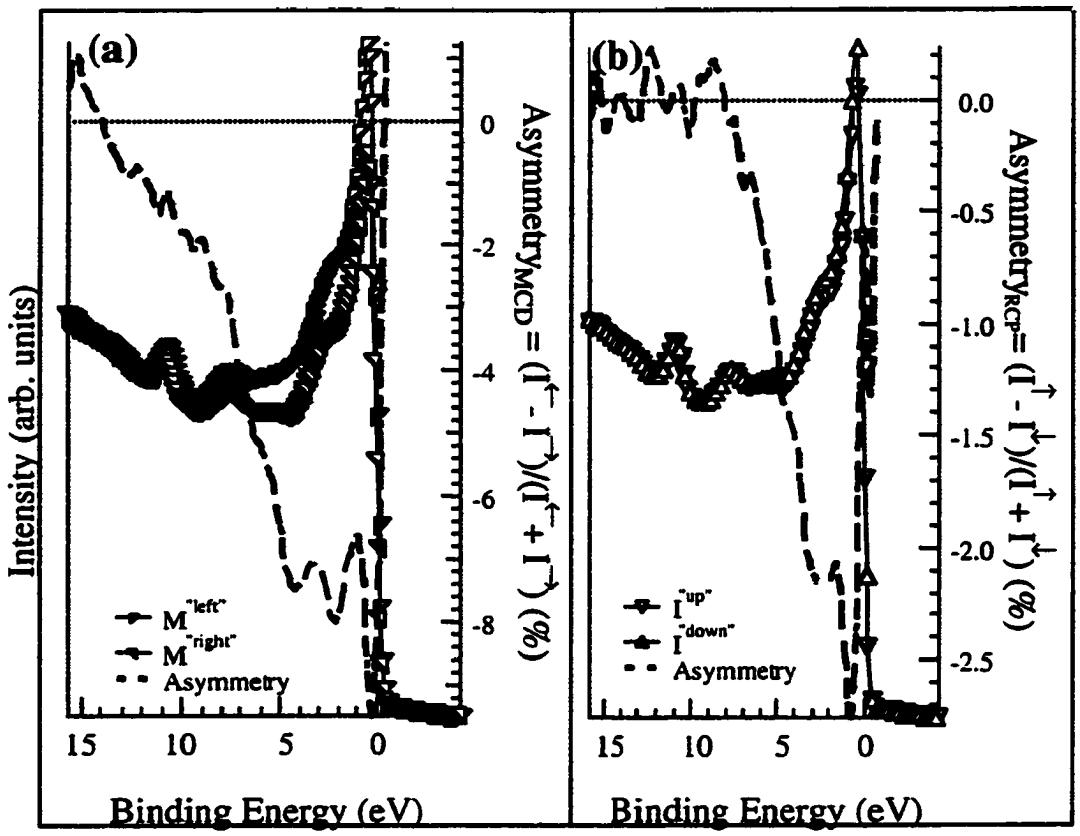

Figure 3.13 Comparison of the angle-integrated MCD in photoemission from the valence band of ~8 ML Co/Cu(001) film (a) by switching the direction of magnetization from "left" to "right", and (b) from "up" to "down". In both cases the helicity of the circularly polarized light remains the same and hν = 45 eV.

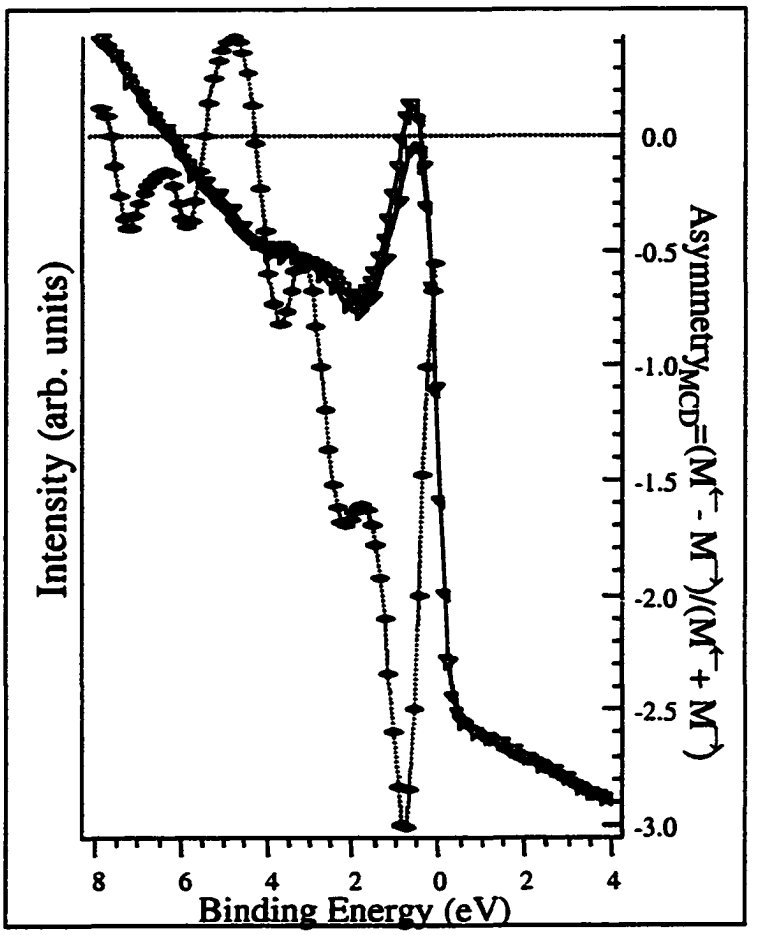

Figure 3.14 MCD in a photoemission from 10 ML Co/Cu(001). hν = 21 eV. Reverse magnetization along horizontal axis.

figure 3.14 we present our data on magnetic circular dichroism in angular integrated photoemission from 10 ML Co/Cu(001). The film was magnetized along the horizontal axis and studied with circularly polarized light, hν = 21 eV, and dichroism was observed upon reversal of the direction of magnetization. Solid lines with left and right rotated triangles correspond to EDC's for "left" and "right" orientation of sample magnetization. The dotted line with diamonds shows the resulting asymmetry. A maximum absolute value of asymmetry ~3% is observed at a binding energy of 0.75eV.

Figure 3.15 shows the angular distribution in photoemission for the same film taken at a binding energy of 0.4 eV. The left image was taken with the sample magnetization pointed to the left, and right image with magnetization to the right. The bottom image is a difference of two above and gives the magnetic circular dichroism in angular distribution (MCDAD).

The first data on magnetic linear dichroism in angular distribution (MLDAD) from ~8 ML Co/Cu(001) were obtained by Subramanian and Mankey.[59] Their data combined with that taken here are shown in figure 3.16 where the dichroism is obtained simply by a magnetization reversal. The EMA is capable of imaging the electron emissions within an acceptance angle of 64°, as stated before. This enables one to probe the electronic states in large volumes of the Brillouin zone and hence obtain MLD angular distributions (MLDAD) with specific momenta. By being able to choose the binding energy of the initial states, the measurement can be performed on specific bands. This is what has been attempted here. In the previous work, the maximum value of the asymmetry for angular integrated EDCs was ~12% at a binding energy of 0.65 eV.[59] In that case, the asymmetry was defined as fraction of the average for magnetization $\vec{M}$ "up" and $\vec{M}$ "down" intensities.

$$\text{Asymmetry}_{MLD} = (I^{"up"} - I^{"dn"})/0.5\cdot(I^{"up"} + I^{"dn"}) \qquad (3.5)$$

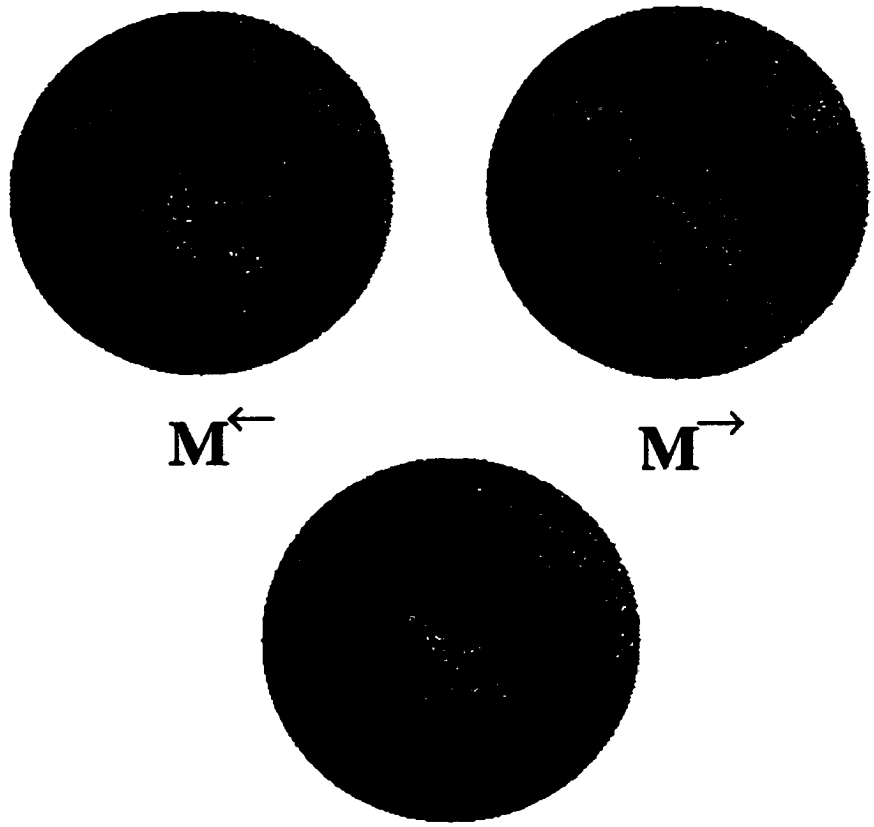

Figure 3.15 MCDAD in photoemission from 10 ML Co/Cu(001). $h\nu = 21$ eV. The top images are collected at $E_b = 0.4$ eV for a reversal of magnetization along the horizontal axis. The bottom image is a difference, which represents the asymmetry in the angular distributions.

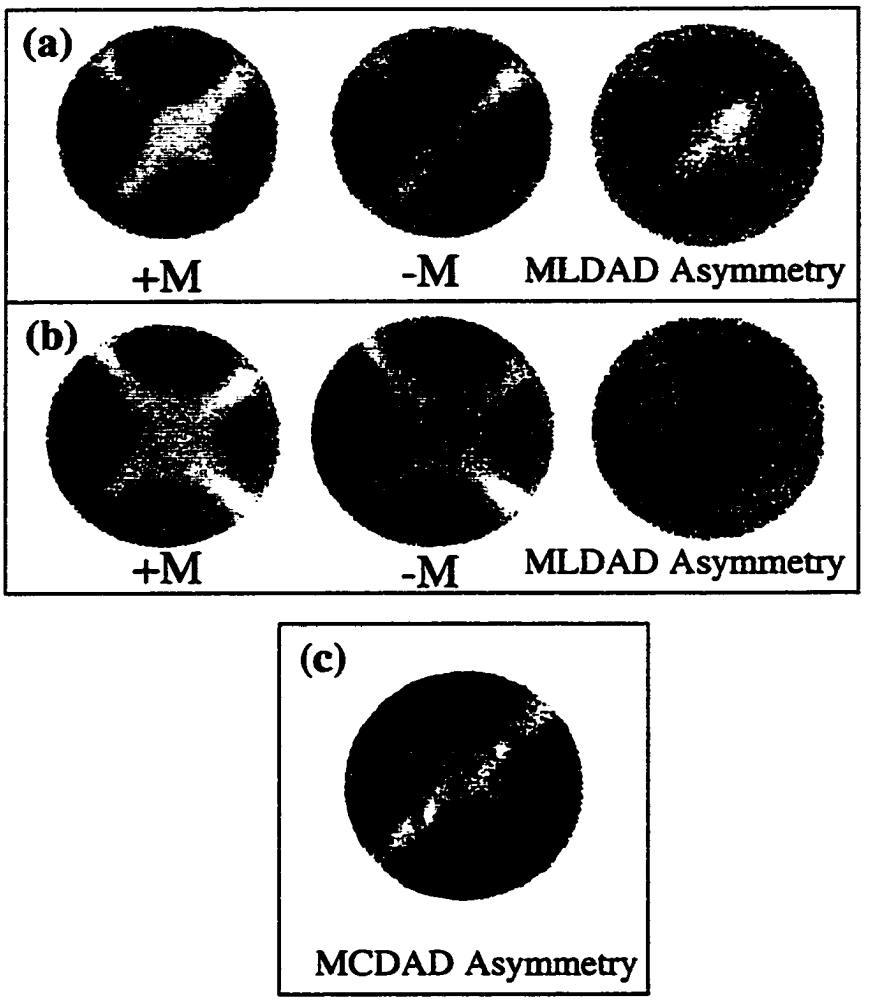

Figure 3.16 Magnetic linear dichroism in angular distribution (MLDAD) from 8 ML Co/Cu(001). The angular distributions in photoemission with linearly polarized light, hν = 21 eV, for "up" and "down" orientation of magnetization, and images of the respective asymmetries shown to the right: (a) at E_b= 0.5 eV, and (b) E_b= 0.7 eV. Figure (c) is the same as (a), but with circularly polarized light.

This is twice the asymmetry defined in equation (3.4). Panels (a) and (b) show the angular distributions in PES from 8 ML Co/Cu(001) film with linearly polarized light for "up" and "down" magnetization of sample and respective asymmetries in angular distribution for binding energies (a) $E_b = 0.5$ eV, and (b) $E_b = 0.7$ eV. Images of the angular distributions show a bright X-like feature which is due to emission from the d_{XY} initial state. At this photon energy we are sampling states midway X to Γ. The images for $\vec{M}$ "up" in (a) and (b) show strong intensity in the center. In contrast, the data for $\vec{M}$ "down" shows weaker intensities at the center of the images, but stronger emissions near the edges of the image along the [110] azimuth in (a), and along the [1$\bar{1}$0] azimuth in (b). The differences between $\vec{M}$ "up" and $\vec{M}$ "down" images in (a) and (b) are the dichroic signal or the MLDAD. The darker regions correspond to negative asymmetry and the lighter regions correspond to positive asymmetry for a specific direction in $\vec{k}$-space. In (a) the bright region in the center of the image reflects the strong emission from the "up" image and the darker regions at the edges of the image reflect the strong emission from the "down" image. For (b) the change in the patterns are striking. The "up" image shows a strong emissions along the [110] azimuth near the edges of the image, while the "down" image shows strong emissions along the [1$\bar{1}$0] azimuth. The MLDAD reflects this clearly. Thus for emission from the same band, the d_{xy} orbital, the dramatic changes in the MLDAD reflect the sensitivity to changes in the spin-orbit coupling strengths in different parts of the Brillouin zone. The MLDAD shows an evident two-fold symmetry. Panel (c) shows MLDAD asymmetry obtained in a similar manner to case (a), but with circularly polarized light. One can notice that the symmetry of this image is the same as in (a). This clear two-fold symmetry observed in the MLDAD is consistent with theoretical predictions based on a single localized emitting shell[70, 71]. These calculations are

particularly applicable to the *d*-bands in solids, because of their relatively flat dispersions.

Two additional sets of data on magnetic linear dichroism in angular integrated photoemission are presented in figure 3.17. Both data sets were taken from the same sample which was 10 ML Co/Cu(001). The film was magnetized in-plane along the [100] "easy" axis of magnetization and studied both in longitudinal and transverse geometries with linearly polarized light. The sample orientation was changed by rotating it 90°,180°, and 270° around the sample normal. The shapes of the MLD asymmetry curves, in both cases, are very close while the maximum value for asymmetry observed in longitudinal geometry, 14.8%, is more than twice the 7.2% observed in the transverse geometry. The second value is very close to the value extracted from the data reported by Subramanian and Mankey in a similar experiment.[59] The maximum asymmetry in the transverse geometry occurs at a binding energy 0.75 eV which is also very close to that reported earlier. The difference between the DOS for majority and minority *d*-bands of bulk fcc Co calculated using the FLAPW algorithm also show two minima, located at binding energies of 0.94 and 0.79 eV and they are due mostly to t_{2g} electrons. These calculations can not be used as an argument to justify the position of maximum in MLD asymmetry for two reasons. First, the bulk bands are slightly different from the bands of thin films, to get a proper DOS one needs to perform "slab" calculations. Secondly, the calculations were performed without including spin-orbit coupling, which was shown by Mainkar [72] to play a minor role in the overall band structure of 3*d* metals, but is very essential for the determination of exact band locations.

More striking is the energy shift of the maximum in asymmetry in longitudinal geometry by 0.5 eV towards E_F. For now we do not have an explanation for this. The inserts in panels (a) and (b) show the respective asymmetries in angular distribution

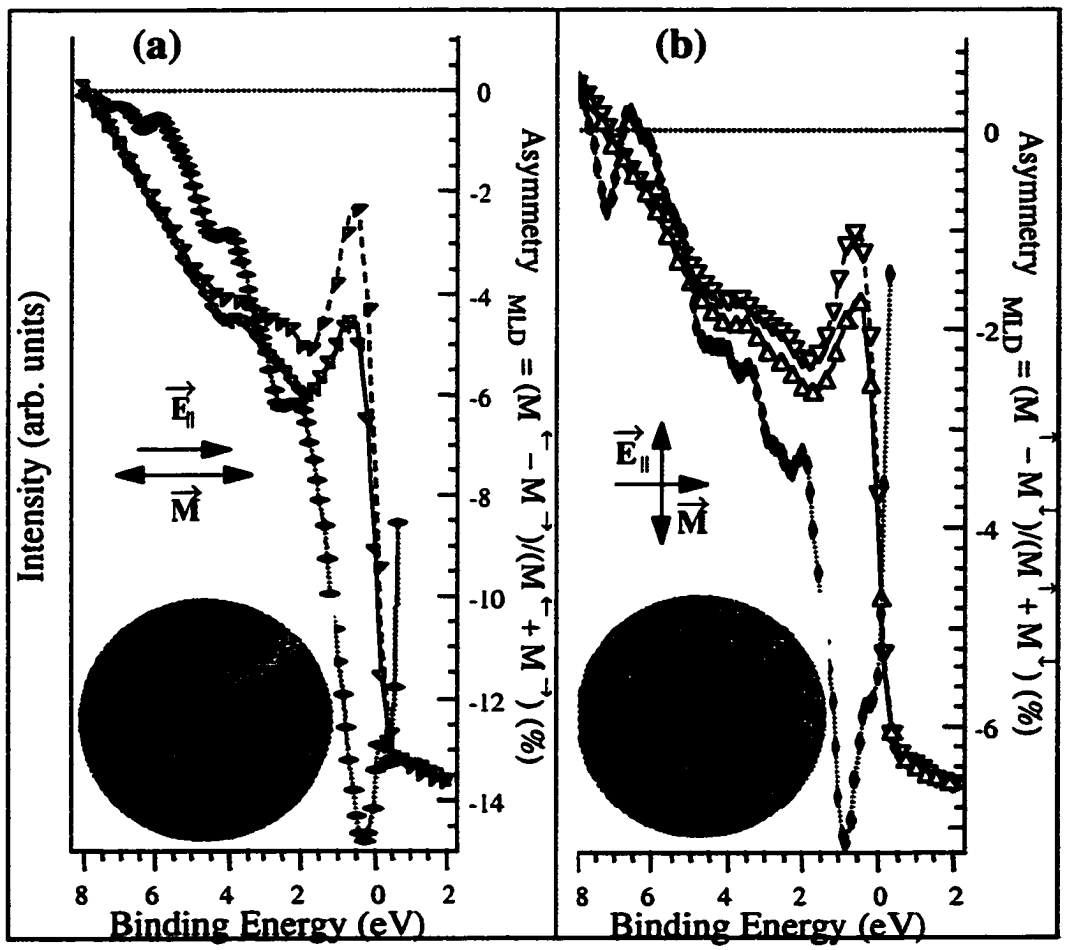

Figure 3.17 Comparison between MLD in photoemission from the valence band of 10 ML Co/Cu(001) (a) in longitudinal geometry, when M is in the plane of reaction, and (b) in transverse geometry, when M is perpendicular to that plane. $h\nu = 21$ eV. Inserts are showing the respective asymmetries in angular distribution at $E_b = 0.4$ eV.

obtained at a binding energy 0.4 eV. The contrast along the image diagonal is a consequence of misalignment of sample normal with respect to axis of rotation by about 1.5°. Without this misalignment, the image in figure 3.17 (b) would look nearly identical to that in figure 3.16 (a) although rotated by 180°. The image on the left panel may be explained from very basic symmetry considerations. The change in the magnetization along the direction of the light polarization should affect the angular distributions in terms of the left-right asymmetry of the image. This is what we have observed. A more complete explanation of the intensities may be given only by a rigorous calculation of the transition matrix elements for the specific experimental geometry.

The next logical step of our study is to examine the asymmetry in angular integrated photoemission as function of photon energy. A number of MLD experiments in the transverse geometry were performed in the range of photon energies from 20 to 45 eV. The results are shown in figure 3.18. The left panel shows the EDC's for different photon energies. Spectra are offset along the vertical axis for convenience. The solid line corresponds to magnetization "up" and the dotted line to magnetization "down". On the right panel are shown the respective asymmetries fit with a spline curve. The right axis for each curve shows the value of the asymmetry in percent. The maximum absolute value for asymmetry, which is located at a binding energy of ~1 eV, monotonically decreases with increasing photon energy, and at 35eV it is virtually vanishing, within the sensitivity of our experimental setup. These data, together with data on the asymmetry in the angular distributions in photoemission (CPL at 45 eV, figure 3.19) suggest that the Co $3d$-e_g states have very little, if any, impact on the magnetization, and magnetic dichroism for this system.

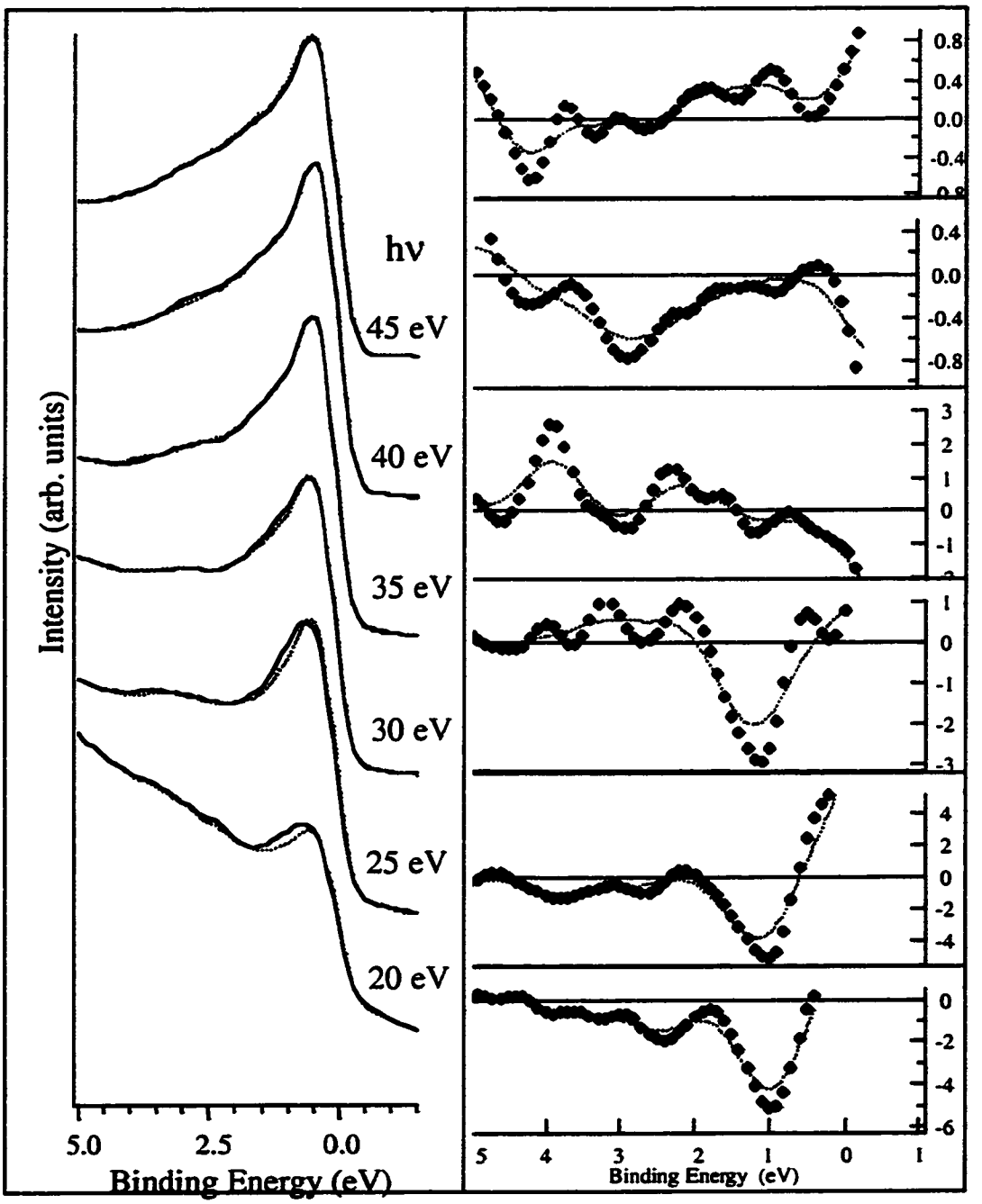

Figure 3.18 MLD in transverse geometry from ~12 ML Co/Cu(001). Study of asymmetry as function of Photon Energy. Left panel shows "up" and "down" spectra as a solid, and dotted lines for various hν. Right panel shows corresponding asymmetries.

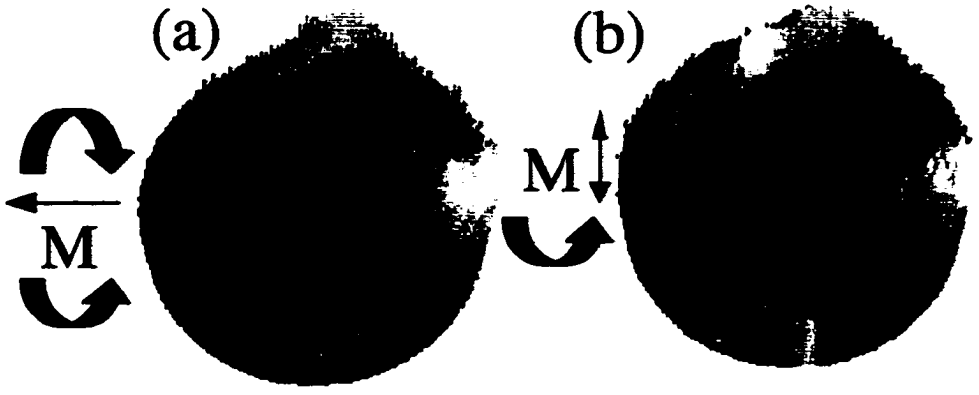

Figure 3.19 3D reconstruction of asymmetry in the angular distributions for (a) MCD at hν = 45 eV, with the magnetization along the horizontal axis, reversed helicity of circularly polarized light, images are taken at E_b = 0.38eV; (b) MCD/MLD at hν = 45 eV RCP light, magnetization along vertical axis, reversed direction of magnetization, images are taken at E_b = 0.36eV.

3.4 Magnetic Dichroism in XR Absorption from Co/Cu(001)

Despite the fact that photoemission was our primary technique for studying magnetic films, other techniques have been used as well. As an illustration of other possible experiments with the EMA using synchrotron light to study magnetic films I will show data in X ray absorption obtained at CAMD on Co/Cu(001).

In figure 3.20 we show constant final state spectra in "soft" X ray absorption over the Co M edge from 10 ML Co/Cu(001). The experiment was performed in the transverse geometry with circular polarized light. The total electron yield (TEY) was measured from the sample and normalized with respect to incoming photon flux. The solid and dashed lines correspond to opposite directions of magnetization. The diamonds are the resulting asymmetry fit with a spline curve. Although there is a visible difference, the effect is quite small and it is close to the limit of detection. The effect is suppressed, in part, due to the limited resolution of the beamline.

Figure 3.21 gives the magnetic X-ray circular dichroism (MXCD) in X ray absorption over the Co L edge from 12 ML Co/Cu(001) both in the transverse and in the longitudinal geometries. The solid and dashed lines are spectra taken for opposite directions of magnetization. As in the previous experiment, the intensity was measured as a TEY normalized with respect to total photon flux. The Co $2p_{1/2}$ and Co $2p_{3/2}$ states are clearly seen although poorly resolved due to the photon linewidth. The dotted lines with diamonds are the dichroism asymmetries. These data are consistent with data obtained by other groups.[66] The point of concern with this experiment is again low beamline resolution. By comparing these spectra with spectra obtained at another light source a rough estimate is that the PGM resolution at these energies is about 4 times worse than beamline at the Advanced Light Source (ALS) at Lawrence Berkeley National Lab.[73]

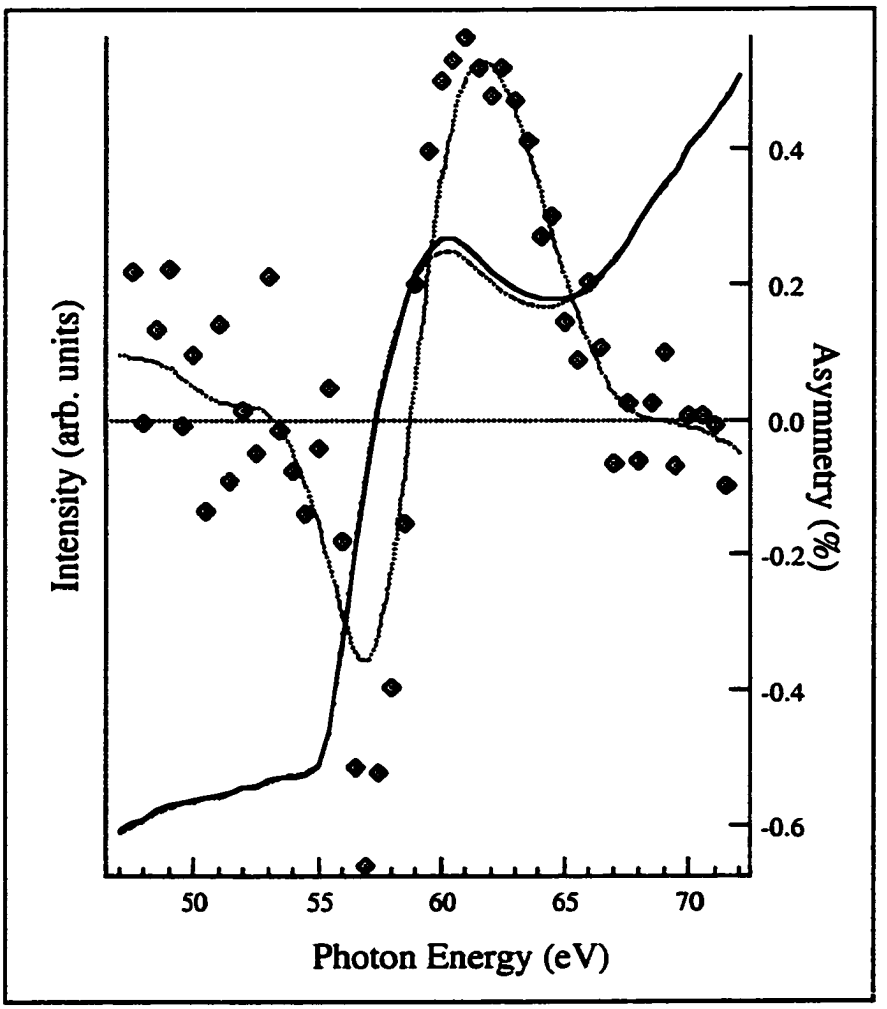

Figure 3.20 Magnetic Circular Dichroism in UV absorption. Solid and dashed lines show CFS spectra over Co M edge for opposite Directions of magnetization of ~10 ML Co/Cu(001). Dotted line is a polynomial spline fit of the asymmetry in total photoelectron yield.

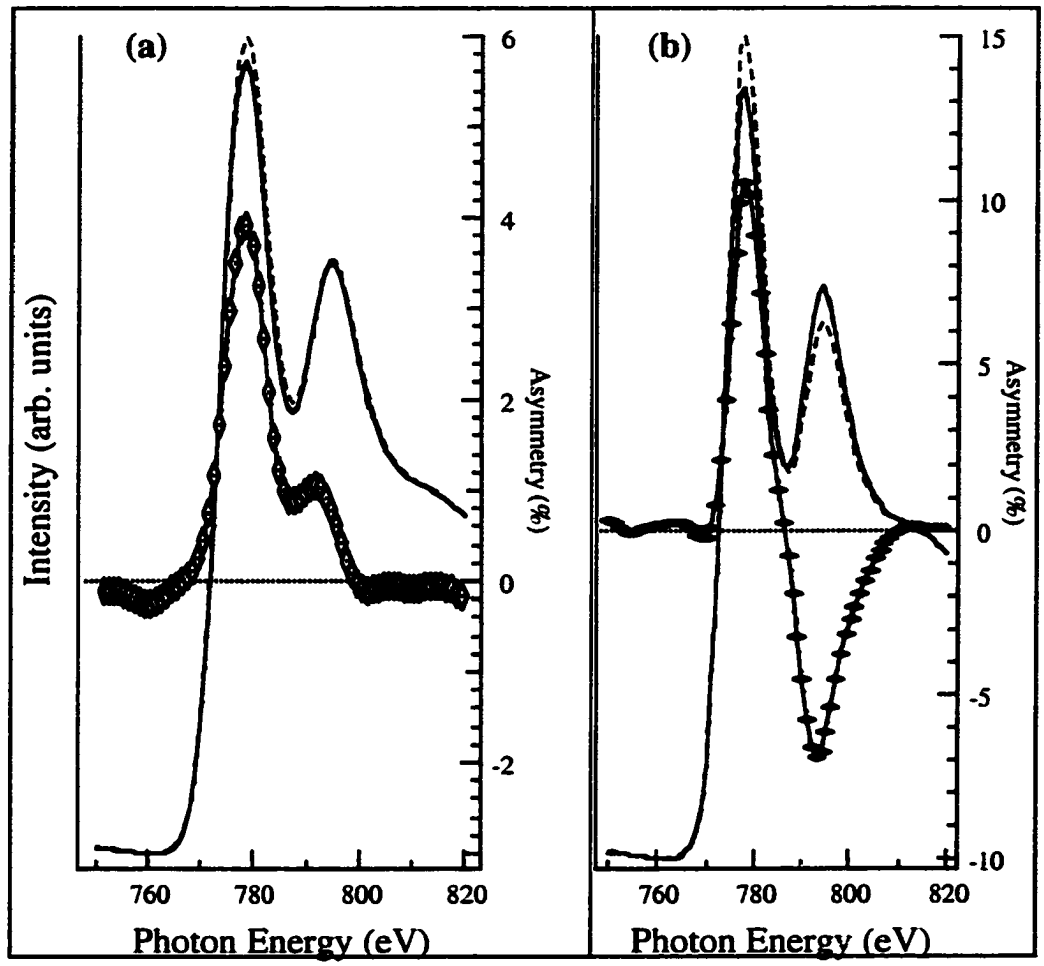

Figure 3.21 Comparison of MXCD on a Co L edge of ~12 ML Co/Cu(001) (a) in transverse, and (b) in longitudinal geometries. Solid and dashed lines show respective XR absorption spectra, taken with circularly polarized light, for opposite directions of sample magnetization. Lines with diamonds show relative asymmetries.

3.5 Conclusions

The data presented in this chapter provides new information on the nature of the electronic structure of Co films on Cu(100). Although Co has a bulk *bcc* crystal lattice, our LEED data are consistent with Co films growing in a pseudomorphic *fcc* on Cu(100). In fact, our LEED and PES data show no evidence of *hcp* lattice for coverages up to approximately 12 ML and this agrees with prior studies of the structure and morphology of Co thin films grown on Cu surface. For a similar system of Fe/Cu(100) it was shown that pseudomorphic growth can be extended by the presence of surfactants like CO up to about 60 ML.

Our first step at characterizing the electronic structure involved investigating the hν-dependence of the valence band photoemission spectra. It is well known that the 3*d* transition metals undergo a resonant process in the photon energy ranges that are of interest here. This resonant process affects the valence band photoemission intensity and it is due to an opening of an extra channel for electron emission. This occurs by an Auger-like decay of the transition state for photon energies above the 3*p* excitation threshold, resulting in a new channel for emission of a valence band 3*d* electron. This is essentially many-body process involving electron-hole interactions in the valence band. Our interest in Co/Cu(100) is in characterizing the ground state, however, and not this multi-electron excitation. In order to avoid unnecessary complications caused by these interactions in most of the cases we have chosen photon energies well below the resonant threshold in order to perform our magnetic dichroism experiments.

Co and Cu have electronic structures that are similar in many ways. They essentially differ by the increased band filling of Cu. These similarities should be reflected in photoemission angular distributions when similar initial states are probed.

This was found to be the case when angular distributions (AD) in PES from the Fermi edge are similar to those from the Cu 3*d*-band at 2 eV below E_F. Our data show that this is the case at the photon energies corresponding to the center of the BZ ($h\nu = 45$ eV) and close to the zone boundary BZ ($h\nu = 90$ eV). In the more general case of an arbitrary photon energy, when the free-electron final state surface samples the BZ somewhere between high symmetry points, the patterns of angular distributions for Co are different from those of Cu and Ni reflecting an element specific features of band structures for these materials. Our patterns also indicate a strong sensitivity towards azimuthal and polar-angle sample misalignment with respect to plane of incidence due to polarization effects in PES. Careful sample alignment is critical in order to acquire symmetric images.

The angular distributions that we observe reflect both the symmetry of the initial state and that of the final state. Some of the patterns that we observed, especially for those from the middle of the BZ and those close to the zone boundary, can be satisfactory explained from spin-polarized calculations of *fcc* Co Fermi surfaces. We performed these calculations using the WIEN97 FLAPW code [74] and visualized constant energy surfaces using Interactive Data Language (IDL). By comparison with calculated FS contours one can deduce that at $h\nu = 45$ eV, when we are sampling states in the middle of the Brillouin zone, the dominant feature in the photoelectron angular distribution is due to majority spin bands. At $h\nu = 60$ eV, which samples states roughly half way to the zone boundary, the observed features are due to minority spin bands, and for $h\nu = 72$-77 eV we observe features which are due to a combination of both. We are currently working on theoretical calculations of the photoelectron angular distributions from magnetic surfaces in order to compare them with these data. Previous studies in our group showed that it is possible to predict photoemission transition matrix elements including the dependence on light

polarization from first-principles calculations. The calculations for Cu gave reasonable polarization-dependent angular distributions up to photon energies ~45. We are going to generalize this approach to other pseudomorphs, Co and Fe grown on *fcc* Cu.

Since our analyzer can not be modified to study spin-resolved PES from the valence band of magnetic films we choose to use magnetic dichroism (MD) as a tool capable to distinguish majority and minority bands. From our band structure calculations, we can see that it is possible to sample bands with minority and majority spin character and dichroism offers the potential to experimentally distinguish them. The relation of different experimental geometries, light polarization, and the influence of the photon energy are the experimental parameters that we are able to vary. Our data show that in the longitudinal geometry, the reversal of the in-plane magnetization direction is not equivalent to the reversal of light helicity for CPL, at hν =45 eV. Even though the numerical values for the asymmetries were found to be very close, the shapes of the asymmetry curves are quite different. In part, this is due to the angle of incidence of the light. A strict equality between magnetization and polarization reversal would be expected for normally-incident light and out-of-plane magnetization. For the film thicknesses investigated here, Co only exhibits an in-plane magnetization. This means that there is a coupling between excitations involving the component of magnetization along the incidence direction together with the linear dichroism effect that is expected for the perpendicular component.

Even more significant changes were observed in the comparison of magnetic dichroism with CPL in the longitudinal and in the transverse geometries at hν=45 eV. In both cases, we are not in the optimal circular dichroism geometry which has the magnetization aligned with the incidence direction of the CPL. However, in the longitudinal configuration, we are reversing the magnetization with a component of M

along the light incidence direction, and we observe an ~8% effect. In the transverse case, the magnetization and the incidence direction are perpendicular to one another and a significantly reduced dichroism of ~2.5% is observed. This is likely to be due primarily to the magnetic *linear* dichroism resulting from the component of light in the horizontal plane. This is also approximately the same magnitude of MLD that we expect to contribute to the longitudinal configuration.

This coupling of effects is a general trend in data taken with the ellipsoidal-mirror analyzer. For example, in the case of linearly polarized light incident with **A** in the horizontal plane, dichroism that results when a horizontal magnetization is reversed comes about from the out-of-plane component of **A**. A vertical magnetization, on the other hand, provides contributions from both components of **A**. Our current work is to use the band structure calculations to predict the intensity of the angular distributions for the various experimental geometries that we have presented here. With the various configurations that we have studied, we are in a position to separate out these competing effects.

Studies of the magnetic dichroism in the transverse geometry for the photon energies from 20 to 45 eV show that the asymmetry decreases as hν increases and the effect almost disappears at hν =45 eV. This trend makes sense when one considers the nature of the band structure. First, the spin-orbit splitting in the valence bands is small, much smaller than the exchange splitting. This means that much of the dichroism signal that we observe is a result of the nature of the initial and final states. At low photon energies, the partial wave character of the final state strongly affects the photoexcitation probability, and a large sensitivity to the nature of the initial state, and its magnetization, is observed. As the photon energy increases, our final state is composed of multiple partial waves of all different character and the excitation is less affected by the details of the initial state.

In the case of excitation from states with large spin-orbit interaction, such as the $2p$ levels of transition metals, photoexcitation selection rules give rise to a large dichroism signal. This can be used, along with sum rules, to allow one to extract the orbital and spin moments, although there is some debate in the literature as to whether this can be made quantitative.

Our interest, though, is to understand the initial development of the electronic structure, and the measured Fermi surface contours and the behavior of the dichroism provides substantial new information on the valence bands. This information can be compared directly with theoretical predictions that are part of our group's ongoing work.

Chapter 4

Thin Films of Co/Cu(111)

4.1 Introduction

Cu(111) is another monocrystal substrate which has been used in studies of electronic structure and magnetic properties of ultrathin cobalt films. Unlike Cu(001) which is C_{4v}, the surface of Cu(111) belongs to C_{3v} group symmetry. This complicates the studies since none of main axis for *fcc* structure coincides with sample normal.

Co films on Cu(111) have been studied in the past with the following results. Up to two ML, Co films grow as a tetragonaly distorted *fcc* structure. Above 2 ML, it incorporates *hcp* stacking fault. By mean of X-ray forward scattering and a CO titration it was shown that up to about 40 Å of Co/Cu(111) the ratio of *hcp* to *fcc* phases is almost constant and close to 35%.[14] Similar results were observed on a Co/Cu(111) superstructure grown on GaAs substrate.[19] The difference between *fcc* and *hcp* stacking along [111] ([0001] in the case of *hcp*) direction is that consecutive layers in *fcc* structure may be represented as an ABCABC sequence, where each layer (A, B, and C) is two dimensional hexagonal lattice. Each layer is rotated with respect the previous one by 60° and shifted by $\left(\sqrt{3}/4\right)\cdot\mathbf{a}$, where **a** is an *fcc* lattice parameter. In the case of *hcp* the layers can be represented as ABABAB, where A and B are also two dimensional hexagonal lattices rotated by ±60° with respect to previous layer and translated by $(1/\sqrt{2})\cdot\mathbf{a}$, where **a** is an *hcp* lattice parameter. This results in that the two-dimensional Brillouin zone for the *fcc* lattice in the [111] direction and the *hcp* lattice in [0001] direction are essentially identical.

In order to explain observed angular distributions in valence band photoemission from the surface of magnetic materials, a number of full potential linearized plane augmented wave (FPLAPW) calculations of band structures and Fermi surface contours were performed. The 'WIEN97' FPLAPW package for calculating Crystal properties was used.[74] Figure 4.1 shows calculated Fermi surface of *fcc* Co both for majority (a) and minority (b) electron bands as seen along [111] direction. The surface shows clear three-fold symmetry, which will be useful in the interpretation of our angular resolved photoemission data.

The perpendicular to plane remnant magnetization was observed only for up to 5 ML Co/Cu(111) films grown at 80 K and latter annealed to room temperature. [14] The magnetic moment of Co films lies in plane without in-plane anisotropy. This makes (111) plane desired orientation for designing isotropic magnetic media and multilayered GMR structures.

4.2 Experiments

The PES measurements on ultrathin Co films deposited on top of Cu(111) were performed on the PGM beam-line at CAMD. Sample preparation was the same as that for Co films on Cu(001) substrate. The Cu(111) crystal was cleaned with multiple Ar^+ sputter and anneal cycles and allowed to cool down to room temperature. Complete details of substrate preparation are in Appendix A1. An e^--beam heated wire evaporator was used to deposit Co films. The films were deposited at room temperature at an estimated rate as 0.16 ± 0.03 Å/sec which is approximately equal to 0.1 ML/sec. The residual gas pressure during deposition was not worse than $4 \cdot 10^{-9}$ Torr. The sample was transferred to the EMA chamber immediately after deposition and the vacuum in EMA chamber was kept below $1.5 \pm 0.6 \times 10^{-10}$ Torr.

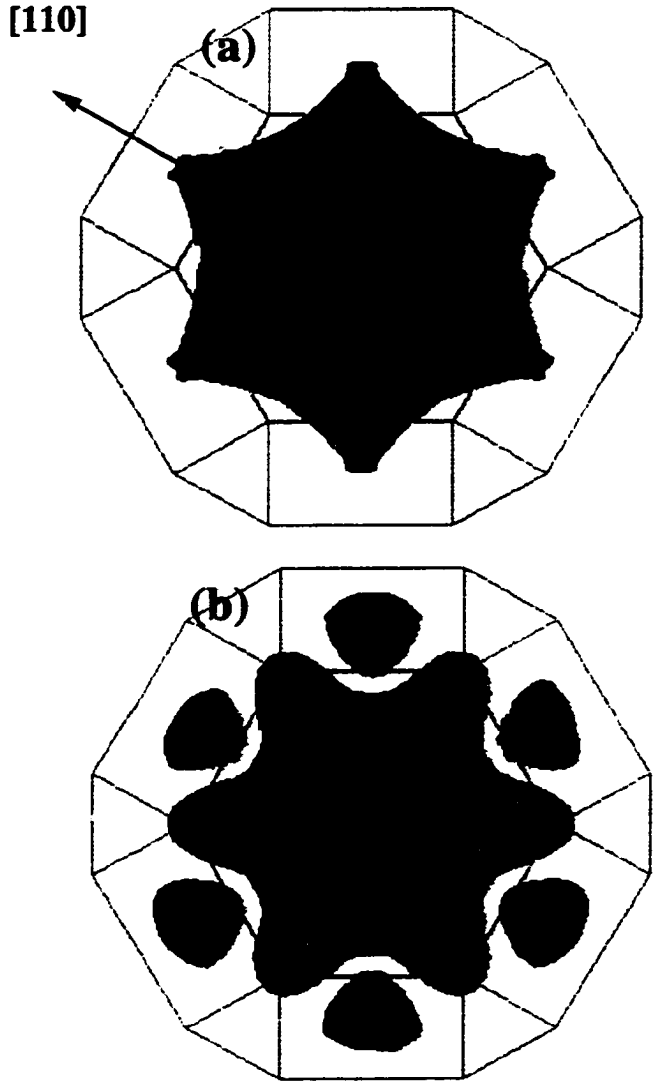

Figure 4.1 Calculated Fermi surfaces for *fcc* Co. Panels (a) and (b) show majority- and minority- electron isosurfaces as seen along [111] direction. Green contours represent *fcc* BZ.

4.2.1 Angle Integrated PES from Co/Cu(111)

The experimental setup was identical to that described in the previous chapter. Linearly or circularly polarized light was incident on the sample at an angle of 45° with respect to sample normal. Angle integrated photoemission spectra were collected within a solid angle cone of ~0.71π sterad (plane angle 64°), normal to sample surface. Photoemission spectra taken with linearly polarized light are shown in figure 4.2 for ~5.2ML Co/Cu(111). The EDC's are aligned with respect to Fermi edge and offset vertically as a function of photon energy (hν).

The DOS near the Fermi edge is due primarily to Co 3*d* electrons. The double peak feature between 2 and 4 eV binding energy seen clearly at lower photon energy is attributed to photoemission from both Cu 3*d*-band and Co 3*d*-band. With higher photon energy, these features becomes less resolved and the Cu 3*d* band contribution less intense compare to Co 3*d* DOS near Fermi edge. This is due to the decrease in the mean free path of photoelectrons emitted from the Cu underlayer. The lack of well defined Cu 3*d* peaks at higher photon energies indicates that there is little or no open Cu substrate exposed on the surface. If there were bare Cu, the ratio of Co and Cu intensities would remain constant with increasing photon energy. The shape of the hν=60 eV spectrum is different from the other spectra. This difference is due to the resonant enhancement discussed in the previous chapter.

A more extensive set of EDC's is shown in figures 4.3 and 4.4. These spectra are taken with circularly polarized light with ~7.4 ML Co/Cu(111). The difference between these two subsets, apart from photon energy range, is that they where taken at different values of the monochromator premirror angle. Those spectra in figure 4.3 were taken with a premirror angle α =77°, while those for figure 4.4, the value of α = 80°. The reason for this is a strong non-flat intensity dependence of photon flux

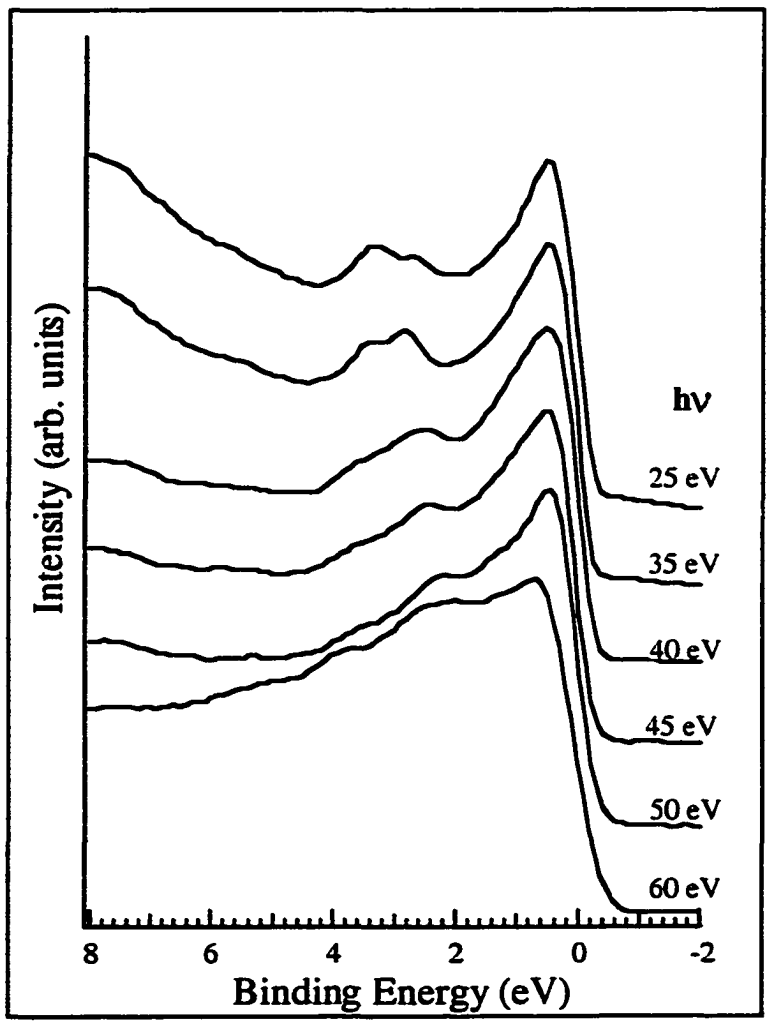

Figure 4.2 Angle integrated photoemission from ~5.2 ML Co/Cu(111). EDCs vs. photon energy.

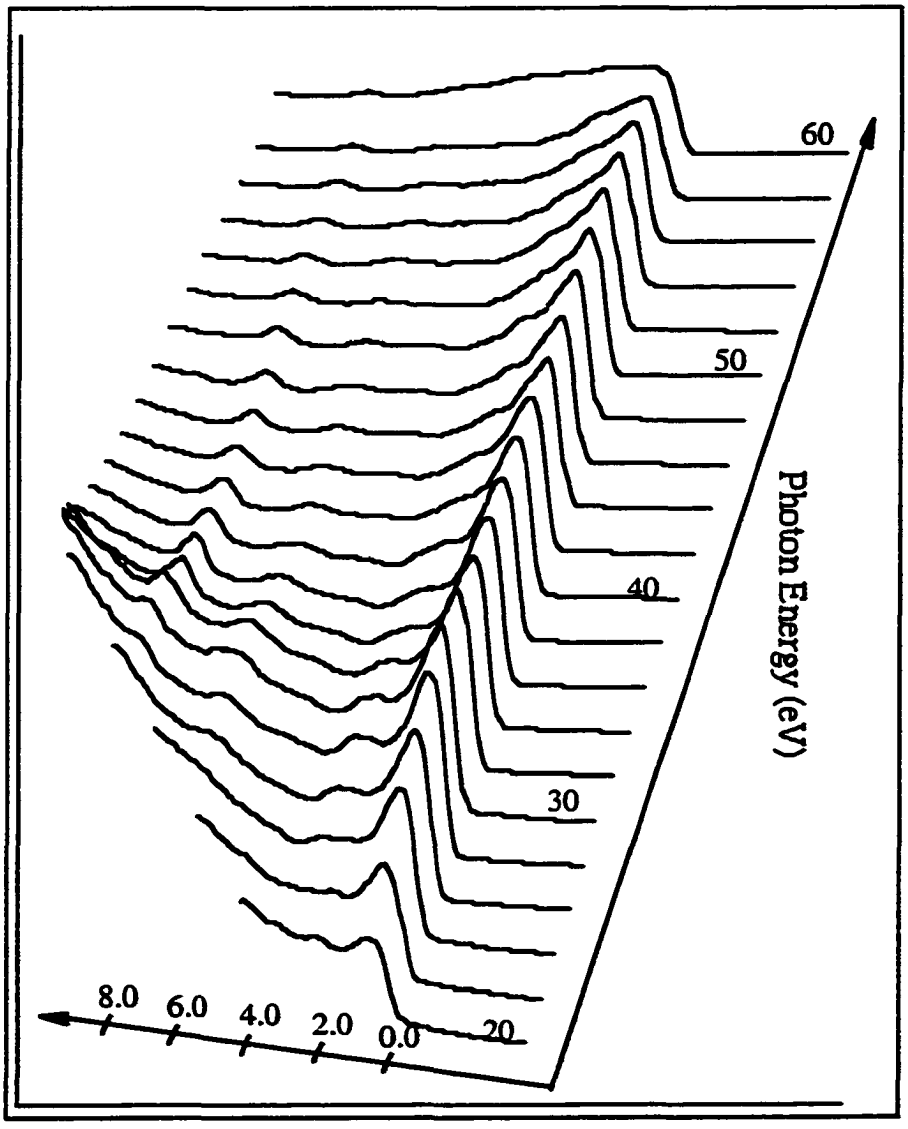

Figure 4.3 Angle integrated photoelectron emission spectra from ~7.4 ML Co/Cu(111) taken with CPL. Part I.

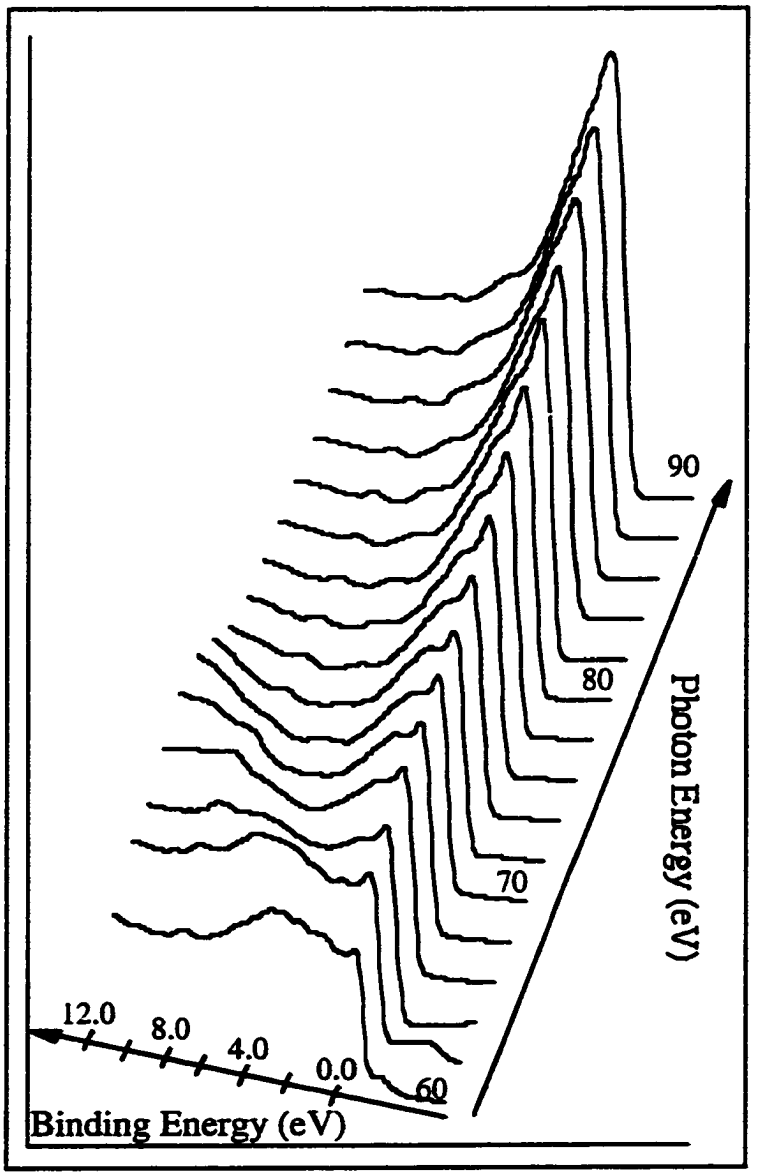

Figure 4.4 Angle integrated photoelectron emission spectra from ~7.4 ML Co/Cu(111) taken with CPL. Part II.

for different values of premirror settings of PGM beamline, especially close to cut off edge at low energies.

The bumps directly above the Fermi edge on the first few spectra of figure 4.4 are due to second order light, i.e. the monochromator transmits higher energy light at multiples of the set energy. Even when all the spectra are normalized with respect to photon intensity it is clearly seen that the spectra for $h\nu = 60$ eV are different in these two figures.

There are two spectral lines, at near 8eV and 11 eV binding energies which are seen at lower photon energies. These lines belong to corresponding σ and π bands of H_2O and CO molecules adsorbed on the sample surface. The effect of residual gas adsorption will be discussed at the end of this chapter.

4.2.2 Angular Distributions in Valence Band PES from Co/Cu(111)

Data on the angular distribution of photoemission from Co/Cu(111) were obtained as described in chapters 2 and 3. Figure 4.5 shows the angular distribution of photoelectron emission acquired with linearly polarized light from 10 ML of Co/Cu(111) with initial states lying close to Fermi edge. The top image, taken at 30 eV photon energy clearly shows six-fold symmetry which we interpret as arising from two families of three-fold spots symmetric with respect to the horizontal plane. The normal at the center of the image corresponds to the ΓLΓ direction of the *fcc* Brillouin Zone. For these photon energies the free electron sphere slices the BZ close to the Γ point. The symmetry of the topmost layer both for *fcc* and *hcp* is hexagonal, so the angular distributions should be six-fold. The symmetry of these spots suggests that the main contribution to the angular distributions comes from 3*d* electrons localized along the main axes with initial state symmetry d_{x^2}, d_{y^2}, and d_{z^2}. Unfortunately, low statistics, limited angular and energy resolution, and most of all, the presence of both

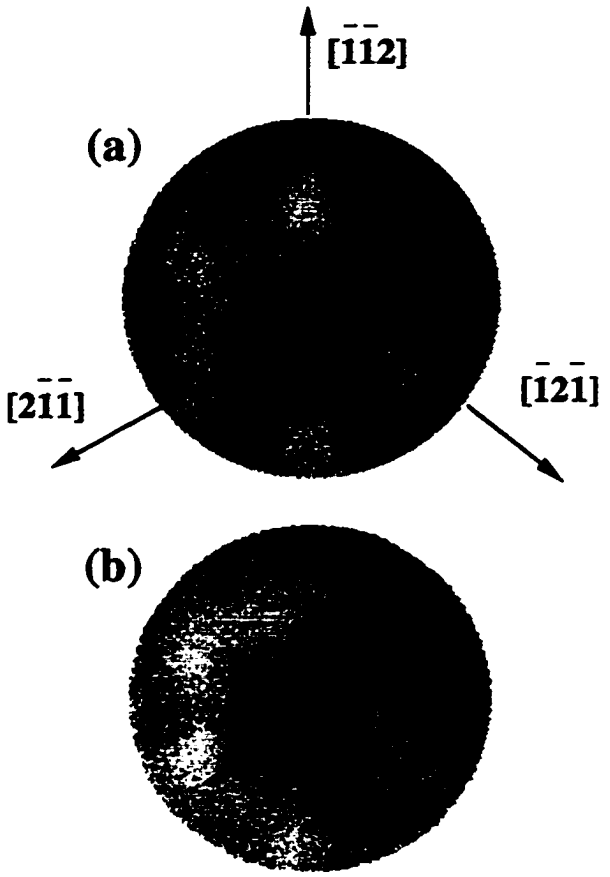

Figure 4.5 Angular distribution in PES from 10 ML Co/Cu(111). Images were acquired with linearly polarized light with photon energy (a) 30eV, and (b) 35eV at the Fermi edge.

phases do not allow us to make a clear distinction between *fcc* and *hcp* features for these ultrathin films.

The bottom image in figure 4.5 corresponds to photoemission angular distribution at 35 eV. This image has also six-fold symmetry, but looks different from the 30 eV image due to the appearance of the arcs connecting the bright areas along the main symmetry directions. These arcs are due to excitation from the 3*d* band with cross term symmetries d_{xy}, d_{yz}, and d_{xz}.

Upgrading the data acquisition hardware and software greatly improved the counting statistics allowing us to obtain more detailed images of the valence band photoemission. Figure 4.6 shows the evolution of the angular distributions of the valence band photoelectrons with the change of the initial state, corresponding to "slices" for different values of the binding energy. The improved statistics allows us to see a quite distinguishable circular feature around the center of the image which can be identified as *sp*-like minority spin band pockets.[75] Dispersion of this feature with change of the initial state creates a parabolloid like feature along the ΓL direction of the *fcc* BZ close to the zone boundary. This finding is similar to what has been observed in high resolution ARUPS from Ni(111) by using unpolarized but highly monochromatic He I/He II UV source.[75]

As a reference, the calculated DOS for bulk *hcp* Co is shown in figure 4.7. The calculations were performed using 'WIEN97' FPLAPW package for calculating Crystal properties.[74] The top panels show majority and minority spin density of states including separately plotted *d*-type DOS for different symmetry *d*-like orbitals. The bottom panel compares majority, minority, and total DOS.

The top panel in figure 4.8 combines DOS for different symmetries of *d*-like bands for minority and majority spins. The bottom panel shows calculated spin

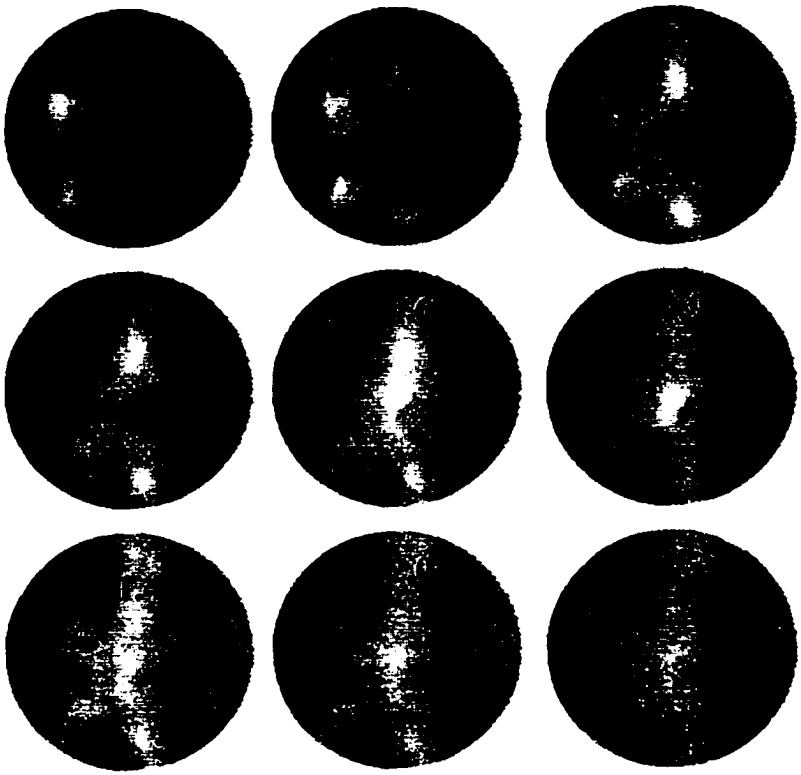

Figure 4.6 Evolution of angular distribution in photoemission from valence band of ~10ML Co/Cu(111)

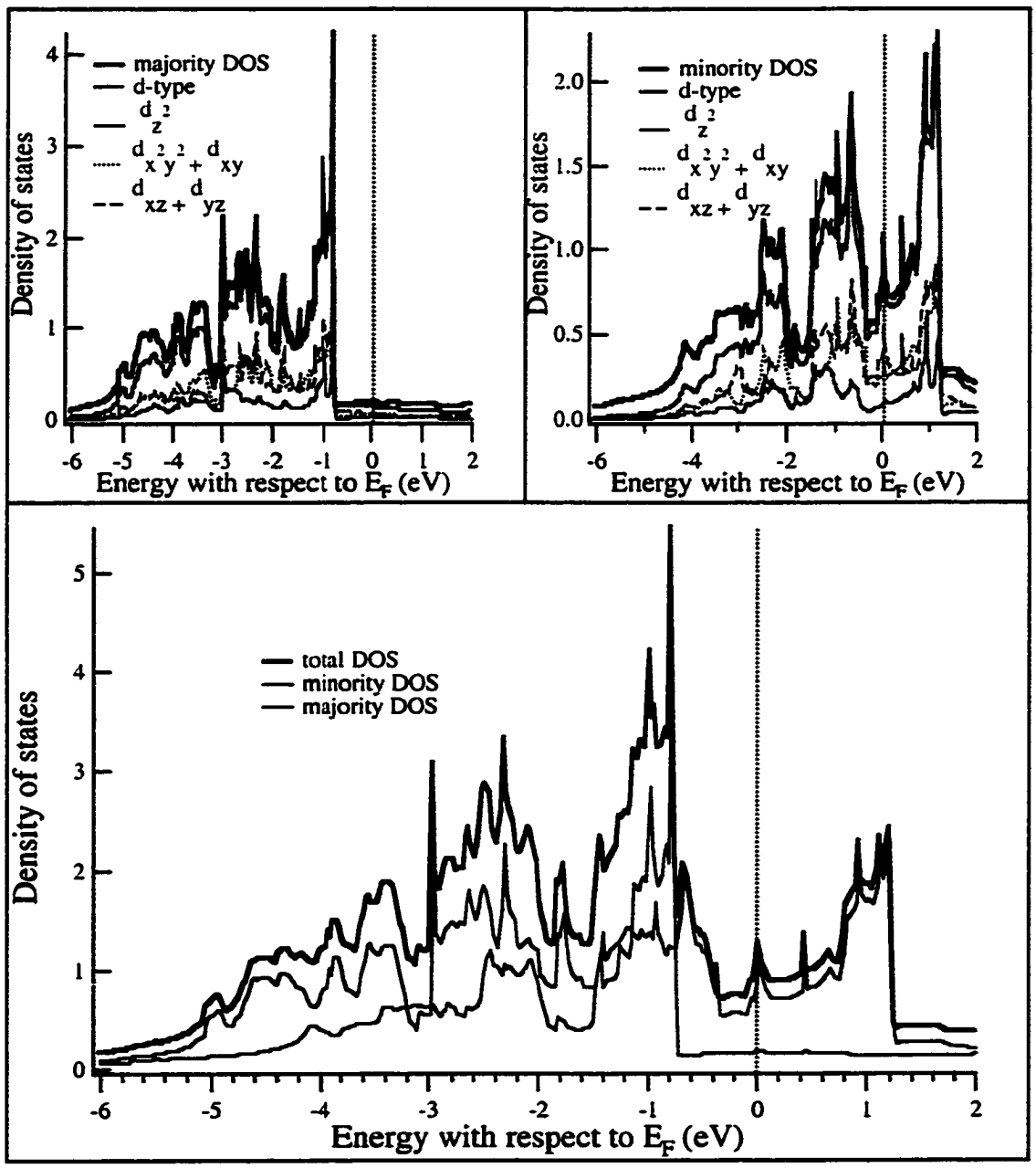

Figure 4.7 Calculated density of states for *hcp* Co. Top panels show minority and majority spin DOS. The total DOS for each case is shown by the thick black line. Thick colored lines show *d* states contributions, thin solid, dotted, and dashed lines represent *d*-type subbands of different symmetries. The bottom panel shows the contribution of majority and minority DOS to the total DOS.

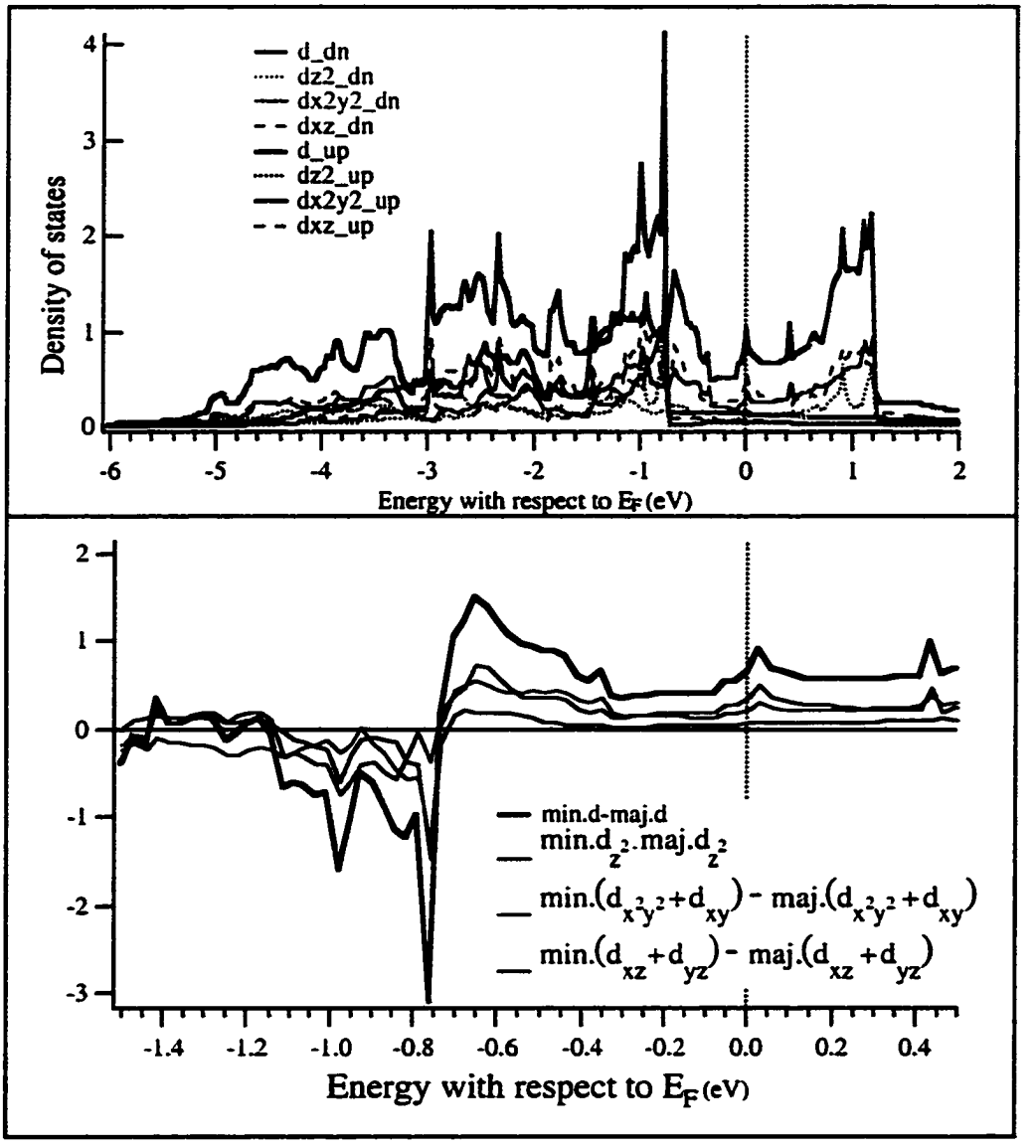

Figure 4.8 Calculated density of states for *hcp* Co. Top panels show minority and majority spin DOS of *d*-type. Thin solid, dotted, and dashed lines represent *d*-type subbands of different symmetries. Bottom panel shows the difference between minority and majority *d* electron DOS close to E_F.

polarization near the Fermi edge. The latter plot will help us to understand observed asymmetries for MCD/MLD experiments in the valence band photoemission.

4.3 Magnetic Dichroism in PES from Valence Band of Co/Cu(111)

The geometry for magnetic dichroism experiment in photoemission from the valence band of Co/Cu(111) remains essentially the same as for Co/Cu(001). Linearly or circularly polarized light enters the EMA chamber and strikes the sample surface at an incident angle of 45°. The plain of incidence coincides with the $[\bar{1}10]$ direction of the Cu(111) substrate, and a horizontal symmetry plane of the sample. The sample was magnetized by applying a magnetic field of 0.8 kOe along the $[\bar{1}\bar{1}2]$ direction which is in the plane of the deposited film and perpendicular to the plane of incidence. The top panel of figure 4.9 presents the angle integrated photoemission spectra from 12 ML Co/Cu(111) over a wide binding energy range with linearly polarized165 eV photons. The solid line corresponds to the "up" direction of sample magnetization ($\vec{M}$) while the dotted line corresponds to the "down" direction. The change in the direction of magnetization was accomplished by rotating the sample by 180° around the sample normal. The spectra are normalized with respect to photon intensity. Rectangular frames outline the areas of interest. The region between 50 and 70 eV binding energy shows magnetic linear dichroism from the Co 3*p* shallow core level, while the region close to Fermi edge represents dichroism in the valence band. The bottom two panels provide more detailed views of the areas of interest combined with corresponding asymmetry plots.

We obtain a value for MLD asymmetry in Co/Cu(111) of ±2% for the Co 3*p* shallow core level. The deviation from zero has both positive and negative signs. The maximum value for the asymmetry in photoemission from the valence band is close to 4% and positioned at a binding energy 0.8 eV. This is consistent with maximum spin

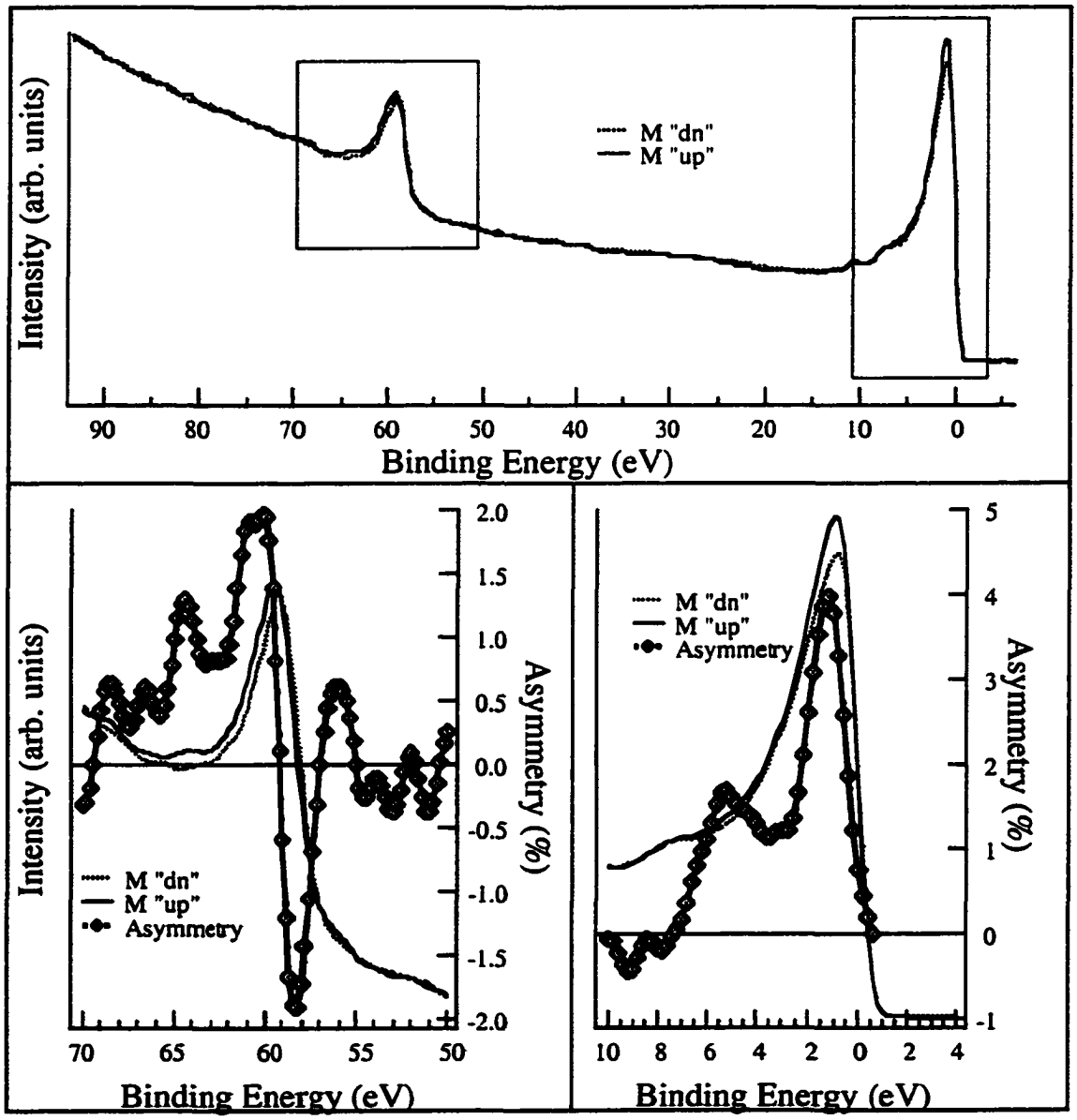

Figure 4.9 Magnetic linear dichroism in angle integrated photoemission in transverse Geometry from ~12 ML Co/Cu(111). Photon energy 165 eV. Top panel shows EDC's for M "up" and M "dn" direction of sample magnetization. Bottom panels show outlined areas of PES spectra and corresponding asymmetries in photoemission from the Co 3*p* levels and valence band.

polarization in our calculations for bulk *hcp* Co DOS, as seen in the previous figure. Figure 4.10 shows spectra from the same sample with identical geometry except, instead of linearly polarized light, circularly polarized light was used. There is an obvious similarity in the shape and values of asymmetries in these sets of data. This indicates that we are dealing essentially with the same phenomenon, namely magnetic linear dichroism.

The studies of magnetic properties of Co films on Cu(111) by means of magnetic circular/linear dichroism in the valence band is more complicated than those of the Cu(001) surface because the C_{3V} surface of the Co film does not have reflection symmetry with respect to the reaction plane. This effect is known as circular/linear dichroism (CD/LD) [20], which means that rotation of the magnetized sample by 180° with respect to sample normal is not, in general, equivalent to reversing the sample magnetization. This simple observation allows us to decouple "geometric" and "magnetic" phenomena. In the first case rotating sample by 180°, both sample symmetry and magnetization effects are combined, while at the second case, we are dealing solely with magnetic asymmetry.

In order to test this effect we have performed magnetic linear dichroism experiments using valence band photoemission on a ~7.4 ML Co/Cu(111) film at hν=30 eV. In the first case we changed the direction of magnetization simply by rotating the sample; in the second case we remagnetized the sample by applying an external magnetic field in the opposite direction. The results of this experiment are shown on figure 4.11. The remagnetization sample, shows a drop in the asymmetry by a factor greater two, compared to the sample rotation. Therefore, the first case is a combination of the MLD and LD, while the second case is "pure" MLD.

The same film was used for imaging the valence band angular distributions with linearly polarized light. In figure 4.12 which shows the images of angular

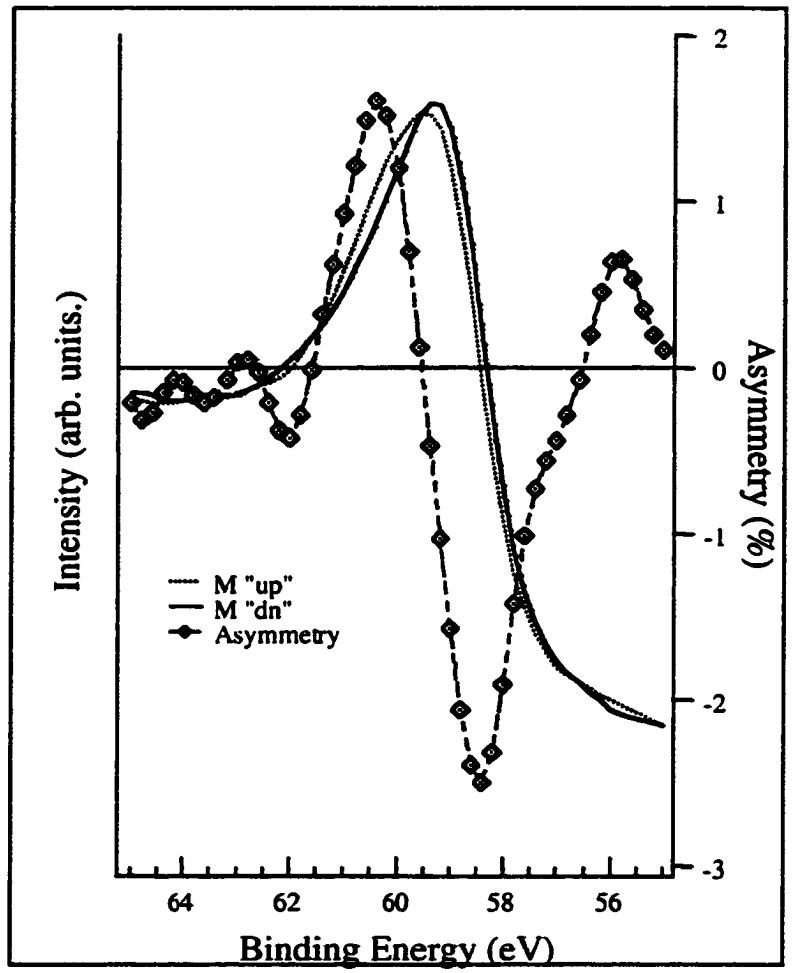

Figure 4.10 EDS's taken with circular polarized light, at hν=165 eV, from Co 3*p* level from in-plane magnetized 12ML Co/Cu(111) in transverse geometry. The corresponding asymmetry is shown as the diamonds.

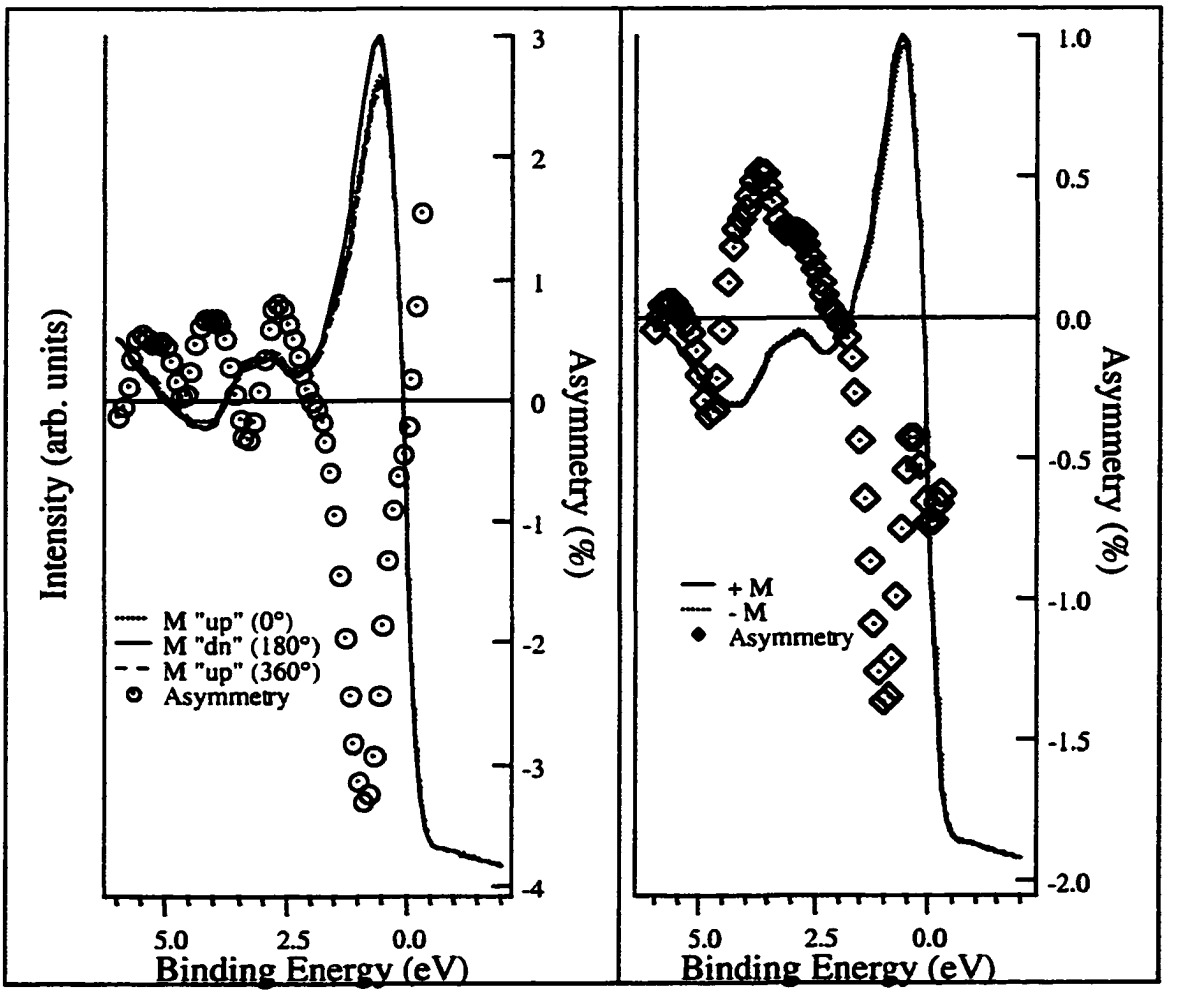

Figure 4.11 Comparison of magnetic linear dichroism (MLD) in angle integrated photoemission from ~7.4 ML Co/Cu(111) at hν = 30 eV in transverse geometry. Panel (a) rotating magnetized sample by 180° and 360°, (b) by changing sign of applied magnetic field.

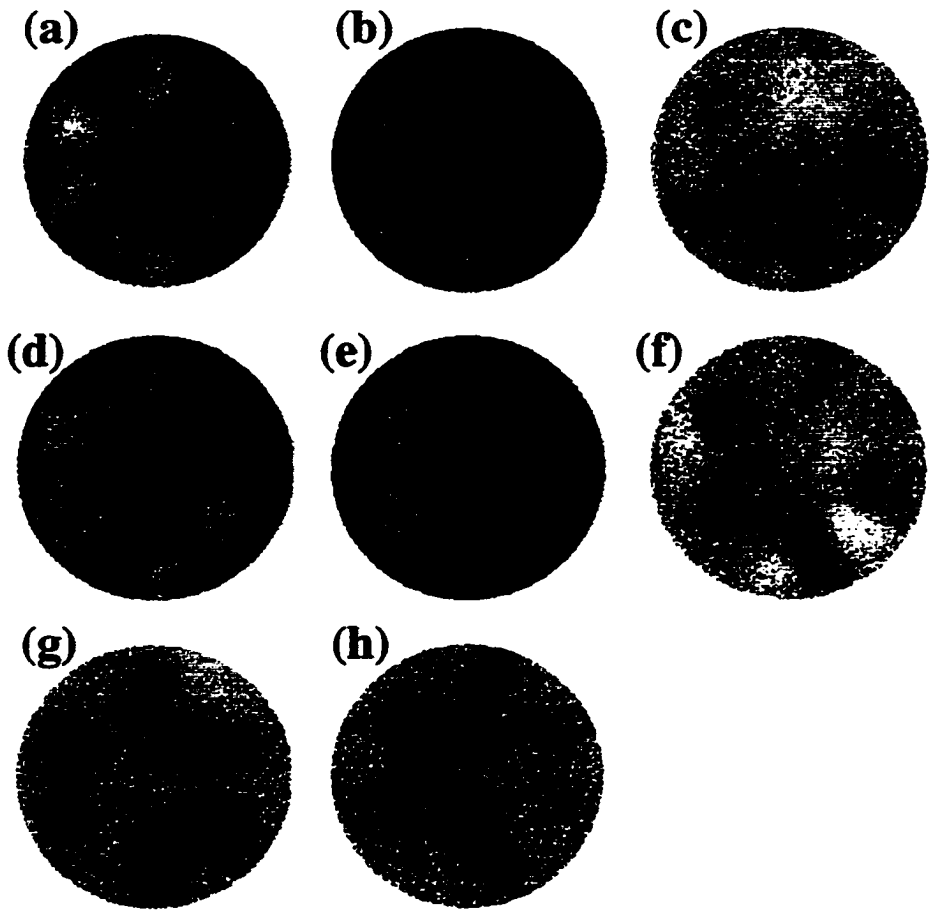

Figure 4.12 MLDAD/LDAD at Fermi Edge of ~7.4ML Co/Cu(111). (a) +M, (b) +M and R(180°), (d) -M, (e) -M and R(180°). (c), (f), (g), and (h) are corresponding asymmetries taken along rows or columns.

distributions, images (a) and (b) correspond to +B external magnetic field, but with the sample rotated 180° in (b), giving a reversed magnetization of the sample compared to (a). In the same manner images (d) and (e) were acquired for –B direction of the external magnetic field with (e) again rotated by 180°. Images (c) and (f) are the asymmetries obtained from the images in the corresponding rows, and represent the case where the change of the direction of magnetization was obtained by sample rotation, resulting in asymmetries that are combinations of both magnetic linear dichroism and linear dichroism in angular distributions. Each of those images was obtained by taking the image difference for images acquired at 0° and 180° and dividing it by sum of them. Images (g) and (h), are the asymmetries from sample remagnetization by an external field, and represent MLD in angular distribution. These images are more symmetric and reflect the symmetry of angular distribution in photoemission itself compare to asymmetries obtained by sample rotation.

Figure 4.13 is another example of magnetic linear dichroism in angle integrated photoemission from Co/Cu(111) obtained with improved statistics provided by the new position computer. In this case a thicker, ~12 ML Co/Cu(111) film was used. The change of the direction of magnetization was achieved by sample remagnetization. It is not surprising that the results look very similar to the previous data set, except for some uncertainty in the determination of the position of maximum asymmetry. During this experiment, we also imaged the angular distributions at different values of the binding energy. Figure 4.14 displays these images for the two directions of magnetization for the Fermi energy, 0.2 eV, and 0.7 eV binding energies. The third row of images shows the respective asymmetries. The *sp* band-like circular feature around the center of the BZ has disappeared in the asymmetries images. Also, one can see that dark spots, which correspond to maximum asymmetry, move towards the center of BZ with increasing binding energy. At 0.7 eV most of the intensity as

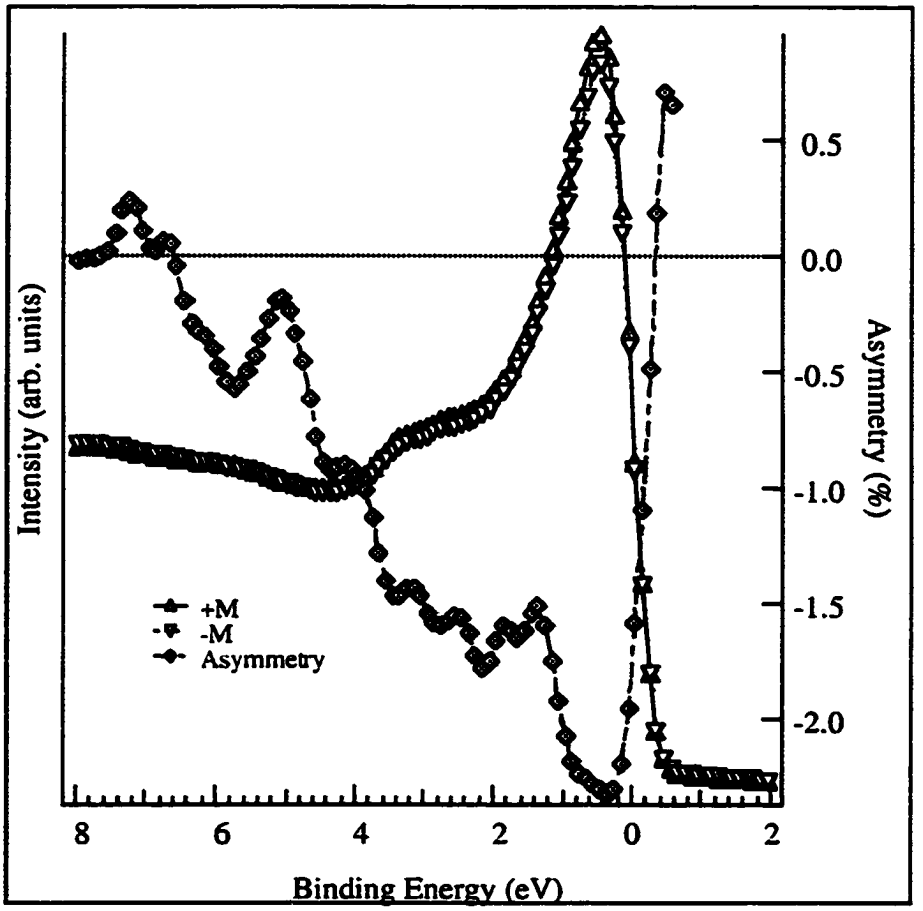

Figure 4.13 Magnetic linear dichroism in the valence band angle integrated photoemission from ~12ML Co/Cu(111). Measurements were done in transverse geometry. Change of magnetization direction was done by reversing the applied field. Photon energy 30 eV.

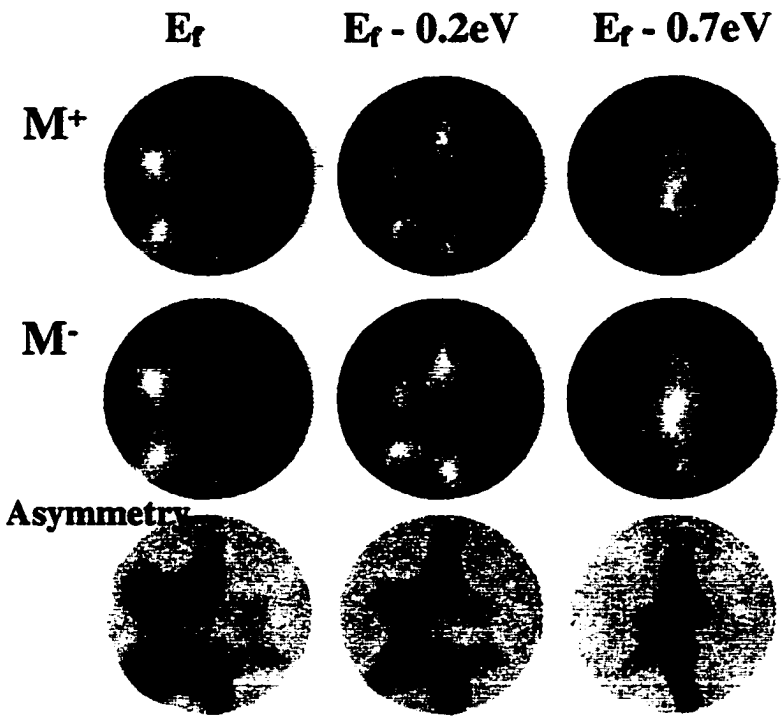

Figure 4.14 Angular distribution and magnetic linear dichroism in angular distribution in transverse geometry for ~12ML Co/Cu(111) taken at different binding energies. Photon energy is 30 eV. Change of sample magnetization was done by reversing the direction of the applied magnetic field.

well as maximum asymmetry are located at center of the BZ. The elongated shape of this spot is in the direction perpendicular to the reaction plane is most probably, due to the offnormal incidence of the light, but not due to direction of magnetization. We have observed a similar feature for a nonmagnetized sample.

A similar experiment was performed with circularly polarized light. These EDC's taken at a photon energy of 30eV from 10 ML Co/Cu(111) film are shown in figure 4.15 along with their asymmetry. The angular distributions at the Fermi edge for opposite directions of $\vec{M}$ obtained by sample remagnitezation are presented in figure 4.16, panels (a) and (b). Image (c) represents asymmetry in angular distribution and obtained by dividing the difference of images (a) and (b) by their sum. An identical set of images taken at binding energy 0.3 eV is shown in figure 4.17. These images and asymmetries are very similar to what we observe with linearly polarized light, including the shift of maximum asymmetry towards the center of the BZ with increasing binding energy. Therefore, we come to the same conclusion as in the previous chapter, namely the character of the angular distribution in photoemission in transverse geometry does not depend on whether we are using linearly or circularly polarized light, but on the geometry of the experiment. Further, in the case of both linearly and circularly light in this geometry we are dealing with the same type asymmetry, which is a manifestation of a more general magnetic dichroism in angular distribution (MDAD).

As was shown in the previous chapter, the asymmetry in photoemission depends on photon energy. This dependence was studied in photoemission from ~12 ML Co/Cu(111) with circularly polarized light. The geometry of the experiment is longitudinal, i.e. the sample magnetization is parallel to the reaction plane. Three sets of data were taken at photon energies 25, 30, and 35 eV. EDC's and the corresponding asymmetries are plotted in figure 4.18. With an increase in photon

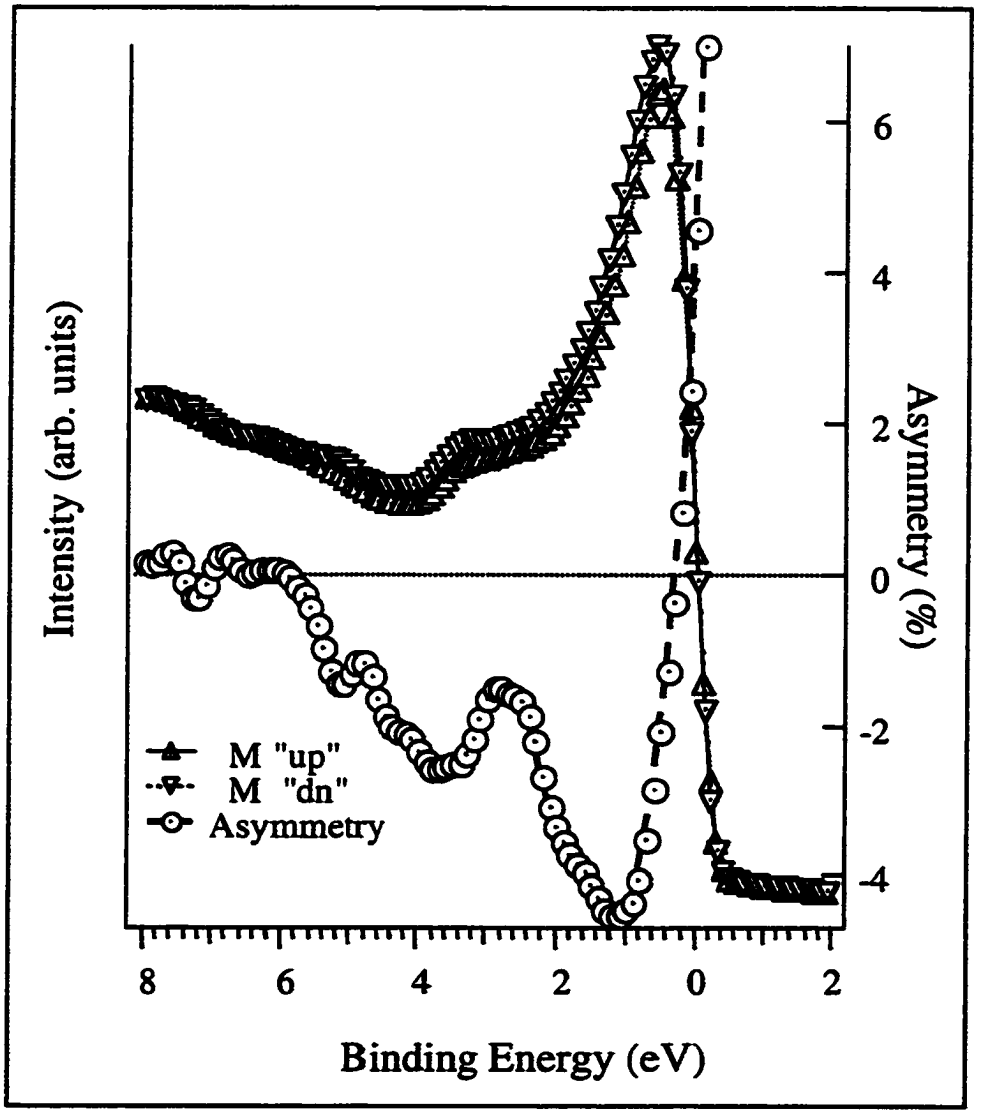

Figure 4.15 Magnetic Circular Dichroism in the valence band angle integrated photoemission from 10 ML Co/Cu(111). Measurements were done in transverse geometry. Solid and dotted curves with the triangles are EDC's for "up" and "down" direction of sample magnetization. The thick line with circles is the corresponding asymmetry.

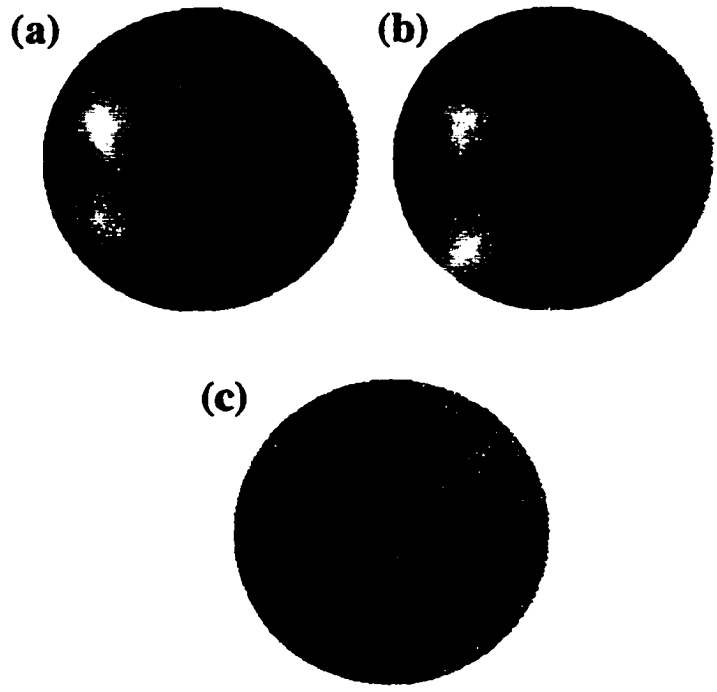

Figure 4.16 Magnetic Circular Dichroism in Angular Distribution images taken with CPL at the Fermi edge on a 10 ML Co/Cu(111) at $h\nu = 30$ eV. Images (a) and (b) are angular distribution in PES for the direction of magnetization "up" and "down". Image (c) represents asymmetry in angular distribution and obtained by dividing the difference of images (a) and (b) by their sum.

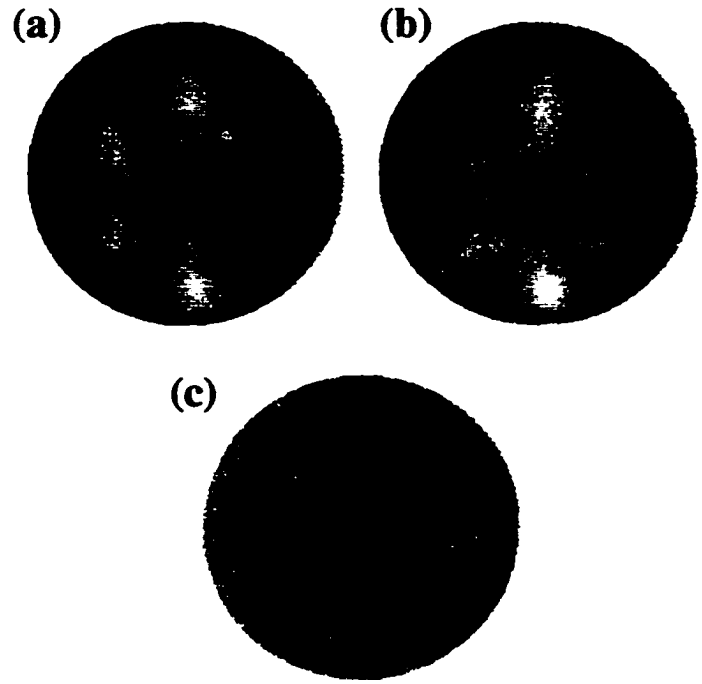

Figure 4.17 Magnetic Circular Dichroism in Angular Distribution (MCDAD) images taken with CPL at E_b = 0.3eV on a 10 ML Co/Cu(111) at hν = 30 eV. Image (c) represents asymmetry in angular distribution and obtained by dividing the difference of images (a) and (b) by their sum.

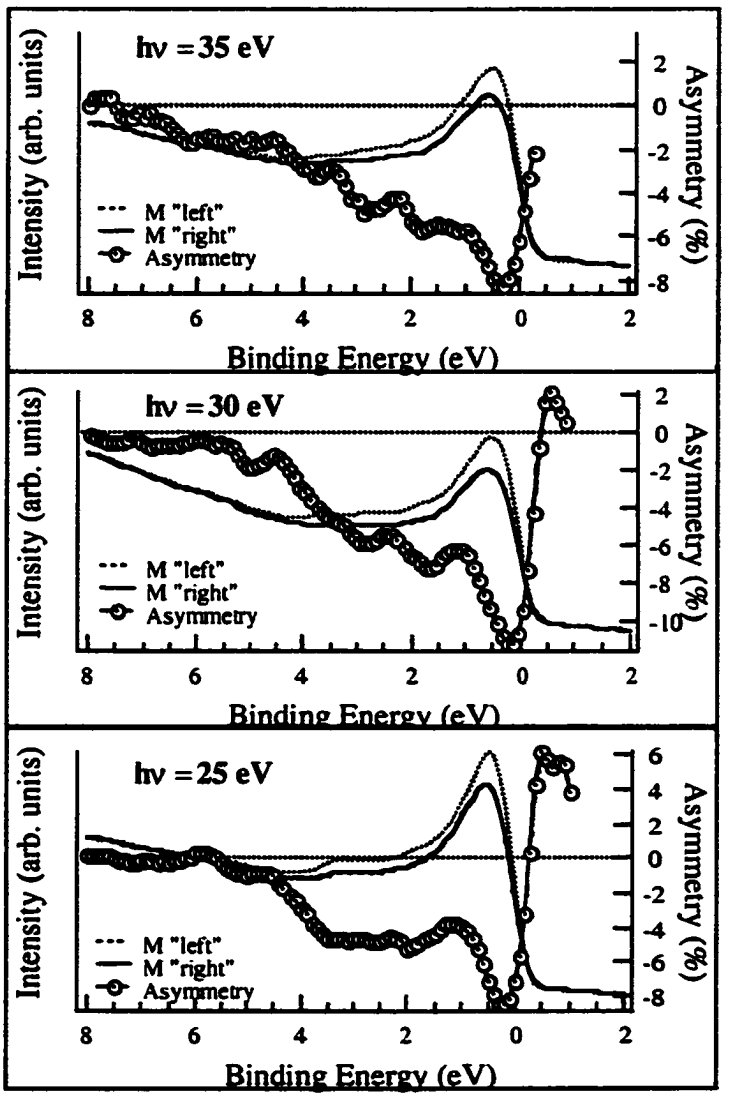

Figure 4.18 Magnetic circular dichroism (MCD) combined with circular dichroism (CD) from ~12ML Co/Cu(111) in longitudinal geometry for different values of photon energy.

energy from 25 to 30 eV the maximum value for asymmetry in MCD/CD increased from 8.4% to 11.1%, corresponding to a 24 % increase. Further increase of the photon energy leads to a decrease in the asymmetry. The position of the asymmetry maximum is near 0.25 ± 0.1 eV binding energy and shows a large shift (more than 0.5 eV) towards the Fermi edge, compared to the transverse geometry experiment. Data on photoemission with linearly polarized light in transverse geometry from the same film are shown in figure 4.19. In this case the maximum value for the asymmetry monotonically decreases with increasing photon energy over the energy range investigated. The changes in the shape of the photoemission spectra, the shift of the asymmetry maximum, and the different character of the energy dependence for maximum asymmetry indicates that the symmetry of the initial state probed in these two experiments is different. More detailed PES studies with higher energy resolution as well as theoretical calculations for optical matrix elements and probabilities of photon excited electron transitions are needed to clarify this issue.

4.4 Effect of Residual Gases on PES from Co/Cu(111)

As it was mentioned in the beginning of this chapter, even at UHV condition, the amount of time required to obtain the data plays an important role in these experiments. Sample contamination is always a consideration in surface science experiments. To quantify these effects surface scientist use a unit of coverage called a Langimouir (L) which corresponds to a surface covered by 1ML thick adsorbate. This may be estimated in terms of time and pressure in a UHV chamber. Making two approximations about constant number of absorbing sites per surface unit cell, and constant sticking coefficient equal to 1, the flux of residual gases molecules hitting the surface at the pressure 10^{-6} Torr approximately equals 1L/sec. With a vacuum

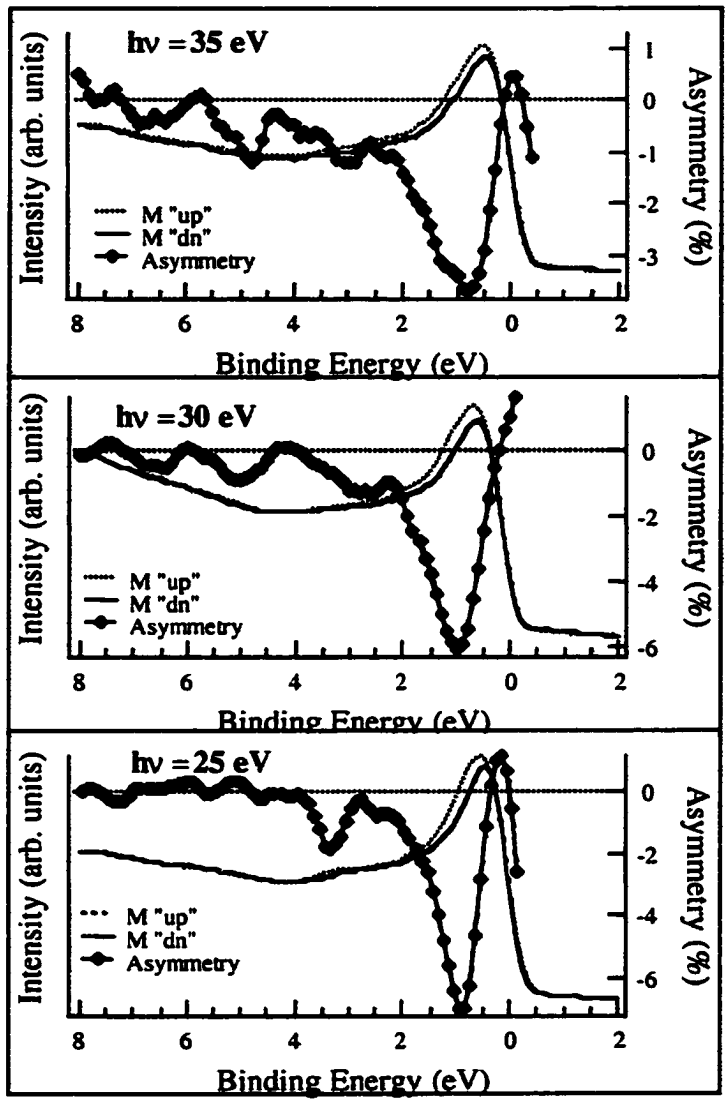

Figure 4.19 Magnetic linear dichroism (MLD) combined with linear dichroism (LD) from ~12ML Co/Cu(111) in transverse geometry for different values of photon energy.

improved to 10^{-10} Torr, the time needed for a 1L coverage becomes 10^4 seconds or 3 hours and 20 minutes.

To study the effects of surface contamination, data from a 12 ML thick Co/Cu(111) film were obtained with linearly polarized light. Angle integrated spectra were taken from the sample soon after Co deposition as well as images of angular distributions for different values of binding energy. The sample was then left in the EMA chamber at a vacuum of $1.2 \cdot 10^{-10}$ Torr for 24 hours resulting in approximately 10L exposure to residual gases. Mass-spectrometry of the residual gasses shows that the main gas component inside the chamber is CO, with some H_2O. The PES measurements were repeated, and the results are shown in figure 4.20. Two well-defined peaks near 8 and 11 eV binding energy were identified as $4\sigma^+$ and $5\sigma^+$ molecular orbitals of CO. The literature values for the binding energy of these orbitals on Co(0001) are 10.75 eV and 8.2 eV.[76] The $2\pi^-$ nonbounding orbital of CO overlaps the 3*d* band of Co causing a strong decrease of PES intensity from the Co *d*-band near 1 eV binding energy. Images of the angular distributions with arrows indicating the binding energy of the initial state are shown as inserts on the same figure. Red arrows indicate images of angular distribution acquired before the exposure, and blue arrows after. The comparison of images for angular distribution of photoelectrons reveals no significant change in shape or symmetry of those images taken before and after exposure. Still, there is an enhancement in photoemission close to the center of BZ from the contaminated film at binding energies below 0.5eV. This fact can be explained in terms of charge transfer due to weak Van-der-Walls type interaction between substrate and molecules of adsorbate gas in the direction perpendicular to sample surface. Data from MOKE and MXCD experiments, show relative stability of magnetization of Co films compared to Fe.

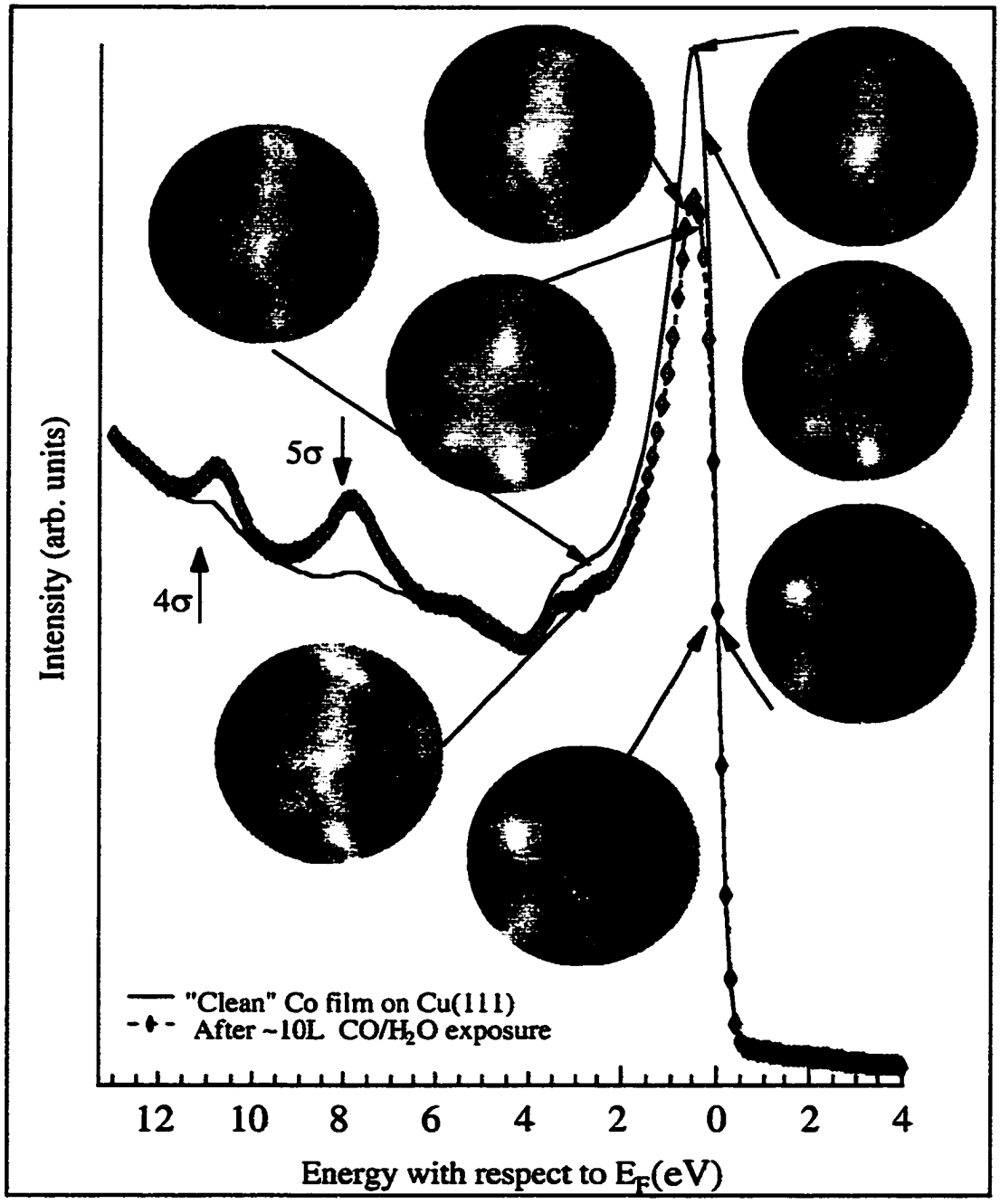

Figure 4.20 Effect of 24 hrs exposure of ~12 ML Co/Cu(111) film to residual gases. Estimated flux is approximately 10 Langimuir of CO plus H_2O. $h\nu = 30$ eV. Inserts show corresponding images of photoelectron angular distribution.

4.5 Conclusions

Co films grown on Cu(111) also exhibit pseudomorphic fcc growth but eventually develop hcp stacking faults before growing completely hexagonal. This is a particularly interesting case, however, since the easy axis of magnetization in bulk hcp Co is along the hexagonal direction. In its fcc form, one might expect Co to behave something like fcc Ni which has its easy axis along the [111] direction as well. In the case of thin-film Co, however, the magnetization is locked in-plane by the film's shape anisotropy and there is no strong anisotropy within the plane. This allows us to change the magnetization along the $[\bar{1}\bar{1}2]$ and the $[11\bar{2}]$ directions.

As discussed in the previous chapter for Co(001), Co(111) exhibits a photoemission process for photon energies that exceed the $3p$ excitation threshold. Again, we will avoid this effect by choosing photon energies well below the threshold to perform magnetic dichroism experiments.

The first difference that one notes in the angular distributions from Co/Cu(111) is that the valence band photoemission exhibits a sixfold-like pattern which can be attributed to the presence of two threefold families of the features in the pattern. The symmetry of the substrate surface belongs to the C_{3v} point group and that means that the plane of the incidence (reaction plane) is not a mirror plane of symmetry. In spite of this, there are significant polarization dependencies in the photoelectron angular distributions. Furthermore, the angular distributions patterns depend strongly on the initial state binding energy, as one would expect when higher binding-energy bands are measured.

Throughout all of the dichroism studies, one must consider the experimental geometry carefully. Furthermore, we expect that our selection of circularly polarized

light by the method described in chapter 2 will also include a linear component which must be considered in interpretations of the results.

Although our experiments on the Co/Cu(111) films are primarily focused on the valence bands, we did undertake some measurements of MLD and MCD from the 3p levels in a transverse geometry. As with all MCD measurements, the best opportunity for dichroism is found when the magnetization, **M**, is aligned with the incidence direction, **q**, of the photon. In accord with our expectation, the dichroism signal of 2.5% from MCD is nearly equivalent to the 2% from the MLD, suggesting that the MCD dichroism arises mostly from the linear component in the measurement.

A general trend of the valence band dichroism that we have observed in the transverse configuration is the small size of the effect, 2 – 4%. This applies to both MLD and MCD measurements. In fact, the dichroism that arises with the use of circularly polarized light is likely to be due to a linear component, effectively giving an MLD signal, since in this geometry the photon incidence direction, **q**, and the magnetization, **M**, are mutually orthogonal.

The longitudinal configuration is different. Here we observe a 7 – 9% effect, depending on the photon energy used and for MLD at the lowest photon energy, 21 eV, a 15 % effect is seen. In this case, one expects any linearly polarized light in the sample plane to give a zero MLD signal since the magnetization **M** is parallel to the polarization vector **A** of the linear component of the light. However, a vertical component (along the sample normal **n**, called "*p*"-polarized) will give a linear dichroism signal.

The longitudinal MCD measurements also show significant dichroism which is consistent with a real MCD effect: the sample magnetization, **M**, now has a significant component projected along the photon incidence direction, **q**. Quantitative

comparisons of the percentages of each contribution to the total dichroism signal will be made with ongoing first-principles calculations.

In addition to the expected dichroism effect due to the sample magnetization, we also have another effect that can give rise to asymmetries in our angle-integrated spectra. This effect involves the change in the experimental symmetry when the C_{3v} sample is rotated by 180° to flip **M** compared to the case where the magnetization is reversed with a field and the sample is not rotated. The former case gave a factor of 2 larger asymmetry in the data than the latter case did. We expect that this is an effect that future calculations should be able to reproduce. Another general trend in the dichroism data can be seen by comparison of the different asymmetry curves for MCD *vs.* MLD in the angle-integrated spectra. EDC's for opposite direction of magnetization show that the centroids of the peaks in Co 3*d* PE with CPL are not shifted with respect to each other, and this gives rise to a dichroism signal which is largest at the centroid of the Co 3*d* peak. In the case of LPL in transverse geometry the EDC's are shifted on the order of 0.2 eV and this gives rise to a dichroism signal with the largest magnitude at a higher binding energy than the average peak position. In addition, the width of the asymmetry in that case is much narrower compared to that from CPL. These observations are linked to the origin of the dichroism phenomenon and the differences between linear and circularly polarized light. In the case of linearly polarized light, we are essentially measuring the exchange splitting, which is reflected in the separation of the minority and majority bands. This gives a difference in the spectra which reflect the exchange splitting of the bands, and peaks appear at different energies. When circularly polarized light is used, different selection rules apply. In that case, absorption of the photon's angular momentum requires $\Delta m_j = \pm 1$ and this means that spin-orbit coupling plays a role in determining allowed transitions. Since the spin-orbit splitting in 3*d* transition metals is small, the

energy changes are also small. This gives rise to dichroism spectra that change in intensity but not in energy.

Finally, the effect of residual gas exposure on the valence bands of Co/Cu(111) was studied. Physically adsorbed molecules of CO and H_2O can affect the overall intensities in the photoelectron angular distributions. Even though other groups using MXCD and MOKE measurements conclude that exposure to residual gases at UHV conditions does not affect the magnetization of the sample[77], we do see changes in the angular distributions from the Co 3*d* bands, presumably reflecting the charge transfer that occurs when these molecules bond to the substrate. For this reason, we feel that this effect should be monitored carefully while dealing with valence band photoemission studies of magnetic materials.

Chapter 5

Fe and Oxidized Iron Films on Cu(001)

5.1 Thin Films of Iron on Cu(001)

In ultrathin metal-on-metal films, crystal structures that are not normally accessible at room temperature can often be stable. In Fe films grown on Cu, an fcc-like pseudomorphic phase grows at low film thicknesses and this new structure and different atomic volume give rise to interesting magnetic phenomena.[78]

Several studies indicate that the formation of ultrathin layers of Fe on the Cu(001) substrate is pseudomorphic. This means that the usual *bcc*-Fe is growing as *fcc*-Fe on Cu(001). For thicknesses beyond 10-12 ML it reportedly reverts to bulk-like *bcc*-Fe.[30] *Fcc*-Fe and *fcc*-Cu have lattice constants of 3.58 Å and 3.61 Å respectively.[79] Previous studies of Fe/Cu(001) system indicated that the small ~1% lattice mismatch results in a tetragonally distorted Fe film on the Cu(001) substrate at low Fe coverage.[30] This tetragonal distortion is a result of the expansive stress, causing the *z*-dimension to compress.

Although the precise growth mode depends on deposition technique, ultrathin Fe films grown epitaxially on Cu(001) at room temperature have been observed to exhibit both layer-by-layer growth as well as a certain amount of 3D islanding.[30, 32, 80] The *e*-beam deposited films which exhibit a deviation from layer-by-layer growth, are shown by medium energy electron diffraction studies to exhibit some second layer growth before the first layer is complete.[31] Scanning tunneling microscopy (STM) studies showed that nucleation and growth of the second ML of Fe starts from a total coverage of about 0.5ML.[30, 33] These observations are consistent with our own

STM studies. At thicknesses above 2 ML the growth appears to be mostly layer-by-layer.

Several experiments have observed that structural and magnetic transitions in Fe/Cu(001) occur at different film thicknesses.[30 - 33] From 0 to about 5 ML the MBE-grown Fe films are ferromagnetic (FM) with a tetragonally distorted *fcc* structure, also known as *fct*, corresponding to an increased atomic volume of ~6%.[31, 32, 34]

At 5 ML, there is a precipitous drop in the perpendicular magnetization, which is thought to reside in a "live" surface layer. From 5 to 11 ML the Fe film is undistorted fcc and, except for the surface "live" layer, is antiferromagnetic (AFM). For Fe coverages of more than 11 ML *fcc* Fe becomes unstable and transforms into the bulk FM *bcc* Fe.[31]

The sensitivity of the *fcc* Fe moment to atomic volume was investigated by Bagayoko and Callaway [81] who found that the electronic band structure, and hence magnetic moment, depended critically on atomic volume. At larger Wigner-Seitz radii, they found that the exchange splitting increased, with an increasing occupancy of a significant portion of the *d*-electron majority-spin bands. Recent total energy calculations for various configurations of the spin orientations in multilayer Fe found that the equilibrium magnetic structure depends critically on volume and symmetry, with several different ferromagnetic (FM) and antiferromagnetic (AFM) configurations in close energetic competition.[82] Asada and Blügel conclude that of all possible collinear spin configurations of monolayers of *fcc* Fe on Cu(001), 1-3 ML *fcc* Fe are FM while thicker layers have AFM-coupled bilayers of parallel orientation. With an odd number of layers, the top layers' magnetization gives the film a net moment.

5.1.1 Photoemission Studies on Fe/Cu(001)

Ultraviolet Photoelectron Spectroscopy (UPS) will be used in this chapter to study the evolution of the valence band structure of ultrathin Fe films deposited on Cu(001), as a function of increasing Fe coverage in the 0-15 monolayer range. Momentum-resolved and angle integrated photoelectron spectroscopy was used to probe the valence electronic structure and to extract Fermi surface contours as a function of increasing Fe coverage.

Figure 5.1 (a) shows the angle-integrated EDC's for emission from the 3*p* core levels of Fe and Cu using 165 eV photons for clean Cu and a series of Fe coverages. The $3p_{1/2}$ and $3p_{3/2}$ spin-orbit split, shallow core levels are clearly visible for the pure Cu at 77.3 eV and 75.1 eV respectively. The intensity of the Cu 3*p* peaks decreases considerably and eventually disappears as more Fe is deposited on the Cu substrate. The uniform and almost complete attenuation of the Cu 3p peak indicates that there is little or no interdiffusion or alloying between the two species. The film thicknesses were estimated using equation (A3.1) (see for details appendix A3) assuming the mean free path $\lambda = 2.7$ ML. These were consistent with estimates from the quartz-crystal deposition rate monitor.

In figure 5.1 (b), angle–integrated photoemission curves for varying thicknesses of Fe/Cu(001) are presented using $h\nu = 90$ eV. The bottom curve shows the spectrum for clean Cu, which has a low density of *sp*-like states at the Fermi level, E_F. The Cu 3*d*-electron bands give the prominent peak between 2 and 5 eV binding energy.

When Fe films are deposited several changes occur. An enhanced DOS appears at E_F, corresponding to Fe 3*d*-electrons, and additional features appear at higher binding energy. The Cu *d*-band is attenuated and is unseen in the thickest

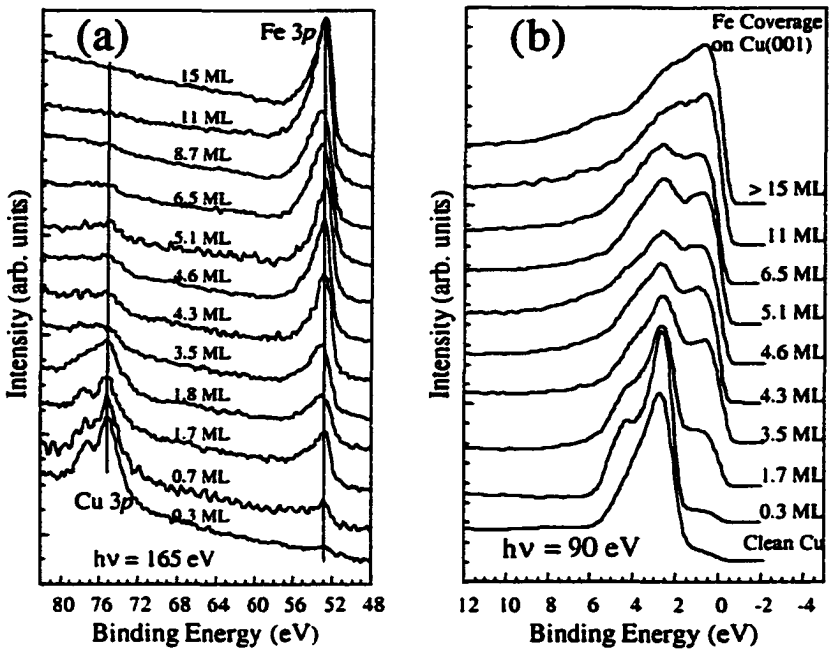

Figure 5.1 (a) Photoemission spectra at hν = 165 eV for Fe films on Cu(001). (b) Angle-integrated photoelectron energy distribution curves of the Cu and Fe 3*d* valence bands at hν = 90 eV for clean Cu, and a series of Fe overlayer films.

films. The spectra from the 15 ML films are essentially identical to those from bulk Fe. At the 0.3 to 4 ML film thickness, a distinct shoulder is seen at about 4.5 eV binding energy that is less evident at higher coverages.

In order to extract more information from these data, one can produce difference spectra that are shown in figure 5.2 for 1.7 and 6.5 ML Fe coverages. These spectra are produced by estimating the attenuation of the Cu substrate by the overlying Fe film, scaling the clean Cu spectrum, and subtracting it from the spectra of Fe-covered surfaces. In addition, a smooth background of inelastically-scattered electrons has been removed from these difference curves. This effectively provides a spectrum giving the Fe-induced changes in the surface density of states.

In figure 5.2 (b) and 5.2 (c) these difference curves are presented as well as those which would arise from ±20% errors in our coverage estimates. The 6.5 ML difference curve shows a spectrum that is similar to calculated bulk *fcc* Fe electronic density of states while the 1.7 ML curve shows more structure. On first glance, one might conclude that the 1.7 ML film looks *bcc*-like, but an alternative possibility is that the bulk *bcc* band-structure is a poor description of this film. Indeed until slab calculations are performed, it is premature to make definitive assignments.

To better understand the difference between these electronic structures, we have calculated the bulk band structures for both bcc and *fcc* Fe figure 5.3 (a) and (b), and the density of states for these structures appear in figure 5.2 (d) and (a). The lattice constants used in the *fcc* is 3.58Å while the *bcc* parameters are those of bulk Fe (2.87Å).

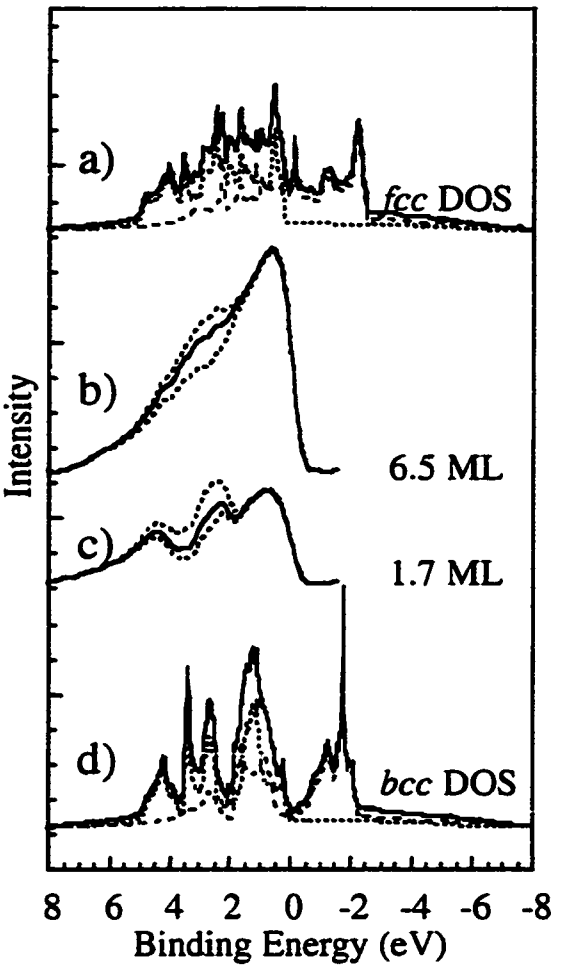

Figure 5.2 (a) Density of States (DOS) for bulk *fcc* Fe. Blue line gives the majority spin DOS, and the red line gives minority spin DOS. (b) Difference spectra obtained for 6.5 ML Fe on Cu(001). Dashed curves represent estimated variations in Cu attenuation, corresponding to a variation in thickness ±20%. (c) Difference spectra obtained for 1.7 ML Fe on Cu(001). (d) Density of States (DOS) for bulk *bcc* Fe.

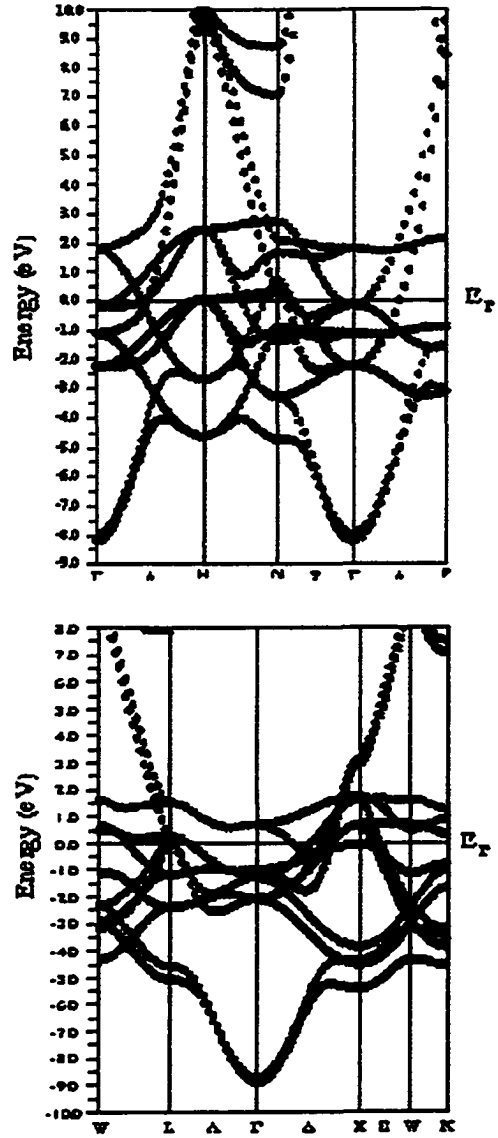

Figure 5.3 FPLAW spin-polarized band structure calculations for (a) *bcc* Fe, lattice parameter 2.87Å, and (b) *fcc* Fe, lattice parameter 3.58Å. Blue lines correspond to majority spin bands, red lines - minority spin.

5.1.2 Fermi Surface Mapping

Additional information on the electronic changes that are occurring can be extracted from measurements of Fermi surface contours as a function of film thickness.

The observation of bulk-like Fermi surface contours in atomically thin films has been observed previously for Ni and Co on Cu(001), supporting our comparison with FS contours from bulk calculations.[64] Although the experimental contours are rather diffuse for Fe on Cu(001), these data suggest that an electronic transition occurs commensurate with a structural change in the Fe.

Figure 5.4 (a) shows photoelectron angular distribution images of the Fermi surface of a 4.2 ML Fe film compared with that from an 8.7 ML Fe film, both taken with hν=75 eV. The photons are linearly polarized in the horizontal plane i.e., the [010] azimuth of the crystal. The data have only been corrected for channel plate efficiency and are plotted on a linear intensity scale, with the whitest feature representing maximum photoemission intensity and the darkest feature representing minimum intensity. Ideally the image should show sharp contours of intensity. Broadening of the structure in the images can be due to both energy (lifetime) and wave-vector effects as well as imperfections in the structure of the overlayer film. In the panel (b) of figure 5.4 these images are were symmetrized and overlaid with the FS contours predicted by FLAPW calculations for the *bcc* and *fcc* Fe.

The image from 4.2 ML Fe film shows distinct features in the [110] directions as well as normal-emission intensity. As the film thickness increases, these local intensity maxima appear to be rotated by 45°, resulting in shows distinct intensity in the [100] azimuths in the 8.7 ML image. The theoretical contours overlaid on the

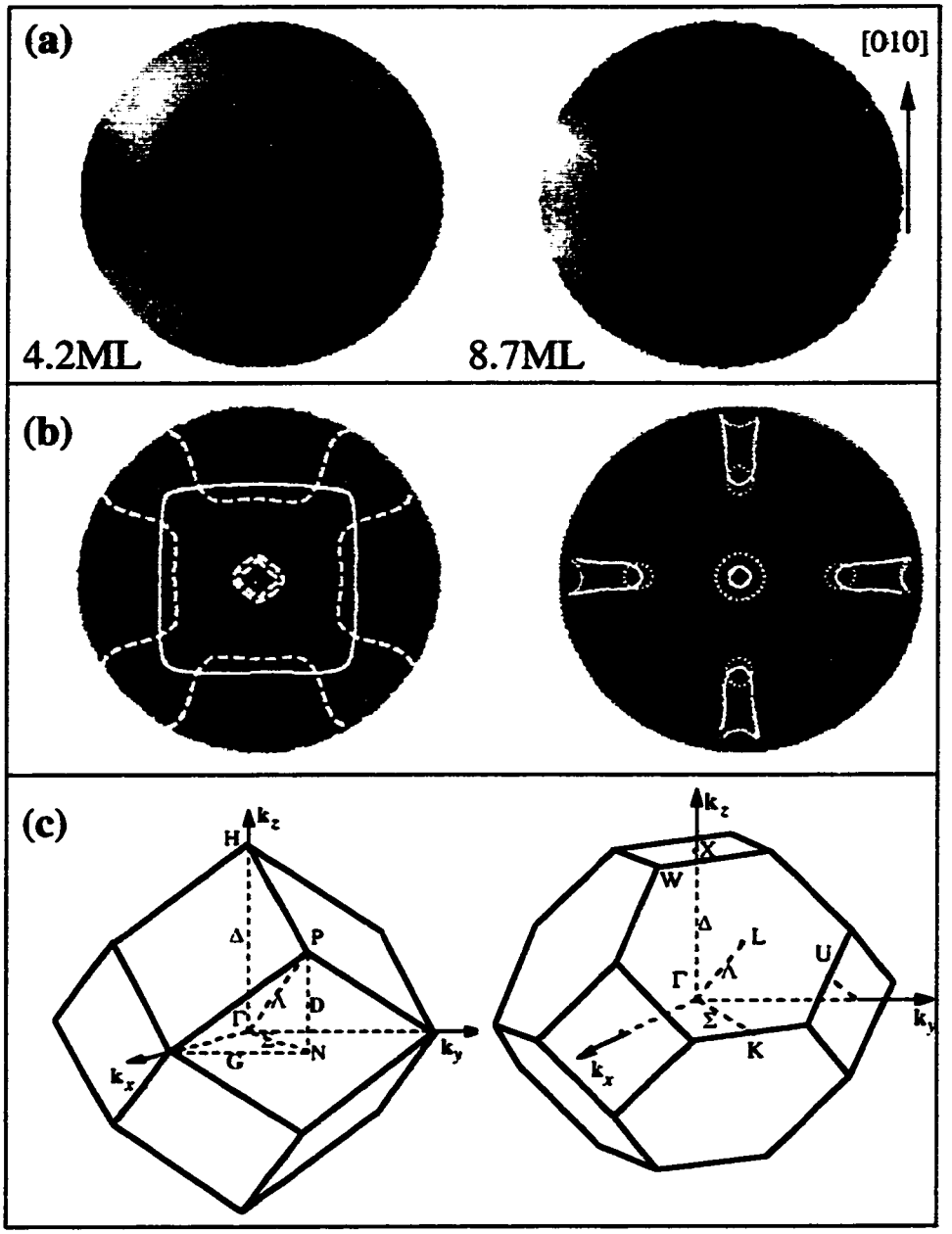

Figure 5.4 Angular distributions in photoemission from 4.2 ML and 8.7 ML Fe/Cu(001). Photon energy 75eV. Panel (a) shows original data, (b) - symmetrized data overlaid with calculated FS contours, and (c) BZ for *bcc* and *fcc* lattices.

images in (c) suggest that a rotation of intensity maxima can be associated with a structural change.

Figure 5.5 presents the angular distributions in photoemission at photon energy 90 eV. Panel (a) shows the image taken from 4.2 ML film at the Fermi edge, (b) image from 8.7 ML film, also at E_F, and (c) angular distribution of photoelectrons with initial state equal to a binding energy of 2 eV from 4.2 ML Fe/Cu(001). The sharp distinct angular distribution from 8.7 ML film is representative of the well defined *fcc* structure of the Fe film, while the ill-defined image from 4.2 ML film results from poorer long range order for the film. The angular distribution in figure 5.5 (c) shows mostly structure from the underlying Cu 3*d* bands, which still show the sharp X-like feature representative of *fcc* Cu. This shows that the overlayer exhibits more disorder than the substrate.

Another result that can not be explained from *fct-fcc* structure below 5ML is the in-plane magnetization of the film, while *fct* Fe structure has **out-of-plane** magnetization.[32] Figure 5.6 presents magnetic linear dichroism in photoemission from 3.7 ML Fe/Cu(001), magnetized in-plane, with a photon energy of 165 eV. Inserts in the panels (b) and (c) show the corresponding asymmetries.

Recent atomic resolution STM studies by Biedermann *et al.* [83] shows (110) *bcc* like nucleation in 3-5 ML Fe films e-beam deposited at room temperature on Cu(001) substrate. This fact may explain such a crucial difference in images for angular distribution as 45° rotation, that we have observed (figure 5.5), as well as the presence of in-plane magnetization for 3.7 ML Fe/Cu(001), which was observed by MLD both in Fe 3p level and in valence band.

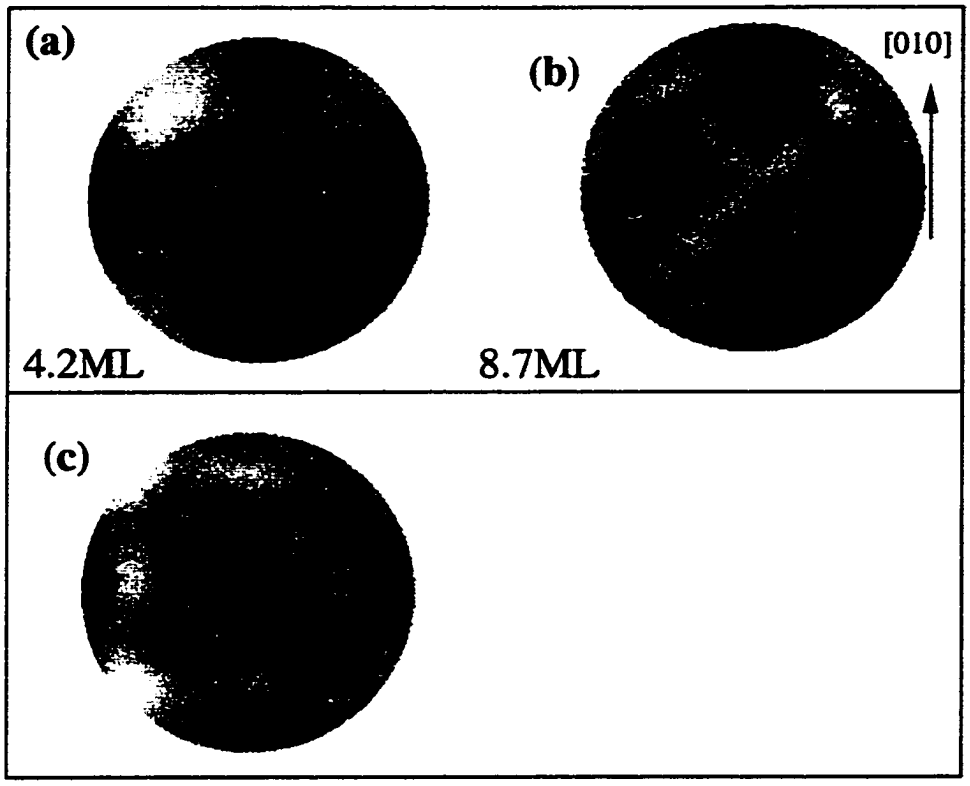

Figure 5.5 Angular distribution in photoemission at a photon energy of 90eV. Panel (a) image taken at Fermi edge from 4.2 ML Fe/Cu(001), (b) 8.7 ML Fe/Cu(001). Panel (c) represents the angular distribution from sample (a) an initial state energy of E_F-2.0 eV.

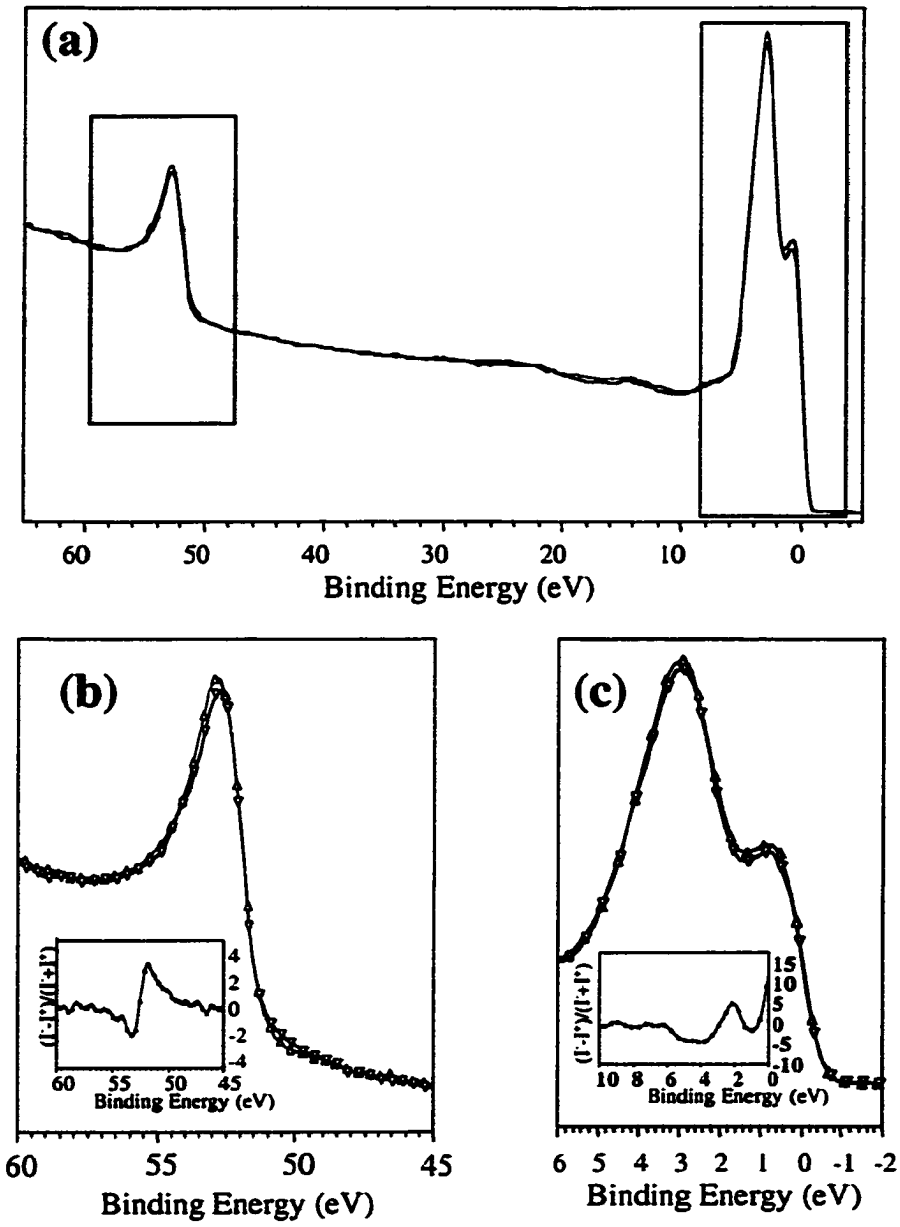

Figure 5.6 (a) EDC's with linearly-polarized light in photoemission from 3.7 ML Fe on Cu(001) magnetized in plane at photon energy 165 eV. (b) MLD on Fe 3*p* band, (c) valence band. Inserts in (b) and (c) show corresponding asymmetries.

5.2 High Temperature Oxidation of Iron Films on Cu(001)

For the past several decades the development of microelectronics has closely paralleled progress in the field of material research.[26] The converse is also true: the demand for new devices drives the search for materials with specific properties, such as spin-polarized conductivity. Magnetite (Fe_3O_4) appears to be a material with this special property. Theoretical computation of the density of states (DOS) in magnetite predicts only minority spin states at the Fermi level.[28] Spin-resolved measurements of secondary photoelectrons performed on single crystal samples demonstrates strong spin polarization of the states near E_F.[29] Based on these observations Fe_3O_4 appear to be half-metallic rather than Mott-Hubbard insulators.

In the Fe-film overlayers studied here, there are interesting *fcc*-to-*bcc* structural transitions as discussed elsewhere.[31, 84] In this section however, we will focus on the oxidation of these films on Cu(001) at elevated temperatures.

A high purity (99.99%) Cu(001) substrate was initially prepared by mechanical polishing followed by electrochemical polishing. Cycles of Ar^+-sputtering and annealing at 825K in ultrahigh vacuum (base pressure of 1×10^{-10} Torr) ensured that we had a clean and well-ordered Cu(001) surface as evidenced by strong surface states in photoemission, and a good 1×1 low energy electron diffraction (LEED) pattern. Previous scanning tunneling microscopy (STM) measurements showed that the surface had primarily single-atomic height steps and uniform width terraces. Detailed description of the sample preparation presented in Appendix A1.

Fe films were deposited *in-situ* using a liquid-nitrogen-cooled electron-beam evaporator. The Fe flux was measured using a quartz crystal oscillator and the rate was stabilized during deposition by monitoring the ion current to the substrate. The film thickness was established by comparing the attenuation of the Cu 3*d* bands and

the growth of the Fe 3*d* bands at the Fermi surface. Oxidation of the Fe films was achieved by heating (electron bombardment from the back of the sample) to 810-840K in a 10^{-6} Torr oxygen ambient for 5 minutes. The sample was then slowly cooled to 525 K in oxygen, at which point the oxygen was pumped out and the heating source was turned off. STM images show two different iron oxide phases, depending on initial Fe coverage. Combining LEED and STM data with a structural model allowed the identification of the oxide.[27]

STM images were taken of submonolayer to multilayer Fe on Cu(001) oxidized at room temperature (300K) as well as at elevated temperatures (810K) to show the dependence of oxide formation on initial Fe coverage.[85]

According to Lozzi *et al.*, the room temperature oxidation of iron films on Cu(001) with 0.5 to 10 ML initial Fe coverage always produces Fe_2O_3.[86] The STM results from Fe films oxidized at room temperature show ill defined islands of oxide with fuzzy boundaries indicating poor tunneling and possible charging.[85, 87]

High-temperature oxidation of Fe on Cu(001) gives dramatically different oxide structures. STM and LEED shows that $Fe_{1-x}O(111)$ forms for Fe coverage below 2 ML and that $Fe_3O_4(111)$ forms for thicker initial Fe coverage. The Fe_3O_4 formation is particularly significant since it is one of the few cases (Ritter *et al.*, observed almost identical results on Pt(111) [88]) where a well-ordered oxide is grown on a dissimilar metal substrate without oxidizing the sample as well.

5.2.1 Model of Oxide Growth

Figure 5.7 (a) shows that for less than 2 ML initial Fe coverage the oxide formed grows in long islands, whose long axes are oriented along the [110] and [1$\bar{1}$0] directions. There is also a substructure in the islands consisting of evenly spaced dark stripes parallel to the long axes of the oxide strip with a separation of ~360 Å. These

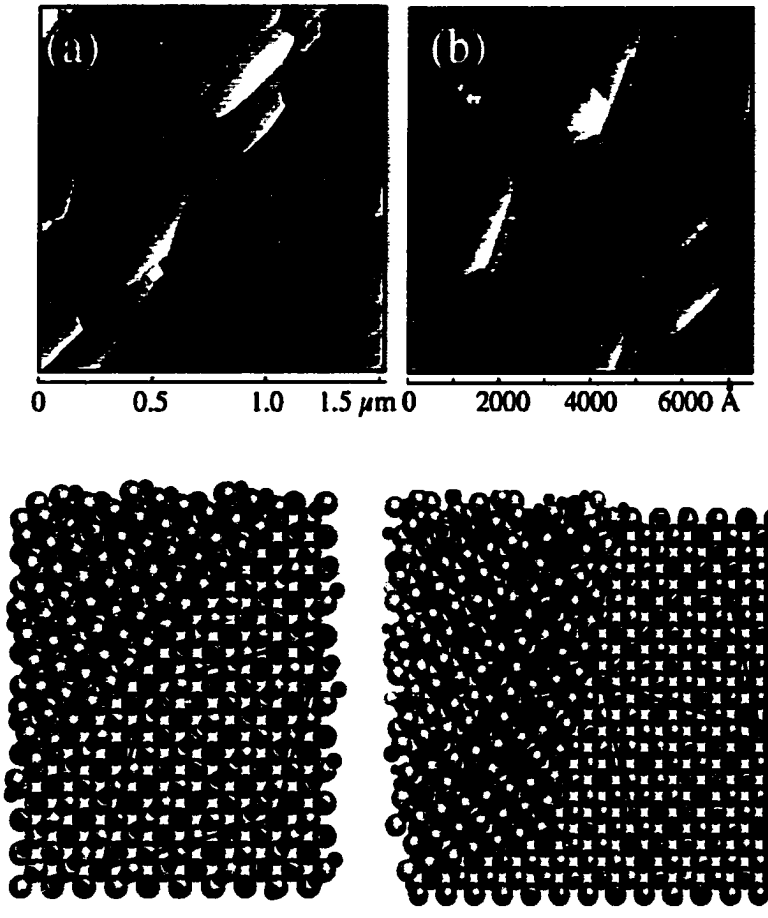

Figure 5.7 STM images of Fe/Cu(001) oxidized at 810 K in 10^{-6} Torr O_2 showing the two phases of oxide that form. (a) < 2ML Fe produces $Fe_{1-x}O(111)$ which grows along Cu[110] and [$\bar{1}$10] directions and (b) 2.5 ML Fe oxidizes to Fe_3O_4 (111) which grows oriented 15° from the [010] direction. (c) A model of $Fe_{1-x}O(111)$ on Cu(001). The *fcc*-Cu(001) is seen below the smaller dark Fe^{2+} layer at the interface. (d) A model of $Fe_3O_4(111)$ on Cu(001). The observed 120°terrace corners correspond to close-packing directions and the island growth is along these directions.

dark regions correspond to anti-phase domain boundaries where strain relief causes a region with different atomic order and tunneling probability.[89] Low energy electron diffraction (LEED) measurements for this film revealed a pattern that is consistent with $Fe_{1-x}O(111)$ and rules out α-$Fe_2O_3(001)$ or $Fe_3O_4(111)$.[27]

When the initial Fe coverage exceeds 2 ML, the resulting oxide films are observed to grow with a second distinct phase as shown in figure 5.7 (b). Although patches of the original oxide phase are still present, the new oxide exhibits well-ordered domains that are clearly distinguishable from the first phase. The long axis is oriented 15° from the [010] substrate azimuth and the islands terminate with mostly 120° corners. Also visible are stripes separated by 170 Å, again attributed to the strain relief at anti-phase domain. Their morphology is distinct from $Fe_{1-x}O$ where the stripes were 360 Å apart. LEED patterns for this oxide phase are consistent with $Fe_3O_4(111)$ and structural models, shown in figure 5.7 (c) and (d), based on the STM observations also suggest that this is the phase formed.[27, 85]

Analysis of both angle integrated and angle-resolved UPS spectra taken at different photon energies gave no evidence of Cu on top of the oxide films.

Since the UPS spectra from CuO(001) [90] are very similar to what we have seen on oxidized Fe/Cu(001) we have taken UPS and XPS data to test for the oxidation of the Cu(001) substrate. The Cu(001) sample was exposed to 1000 Langimouir of oxygen at room temperature and the only observed difference was a substantially reduced surface state intensity. Furthermore we heated the Cu(001) substrate to 810K in 10^{-6} Torr O_2 for 5 minutes, the conditions of oxidation for the Fe overlayers, and no sign of oxidation of the substrate was observed in either the UPS or XPS spectra.

Although some authors have identified the various Fe oxide phases from XPS data and structural information such as LEED and STM [91, 92], a definitive

identification of the oxide phase by core-level analysis is complicated by overlapping features. This is especially troublesome in the presence of multiple oxide phases. The identification is easier using PES from the Fe 3*p* shallow core levels. Such spectra from Fe on Cu(001) as well as oxidized Fe films of different initial thickness obtained with linear polarized light at a photon energy of 165 eV are shown in figure 5.8. The lower curve shows the spectrum from 2 ML Fe on Cu. This curve was fitted by a single Gaussian curve located at 53.1 eV with a full-width half maximum of 2.35 eV. This 3*p* peak is consists of two features – the $3p_{1/2}$ and $3p_{3/2}$ but their small splitting and individual linewidths (short lifetimes) makes them unresolvable.

When 0.5 ML Fe is oxidized this peak shifts by ~2 eV to higher binding energy without a change in the linewith. This observation indicates that only a single oxidation state of iron, namely Fe^{+2}, is present in the sample, and the peak location is comparable to Fe^{+2} positions reported in the literature.[93]

This observation confirms the results of Karunamuni *et al.* [87] on the basis of an STM study conducted in our lab, that suggested the oxidation of < 2ML Fe resulted in the formation of FeO. Furthermore, when thicker Fe films are oxidized, we observe a Fe 3*p* peak that is substantially different. In this case an additional Gaussian located at 57.6 eV is needed for an adequate fit, shown in the top curve in figure 5.8. This second Gaussian implies that there are two different types of Fe cations present in the oxide film. We identify this second peak as being due to Fe^{+3}.

The oxide formed from thicker Fe films contains both Fe^{2+} and Fe^{3+} cations, as does Fe_3O_4. However the ratio of Fe^{+2} to Fe^{+3} oxidation states of iron in our film is 1.56:1 whereas in magnetite (Fe_3O_4) the ratio is 1:2. There are three factors that may contribute to this. First is the coexistence of FeO with Fe_3O_4 which will shift the ratio in favor of Fe^{2+}. Second, for such a thin film, the formation of a magnetite lattice with a limited number of layers may not be complete. This would result in a film not

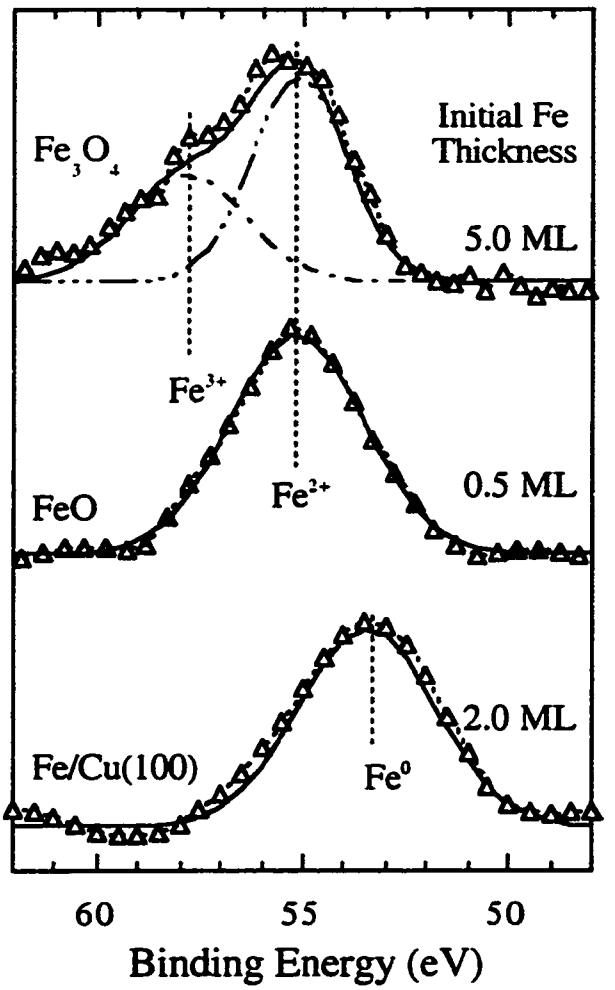

Figure 5.8 PES from Fe 3*p* level at hν = 165 eV reveals chemical shift in Fe 3*p* band due to oxidation and presence of the two different oxidized Fe states.

representative of the bulk. And finally, in our model we expect that Fe atoms at the Fe/Cu interface will have a reduced coordination with oxygen atoms which will make this interface layer completely different from bulk iron oxide.

5.2.2 Resonant Photoemission, Spin Polarization

Figure 5.9 (a) presents a sequence of UPS spectra as a function of photon energy taken on an oxidized Fe film with high initial Fe coverage. Spectra are shown in 2 eV photon energy steps, and they change shape substantially over the photon energy range 49 to 59 eV. This is due to resonant photoabsorbtion in Fe, in which an additional channel for Fe 3*d* emission opens up due to the onset of 3*p* excitations. These 3*p* excitations decay emitting a 3*d* electron, interfering with the direct process, giving a resonant enhancement.

Figure 5.9 (b) shows constant-initial state (CIS) spectra measured across the Fe 3*p* resonance near 54 eV as well as the similar resonant channel in Cu at 72 eV. The top most curve shows the integral of photoelectron current in the binding energy range from -1 to 15 eV as a function of photon energy, following the approach of Lad and Henrich.[94]. Strong Fe resonant enhancement is observed in all three curves. The Cu resonance is the strongest in 2.5 eV binding energy curve which is centered on the 3*d*-bands of Cu. The CIS taken close to E_F exhibits a strong Fe resonance and almost no Cu resonance, indicating that the DOS close to Fermi level is almost entirely derived from iron oxide states.

Figure 5.10 illustrates the presence of bare Cu patches on the surface even after a relatively thick film of ~10 ML Fe film was oxidized. Panel (a) shows resonant features in PES from clean Cu(111). Dashed lines, drawn to guide the eye, show two Auger like features, characterized by a constant kinetic energy and two satellite peaks,

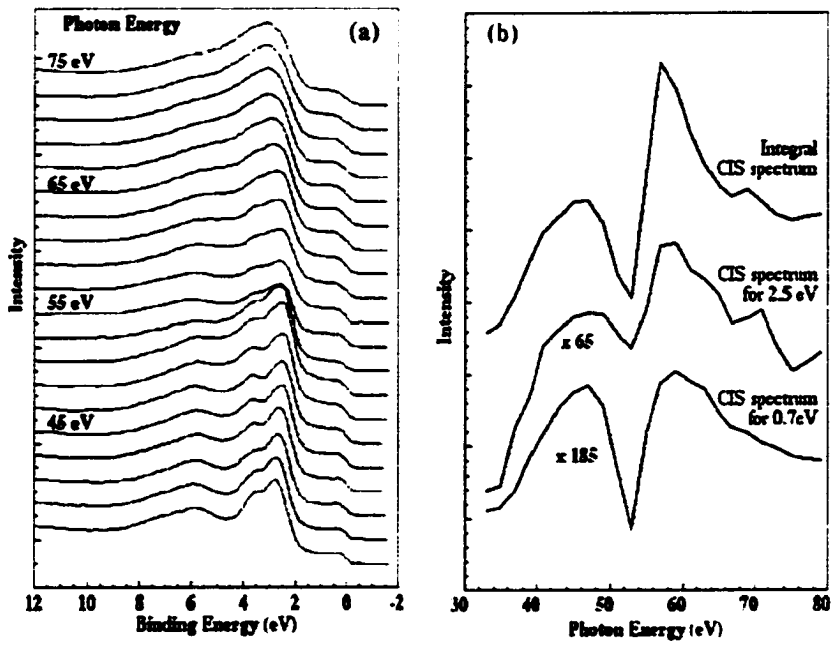

Figure 5.9 (a) EDC's of ~ 2.1 ML oxidized Fe/Cu(001) at different photon energies exhibiting a resonant enhancement between hν = 50 and hν = 60 eV. (b) Constant-initial state (CIS) spectra for the same film. The 0.7 eV spectrum, close to the Fermi level shows a strong Fe resonance but no resonance due to Cu which occurs at ~72 eV.

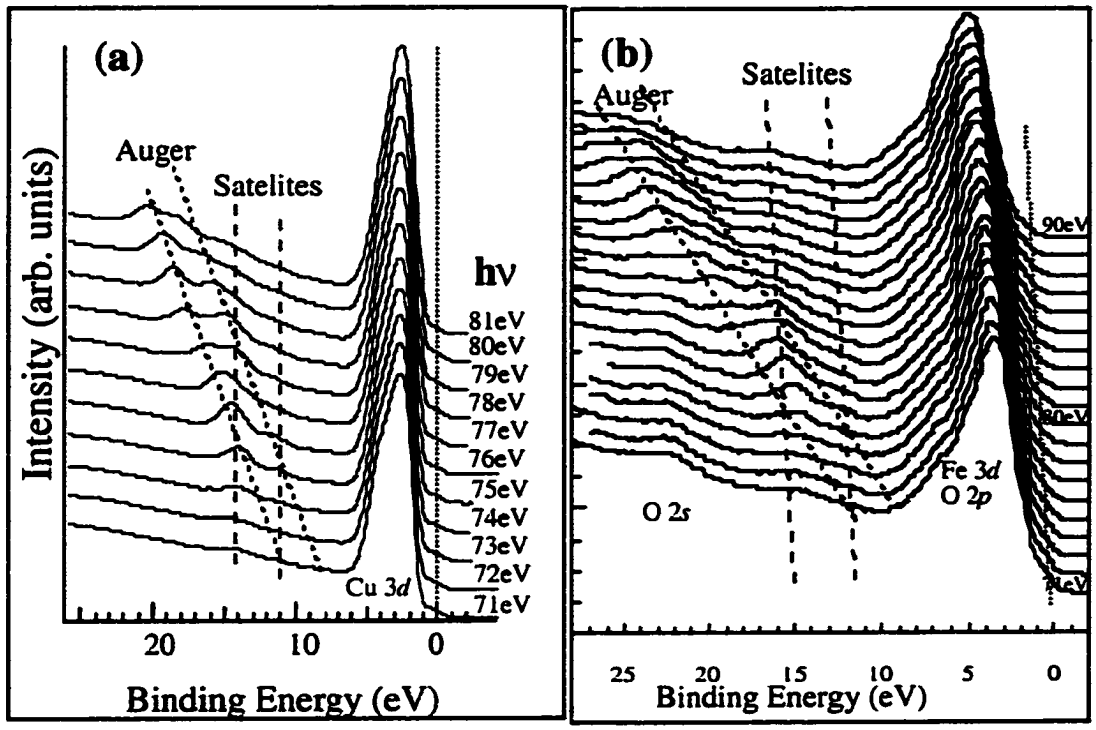

Figure 5.10 Resonant PES from (a) clean Cu surface, and (b) from 10 ML Fe/Cu(100) oxidized at 10^{-6} Torr O_2 ambient and 930 K.

characterized by a constant binding energy. The same features are observed in PES from 10ML Fe/Cu(001) after oxidation at elevated temperature, as shown in (b).

The main questions concerning the oxidized Fe films is whether the sample is magnetic and what the is nature of the DOS close to the Fermi edge, i.e. is it metallic or semiconducting? For this purpose we have performed number of experiments using MCD/MLD, and the results are shown in figure 5.11. A strong asymmetry in the valence band photoemission is observed upon reversal of the chirality of the circularly polarized light from an oxidized 5 ML Fe/Cu(001). This sample was oxidized at a 100K higher than usual temperature resulting in a higher contribution of Cu 3*d* bands to spectrum and a more defined O 2*p* peak. This may suggest a shift towards the formation of FeO. Both 30 and 45 eV photons cause strong asymmetry and suggest spin polarization at the Fermi level. This film was not magnetized, so the only reason for magnetic asymmetry would be remnant magnetization. These data should be treated carefully because of big differences in PE intensities for opposite chirality before normalization. This is an indicative that degree of circularly polarized photons is different for LCP and RCP photons.

In order to verify the strong asymmetry in the valence band, an additional experiment with a 6.1ML Fe/Cu(001) film was performed. This film was oxidized at 840K and after cooling down to room temperature it was magnetized in-plane in the direction perpendicular to the reaction plane. Figure 5.12 (a) shows MLD in angle integrated photoemission from the valence bands at photon energy of 45 eV. The solid and dotted lines show spectra taken for opposite magnetization. The shape of the PE spectra differs from figure 5.11, oxidation at 920K, and from the bulk oxide spectra.[94] One can see features similar to those previously observed: a peak at a binding energy ~0.7 eV characteristic for Fe_3O_4, a Cu 3d band, and a diffuse poorly resolved O 2*p* valence band. The latter suggests the presence of multiple oxide

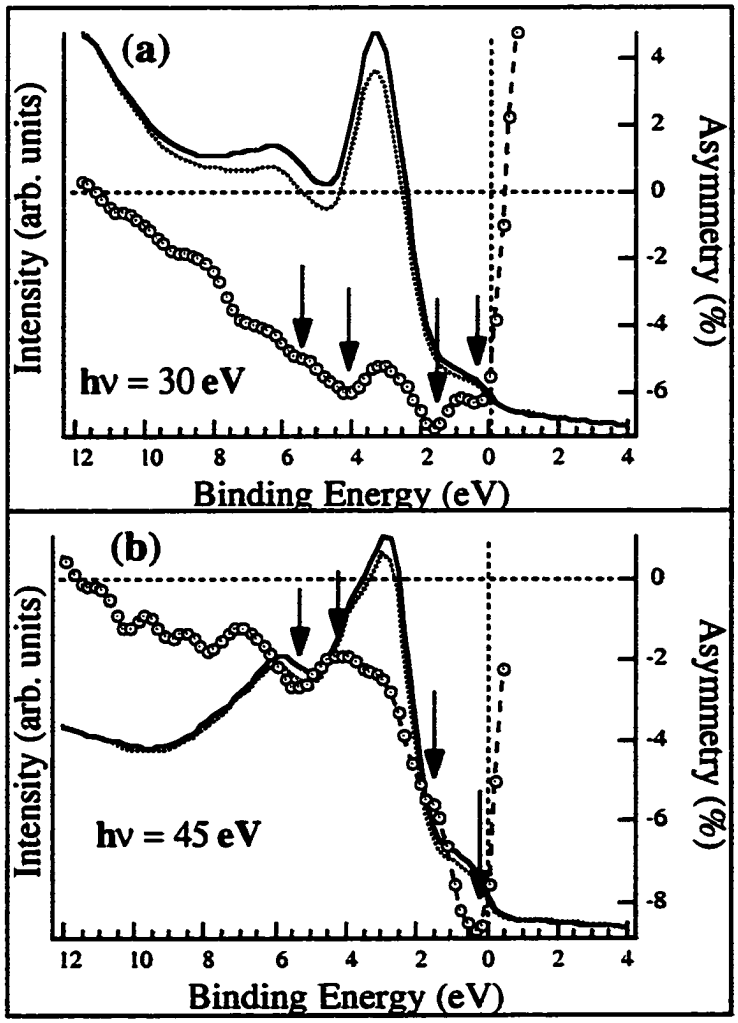

Figure 5.11 Magnetic dichroism in angle integrated photoemission from 5 ML Fe/Cu(100) oxidized at 920 K in 10^{-6} Torr O_2 ambient. (a) Photon energy 30 eV. Solid and dotted lines correspond to EDC's taken with circularly polarized light of opposite chirality. (b) hν = 45 eV.

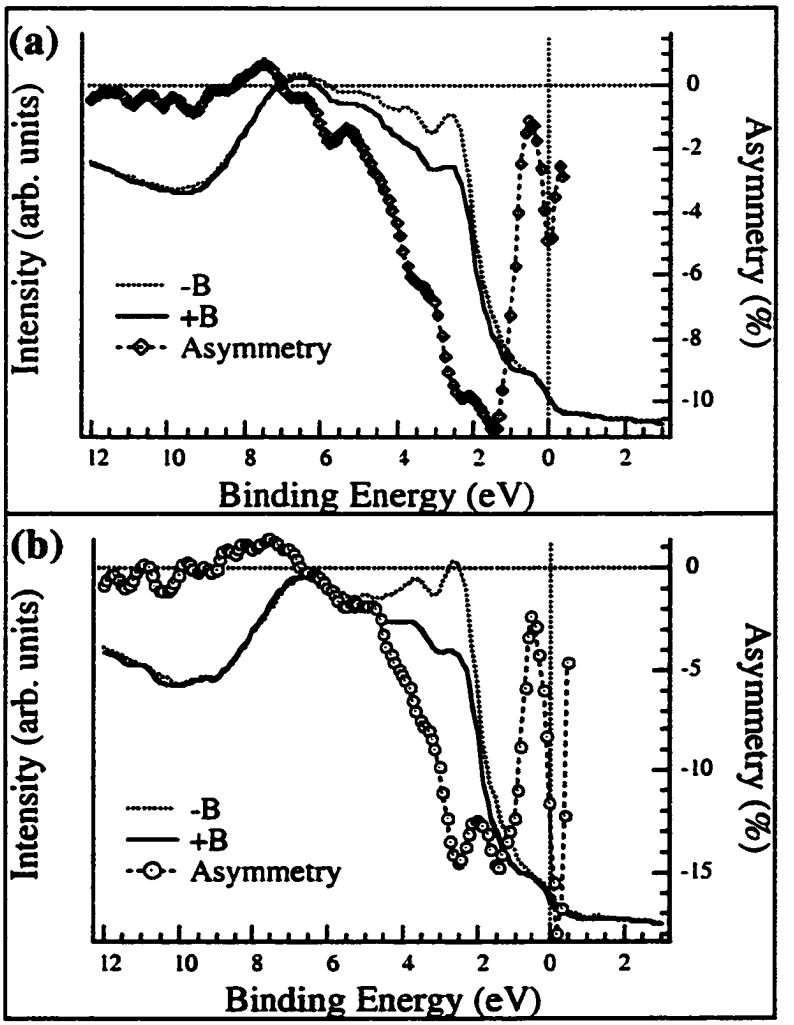

Figure 5.12 Magnetic dichroism in angle integrated PES at hν=45 eV. Sample, 6.1 ML Fe/Cu(100) oxidized at 840 K in 10^{-6} Torr O_2 ambient, magnetized in plane. (a) PE spectra taken with linear polarized light, (b) circular polarized light.

phases. There is a visible spin polarization at the Fermi level. Panel (b) show the photoemission spectra obtained from the same film but with circularly polarized light. Both MLD and MCD indicate asymmetry at the Fermi edge. Figure 5.13 shows another set of data for the same film but at photon energy 60 eV. Even though the shape of the spectra has changed, the overall character of the asymmetry curves remains the same, showing the same features. These data are remarkably consistent with each other and with theoretically predicted DOS.[28] However, direct spin-resolved photoemission measurements are needed to evaluate the spin polarization of these states more precisely.

5.3 Conclusions

The thickness-dependent structural and magnetic changes observed in ultrathin Fe films deposited on Cu(100), pushed us to investigate the nature of the electronic structure within these thickness ranges.

In order to explore the differences between face-centered tetragonal (*fct*) (< 5ML) and *fcc* (5ML–11ML) Fe films on Cu(100), we made use of valence band photoemission. Since the valence electronic band structure depends on the atomic volume, we expect to observe a change in the photoemission spectra and Fermi surface contours as a function of film thickness as we go through the 5 ML transition. Angle–integrated photoemission curves for varying thicknesses of Fe/Cu(100) taken with hν = 90eV, showed differences in the bands for thin (< 5ML) and thick (5 - 11 ML) films.

Further analysis, using difference spectra (Fe/Cu signal minus Cu signal) between a thick and thin film revealed some interesting results. The difference curves effectively provide a spectrum of the Fe-induced changes in the surface density of states (DOS). The spectra for thicker films were consistent with a *fcc*-like electronic

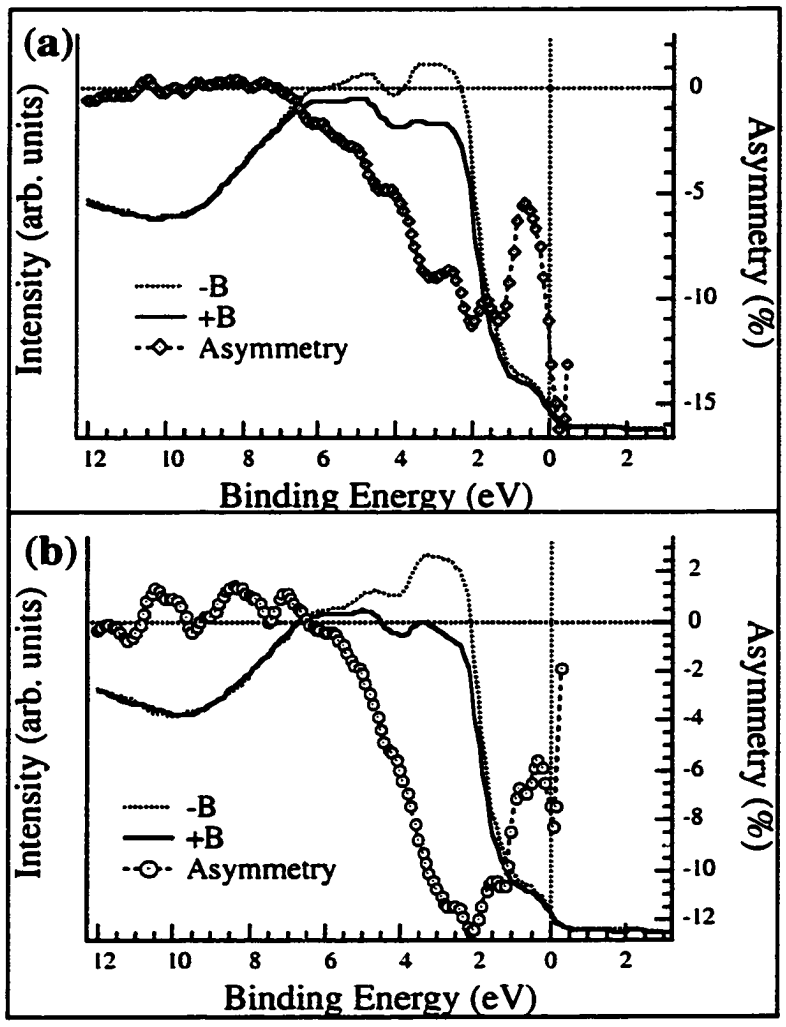

Figure 5.13 Magnetic dichroism in angle integrated PES at hv=60 eV. Sample, 6.1 ML Fe/Cu(100) oxidized at 840 K in 10^{-6} Torr O_2 ambient, magnetized in plane.
(a) PE spectra taken with linear polarized light,
(b) circular polarized light.

DOS. However, the curves for thinner films were unlike both *fcc* and *fct* Fe. To better understand the difference spectra of these Fe/Cu(100) films, band structure calculations were performed in collaboration with Chris Harwell and Randall Hall from the LSU Chemistry department.[84] Wien97 calculations, using bulk ferromagnetic (FM) *fcc*, *fct* and *bcc* parameters, showed that although the DOS within the bands vary, neither the bandwidth nor the location of the bottom of the *d*-band is significantly different for FM *fcc* Fe compared with FM *bcc* Fe. Magnetic dichroism in transverse geometry with LPL indicates presence of in-plane component of magnetization for films with thickness below 5 ML.

Additional information on the electronic changes that are occurring can be extracted from measurements of Fermi surface contours as a function of film thickness. Fermi surface images from *fct* Fe films with thicknesses below 5 ML showed distinct features in the [100] directions. For thicker films (> 5ML), these local intensity maxima appear to be *rotated by 45°*. The theoretical contours calculated using the WIEN code suggest that a rotation of intensity maxima can be associated with a structural change. Nevertheless, diffuse low-quality images for coverage below 5 ML indicate the absence of good long order in this film. Furthermore, expansive stress with the larger underlying substrate lattice is likely to cause surface relaxation with increased numbers of defect sites.

Using synchrotron light at hν = 165 eV we probed the shallow 3*p* core levels. The peak for Fe/Cu(100) was located at 53.1 eV and was fitted with a single Gaussian consistent with a single, metallic Fe^{o} state. When ultrathin Fe (< 2ML) was oxidized, the 3*p* peak shifted by 2 eV to higher binding energy. It was also fitted with a single Gaussian and the 2eV shift is consistent with an Fe^{+2} state. However, for thicker oxidized Fe films, the Fe 3*p* level broadened substantially and an additional Gaussian peak was needed for an adequate fit. This second Gaussian implies that a second Fe

valence state is present in the oxide film. The oxide formed from thicker Fe films contains both Fe^{+2} and Fe^{+3} species, as does Fe_3O_4. We found that the ratio of Fe^{+2}/Fe^{+3} was almost inverted from the expected 1:2 ratio for stoichiometric Fe_3O_4. This ratio is consistent with presence of undercoordinated Fe at Fe/Cu interface, a model which was previously proposed by Karunamuni based on STM results. Although there have been several published papers showing the valence bands of various Fe oxides, the details of the spectra have been difficult to duplicate, even with single-crystal materials. In part, this is due to the different potential reconstructions that can occur when surfaces are prepared in uhv. It is not surprising that our data look unlike prior reported spectra. In part this is expected since we are dealing with ultra-thin oxides where the interfacial Fe is not completely oxidized.

We have observed that the DOS from oxidized films close to the Fermi edge is higher that observed from bulk oxides. This is a particularly interesting result since it may be a useful means for coupling spin-polarized carriers from one film to another. Recent work has suggested that the behavior of Fe_3O_4 films in tunnel magneto-resistive devices is highly dependent on the conditions at the film's interface, and most departures from stoichiometry result in a loss of half-metallic behavior. Our resonant photoemission CIS data show that the enhanced DOS at the Fermi level is associated with Fe atoms and not from the Cu substrate.

Magnetic dichroism experiments in the transverse geometry from in plane magnetized oxide films studied with both LPL and CPL indicate presence of a surface magnetic moment and a certain degree of spin polarization at Fermi edge, which is consistent with theoretical expectations.

Chapter 6

Summary

The research reported here is a study of the electronic and magnetic properties of ultrathin films grown epitaxially on Cu. The films that we chose to study are important for three reasons. First, they are all model systems for evaluating the changes in electronic structure when these materials are synthesized in ultra-thin form. Secondly, some of these films are important in the magnetic recording industry, such as Co/Cu which is currently used in magnetic disk sensors. Finally, we have also studied materials that have the potential for spin-dependent transport. These materials are needed for further development of the nascent field of *spintronics*.

We have used synchrotron radiation in both the UV and soft X-ray ranges to perform photoelectron emission experiments, allowing us to extract information on the electronic structures of these materials. Specialized techniques such as resonant photoemission and magnetic linear/circular dichroism were used to obtain additional information about their electronic and magnetic properties.

The evolution of the electronic structure of *fcc* Co films grown on Cu(001) was studied by monitoring the angular distributions of photoemitted electrons. By changing the initial-state, the band structure was monitored and the behavior of this electronic structure was observed in different parts of the Brillouin zone by changing the photon energy, thereby accessing different **k** values. The symmetries of the initial states responsible for pattern formation in angular distributions were identified in some cases.

To the best knowledge of the author although studies have been made in normal emission geometries, there have been no prior studies on magnetic dichroism in angle integrated valence band photoemission. Furthermore, our imaging

experiments have provided a wealth of new information on the dichroism that occurs in a broad range of low-symmetry directions in the Brillouin zone. In this sense the present work is pioneering because we have obtained new valence band information on MLD/MCD from ultrathin films of Co on Cu(001) and (111) substrates. Furthermore, the relationship between different implementations of magnetic dichroism effects was explored for films of C_{4v} and C_{3v} point-group symmetries on (001) and (111) surfaces respectively.

In the MCD experiment on Co/Cu(001), it was shown that when the magnetization vector $\vec{M}$ lies in the reaction plane of the incident light for a C_{4v} surface, and this plane coincides with a mirror plane of the crystal, the effects of magnetization reversal and light helicity reversal are not identical. This is due to the fact that, for our experimental geometry, the helicity reversal using this technique also gives rise to an MLD term in dichroism.[20] The MCD asymmetry strongly depends on the experiment configuration. For CP light, $h\nu = 45$ eV, the maximum asymmetry in the longitudinal configuration is 3.5 times that for the transverse geometry. This ratio also strongly depends on the photon energy. For linearly polarized light, $h\nu = 21$ eV, the ratio of the asymmetry in the longitudinal geometry versus that in the transverse is close to 2.

A number of images of MCD/MLD asymmetries in photoelectron angular distributions (MCDAD/MLDAD) were presented for valence band photoemission at $h\nu = 21$ eV. The symmetry of these images was interpreted in terms of the mutual orientation of the $\vec{M}$ and $\vec{P}$ vectors. The images of the angular distributions also show asymmetries for Co/Cu(001) and Co/Cu(111) that depend on the initial state binding energy.

The magnetic dichroism asymmetries in angle integrated photoemission from the 3*p* shallow core levels of in-plane magnetized Co/Cu(111) in a transverse

geometry both for CP and LP light have similar shapes and magnitudes, which indicates that the dichroism in this case depends only on magnetization reversal and not on the character of light polarization. As mentioned above, this is not the case in the valence band photoemission. In the case of Co/Cu(111), it was shown that the MLD effect which is due to reversal of magnetization for in-plane magnetized Co film and the LD effect which is due to the fact that the reaction plane is not a mirror plane for (111) surface in our experimental geometry can be decoupled. The maximum value of asymmetry in the case of magnetization reversal obtained by rotating the sample 180° around the surface normal is factor of 2 larger than the asymmetry obtained by changing the sample magnetization reversing the direction of applied external magnetic field.

Residual gas exposure can have some effect on valence band photoemission and intensities and this was studied to some degree. Physically adsorbed molecules of CO and H_2O were found to not affect the magnetization of the sample, consistent with MXCD and MOKE measurements by other groups. However, these molecules can affect the overall intensities of the photoelectron angular distributions. Therefore, this effect should be taken into consideration while dealing with valence band photoemission.

Fe/Cu(001) films in coverages below 5 ML gave Fermi surface contours that are significantly different from the Fermi surface contours for coverages higher than 5 ML. These changes can not be explained from the "traditional" point of view on the magnetic and structural phases of ultrathin Fe films on Cu(001).[30, 32, 80] In that model, MBE grown Fe/Cu(001) below ~5 ML forms ferromagnetic tetragonally distorted *fcc* phase (*fct*) with out-of-plane magnetic moment. Around 5 ML, films undergo *fct* to *fcc* transition with the magnetization remaining out-of-plane with reduced value of the net magnetic moment due to AFM alignment of local magnetic

moments between layers. Above 10-12 ML films transform to (110) face of *bcc*-Fe, with in-plane magnetic moment. Recent atomically resolved STM data for ultrathin Fe/Cu(001), however, indicate the presence of a *bcc* tetragonally distorted phase of Fe at low coverages.[83] Our experimental data in angular distributions from the Fermi edge show that at low coverage (near 5 ML) the FS contours can not be satisfactory explained neither by *fcc* (*fct*) nor by *bcc*. This is a result of strong surface relaxation and the lack of perfect long range order.

This thesis also reports the results of study of the high temperature oxidation of Fe/Cu. We were able to produce extremely well-ordered oxide patches grown on a metallic surface without oxidizing the Cu substrate. One of the oxides formed during this investigation is Fe_3O_4, which is a magnetic material predicted to provide carriers of only one spin orientation. This is a useful step in the effort to develop microelectronic devices such as magnetic RAM and more sensitive computer disk head sensors based on spin-dependent transport. Cu is a metal that is compatible with current device components and the growth of an ordered oxide on a Cu substrate make this work applicable to technologically interesting devices.

Combining STM data that gives structural information with PES, we have an opportunity to identify the iron oxide phases. Shallow core-level PES data using the Fe 3*p* peaks indicates that only one oxidation (Fe^{+2}) state of Fe is present for all the oxide films formed with initial thickness below 2ML in agreement with previous STM and LEED experiments which indicated FeO formation. As the initial Fe coverage increases above 2ML, the double Fe 3*p* core-level peaks in photoemission indicate the presence of an extra oxidation state. These two oxidation states (Fe^{+2} and Fe^{+3}) confirm the formation of Fe_3O_4. We found that the ratio of Fe^{+2}/Fe^{+3} was almost inverted from the expected 1:2 ratio for stoichiometric Fe_3O_4. This ratio is consistent

with presence of undercoordinated Fe at Fe/Cu interface, a model which was previously proposed by Karunamuni based on STM results.

Constant initial state (CIS) resonant photoemission data shows that the DOS close to the Fermi edge can be identified as mostly due to iron oxide states, but not due to Cu states. MCD/MLD data suggest a significant degree of spin polarization at the Fermi edge and the presence of a surface magnetization for these films. A direct method of measuring the spin-polarized fraction, such as spin-resolved photoemission or Andreev scattering on the *in-situ* prepared surface may help to obtain an unambiguous answer to this problem.

The best direction for the future development of the study of these magnetic structures lies in spin-resolved band mapping and magnetic dichroism in spin-resolved photoemission. The future studies of MCD/MLD in angular distributions will benefit from instrumentation improvement, which can be done by increasing the energy range of the beamline to span the $2p$ levels of the $3d$ transition metals and improving the angular resolution of the detector. A "thinner" design of the micro-rotational stage will result in a better positioning of the sample at the focal point inside the EMA, which will provide higher quality images of angular distributions. Among the future subjects for studies I would mentioned chrome oxide (CrO_2), which is another candidate for spin-polarized conductivity. Another possible direction of the studies is a tunneling magnetoresistance (TMR) of ultrathin, ~10 Å, insulating oxide films on a magnetic substrate.

References

1. M.N. Baibich, *et al.*, *Phys. Rev. Lett.* **61**, 2472 (1988).
2. D.M.C. Nicholson, *et al.*, *J. Appl. Phys.* **76**, 6805 (1994).
3. J.M. MacLaren and R.H. Victora, *Appl. Phys. Lett.* **66**, 3377 (1995).
4. J. A. C. Bland and B. Heinrich , Eds., *Ultrathin Magnetic Structures* , Springer-Verlag, , (1994).
5. D. Pescia and V. L. Pokrovsky, *Phys. Rev. Lett.* **65**, 2599 (1990).
6. D. Kerkmann, D. Pescia, R. Allenspach, *Phys. Rev. Lett.* **68**, 686 (1992).
7. N. W. Ashcroft and N. D. Mermin, *Solid State Physics*, Holt, Rinehart and Winston, (1976).
8. S. van Dijeken, PhD dissertation, University of Twente (2000).
9. M. Tischer, *et al*, *Phys. Rev. Lett.* **75**, 1602 (1995).
10. F. Nouvertne, *et al.*, *Phys. Rev. B* **60**, 14382 (1999).
11. F. Nouvertne, *et al.*, *Surf. Sci. Letters* , 653 (1999).
12. U. Ramsperger, A. Vaterlaus, P. Pfaffli, U. Maier and D. Pescia, *Phys. Rev. B* **53**, 8001 (1996).
13. M. Kowalewski, C. M. Schneider and B. Heinrich, *Phys. Rev. B* **47**, 8748 (1993).
14. M. T. Kief and W.F. Egelhoff, *Phys. Rev. B* **47**, 10785 (1993).
15. R. Miranda, D. Chanderesis and J. Lecante, *J. Surf. Sci* , 269 (1983).
16. C. M. Schneider, *et al.*, *J. Phys. C* **3**, 4349 (1991).
17. G. Mankey, PhD dissertation, Pennsylvania State University (1992).
18. M. Hochstrasser, *et al*, *Phys. Rev. B* **60**, 17030 (1999).
19. F. J. Lamelas, *et al.*, *Phys. Rev. B* **40**, 5837 (1989).
20. D. Venus, *Phys. Rev. B* **56**, 2661 (1997).
21. T. Matsushita, *et al.*, *Phys. Rev. B* **56**, 7687 (1997).
22. A. Fanelsa, E. Kisker, J. Henk, and R. Feder, *Phys. Rev. B* **54**, 2922 (1996).
23. C. M. Schneider, U. Pracht, W. Kuch, A. Chasse´and J. Kirschner, *Phys. Rev. B* **54**, 15618 (1996).

24. W. Kuch, *et al.*, *Phys. Rev. B* **57**, 5740 (1998).

25. A. Fanelsa, E. Kisker, J. Henk, and R. Feder, *Phys. Rev. B* **54**, 2922 (1996).

26. G.A. Prinz, *Science* **282**, 1660 (1998).

27. R. Kurtz, J. Karunamuni and R. Stockbauer, *Phys. Rev. B.* **60**, R16 342 (1999).

28. Z. Zhang and S. Satpathy, *Phys. Rev. B* **44**, 13319-13331 (1991).

29. S. F. Alvarado, *et al.*, *Phys. Rev. Lett.* **34**, 319-322 (1975).

30. J. Giergiel, J. Shen, J. Woltersdorf, A. Kirilyuk and J. Kirschner, *Phys. Rev. B* **52**, 8528 (1995).

31. J. Thomassen, *et al.*, *Phys. Rev. Lett.* **69**, 3831 (1992).

32. D. Li, *et al*, *Phys. Rev. Lett.* **72**, 3112 (1994).

33. D. Chambliss and K. E. Johnson, *Surf. Sci.***313**, 215-226 (1994).

34. D. Wang, A. J. Freeman, and H. Krakauer, *Phys. Rev. B* **24**, 1126 (1981).

35. R. L. Stockbauer and A. Pararas, *Nucl. Instrum. Meth. Phys. Res.* **A266**, 560 (1988).

36. R. Stockbauer *et al.*, *Nucl. Instrum. Meth. Phys. Res.* **A291**, 505 (1990).

37. S.D. Kevan, *Angle-Resolved Photoemission:Theory and Current Applications*, vol. 74, ELSEVIER, (1992).

38. D.P. Woodruff and T.A. Delchar, *Modern Techniques of Surface Science*, Cambridge University Press, Cambridge, (1994)

39. C.N. Berglund and W.E. Spicer, *Phys. Rev.*, 1030 (1964).

40. C.N. Berglund and W.E. Spicer, *Phys. Rev.*, 1044 (1964).

41. H. Luth, *Surfaces and Interfaces of Solid Materials*, Springer, ed. 3, (1996).

42. W.E. Spicer, *Phys. Rev.* **112**, 114 (1968).

43. S.D. Kevan, *Phys. Rev. Lett.* **50**, 526 (1983).

44. F.J. Himpsel, *J. Appl. Optics* **19**, 9 (1980).

45. M.P. Seah and W.A. Dench, *Polarized Electrons*, Springer-Verlag, (1976).

46. C. Roth, F. Hillebrecht, H. Rose and E. Kisker, *Phys. Rev. Lett.* **70**, 3479 (1993).

47. J.G. Tobin, *et al.*, *J. Appl. Phys.* **79**, 5626 (1996).

48. F.U. Hillebrecht, *et al.*, *Phys. Rev. Lett.* **75**, 2224 (1995).

49. J. Henk, S.V. Halilov, T. Scheunemann and R.Feder, *Phys. Rev. B* **50**, 8130 (1994).

50. T. Scheunemann, S.V. Halilov, J. Henk and R.Feder,, *Solid State Commun.* **91**, 487 (1994).

51. G. van der Laan, *et al.*, *Phys. Rev. B* **34**, 6259 (1986).

52. F. U. Hillebrecht, *et al.*, *Phys. Rev. Lett.* **75**, 2883 (1995).

53. G. van der Laan, *Phys. Rev. B* **51**, 51 (1995).

54. W. Kuch, *et al.*, *Phys. Rev. B* **53**, 11621 (1996).

55. J. Henk and B. Johansson, *J. Electron Spec.* , 259 (1998).

56. E. Morikawa, *et al.*, *Rev. Sci. Instrum.* **63**, 1300 (1992).

57. Z. Qu, *et al.*, *Nucl. Instrum. Methods Phys. Res. A* **347**, 299 (1994).

58. Z. Qu, *et al.*, *Surf. Sci.* **324**, 133 (1995).

59. K. Subramanian, PhD dissertation, Louisiana State U. (1997).

60. J. Hermanson, *Solid State Commun.* **22**, 9 (1977).

61. R. Courths and S Hufner, *Physics Reports* **112**, 53-171 (1984).

62. J.H. Weaver, *Phys. Rev. B* **19**, 3850 (1979).

63. J. Barth, F. Gerken, and C. Kunz, *Phys. Rev. B* **31**, 2022 (1985).

64. G. Mankey, *et al.*, *Phys. Rev. Lett.* **78**, 1146 (1996).

65. F.M. de Groot, J.C. Fuggle, B.T. Thole and G.A. Sawatsky, *Phys. Rev. B* **42**, 5459 (1990).

66. C. T. Chen,, *et al.*, *Phys. Rev. Lett.* **75**, 152 (1995).

67. J. G. Menchero, *Phys. Rev. Lett.* **76**, 3208 (1996).

68. M. Finazzi, G. Ghiringhelli, O. Tjernberg, and N. B. Brookes, *J. Phys.: Condens. Matter* , 2123 (2000).

69. J.G. Tobin, *et al.*, *Surf. Sci. Lett.* , L227 (1998).

70. G. van der Laan and B.T. Tobin, *Solid State Commun.* **92**, 427 (1994).

71. B.T. Thole and G. van der Laan, *Phys. Rev. B* **49**, 9613 (1994).

72. N. Mainkar, PhD dissertation, Louisiana State U. (1996).

73. N. Smith, *Physics Today* **54**, 29 (2001).

74. P. Blaha, K. Schwarz and J. Luitz, *FPLAPW packageWIEN'97*, Vienna University of Technology, (1997).

75. T.J. Kreutz, T. Greber, P. Aebi and J. Osterwalder,J., *Phys. Rev. B* **58**, 1300 (1998).

76. E.W. Plummer and W. Eberhardt, Eds., *Angle-resolved photoemission as a tool for the study of surfaces*, vol. XLIX, John Wiley & Sons, (1982).

77. X. Gao, *Private Communication*, (2000).

78. G.J. Mankey, R.F. Willis and F.J. Himpsel, *Phys. Rev. B* **48**, 10284 (1993).

79. S.E. Greco, J.P. Roux and J.M. Blakely, *Surf. Sci.***120**, 203 (1982).

80. D. Li, *et al., Surf. Sci.***264**, 406 (1992).

81. D.Bagayoko and J. Callaway, *Phys. Rev. B* **28**, 5419 (1983).

82. J. Asada and S. Blugel, *Phys. Rev. Lett.* **79**, 507 (1997).

83. A. Biedermann, M. Schmid and P. Varga, *Phys. Rev. Lett.* **86**, 464 (2001).

84. R. H. Madjoe, *et al., J. Appl. Phys.*, **85**, 6211 (1999).

85. J. Karunamuni, R. Kurtz and R. Stockbauer, *Surf. Sci.***442**, 223 (1999).

86. L. Lozzi, *et al., Surf. Sci.* **331-333**, 703 (1995).

87. J. Karanamuni, PhD dissertation, Louisiana State University (1999).

88. M. Ritter, H. Over and W. Weiss, *Surf. Sci.***371**, 245 (1997).

89. D.T. Margulies, *et al., Phys. Rev. Lett.* **79**, 5162 (1997).

90. S. Warren, *et al., J. Phys.: Condens. Matter* **11**, 5021 (1999).

91. J.F. Andrson, *et al., Surf. Sci.* **373**, 85. (1997).

92. Th. Schedel-Niedrig, W. Weiss and R. Schlogl, *Phys. Rev. B* **52**, 17449 (1995).

93. H. Kim, J. Park and E.Vescovo, *Phys. Rev. B.* **61**, 15 288 (2000).

94. R.J. Lad and V.E. Henrich, *J. Vac. Sci. Technol. A* **7**, 11893 (1989).

95. G.J. Mankey, M.T. Kief, F. Huang and R.F. Willis, *J. Vac. Sci. Technol. A* **11**, 2034 (1993).

96. M.P. Seah and W.A. Dench, *Surface and Interface analysis* **1**, 2 (1979).

Appendix

Sample preparation procedures

A1 Cu(001) and Cu(111)

The Cu(001) and Cu(111) substrates were obtained commercially from the '*Monocrystals*' Company. Initially they were used "as received" but after many cycles of film growth and cleaning, there was a need for repolishing. The Cu substrate was then prepared by mechanical polishing to 0.1 μm with diamond paste. The final delicate stage of mechanical polishing (0.05μm grit alumina) was followed by electropolishing in a solution of 25% hydrochloric acid and 75% phosphoric acid.[78] The crystal, suspended on pure Cu holder, serves as the anode (+), while a another Cu plate serves as the cathode (-). The electropolishing is performed for 50 - 60 seconds at a voltage of 2.1V and then thoroughly rinsed with distilled water. This helps to restore the bright copper color of the crystal surface, which turns milky due to roughening.

Cycles of Ar^+-sputtering and annealing at 600°C in ultrahigh vacuum (base pressure of 1 x 10^{-9}Torr) ensured that we had a clean and well-ordered Cu surface as evidenced by photoemission. The cleanliness of the surface was confirmed by scanning tunneling microscopy measurements that were also performed in our laboratory. Typically, the crystals were sputtered for ~30 minutes with Ar^+ ions at a pressure of $5x10^{-5}$ Torr.[95] This technique cleans the surface of adsorbed contaminants and any previously deposited film. A sputtered surface, however, is not smooth on the atomic level as shown in STM studies previously conducted in our lab by Karunamuni and reproduced in Fig. A1.1.[87] The STM images of a Cu surface after sputtering are shown in A.1.1.(a) and an image obtained after annealing are

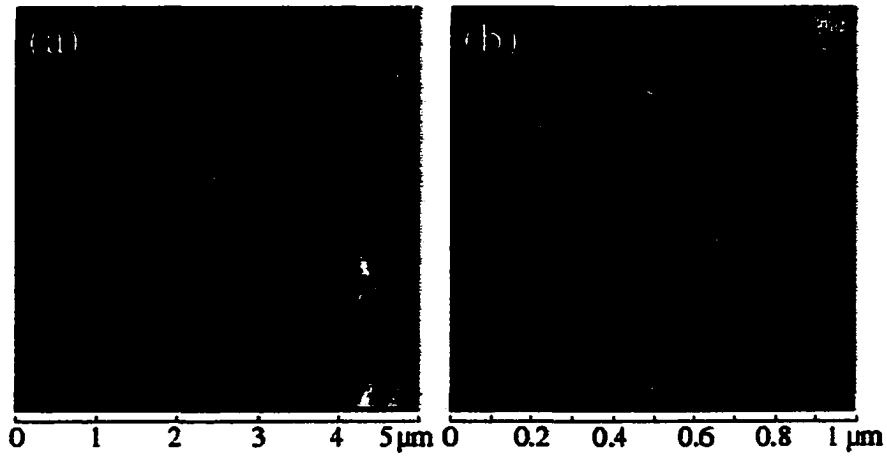

Figure A1.1 STM images of Cu(001) surface after various stages of sample preparation. (a) An image of Cu(001) that has been bombarded with 500 eV Ar^+-ions; the deepest pits are ~350Å deep. (b) After annealing at 600°C the surface exhibits atomically flat Cu terraces with monoatomic steps.

shown in figure A1.1(b). The latter surface had been annealed for ~10 minutes at ~600°C which increases the mobility of the atoms on the surface and redistributes the atoms to render a flat surface with monoatomic steps and terraces many microns wide.

A2. Thin Film Growth on Cu(001)

The Fe and Co thin films were grown in ultra-high vacuum by molecular beam epitaxy (MBE) from an e-beam heated wire source. The schematic cross-section of the source is presented in figure A2.1. A high purity (99.99%) Fe(Co) rod Ø=1mm, was placed along the axis of a hollow cylindrical Cu cooling jacket. A circular thoriated W filament was placed close to the tip of the rod, encircling one end. A DC current of ~ 5 - 6 A was passing through the filament to create a flux of thermally emitted electrons at ground potential while the rod was biased by applying +2kV. The tip was heated by radiant heating as well as by the electrons which bombarded the rod. This heating resulted in the evaporation of neutrals and ions from the rod. The fraction of ionized particles is less then 1/1000. A collimating aperture was used to produce a beam of particles directed at the substrate. The Cu cooling jacket and aperture were cooled using flowing liquid nitrogen to keep the pressure in the chamber from increasing during deposition. Typical evaporation rates were ~1-5 ML per minute with chamber pressure rising to the mid 10^{-9} Torr range.

The neutral flux was measured using a quartz crystal oscillator and the rate was stabilized during deposition by monitoring the ion current to the substrate. A constant ion current was assumed to imply a constant neutral flux. The film thickness was established by comparing the attenuation of the Cu 3*p* peaks in photoemission and the growth of the Fe or Co 3*p* peaks, monitored with hν=165 eV. At this kinetic energy, the inelastic mean-free path corresponds to approximately 3 ML.

Oxidation Procedure

The oxidation of Fe films on Cu was accomplished by filling the sample preparation chamber with oxygen to 1×10^{-6} Torr at room temperature and

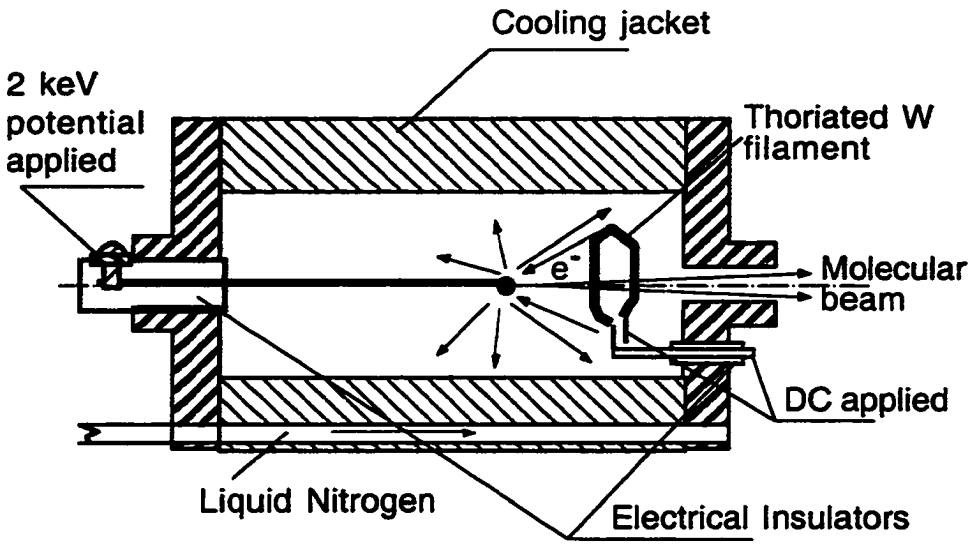

Figure A2.1 Schematic cross-section of an electron beam heated wire MBE source. Thermal electrons from the thoriated W filament accelerated by applied voltage hit the rod of the material to deposit. The tip of the rod melts emitting the flux of neutrals.

simultaneously heating the sample slowly to 810K and holding at this temperature for 3-5 minutes. During the oxidation, the sample puck with the Cu crystal, was heated using electron bombardment by electrons accelerated to ~600eV from the surface of thoriated W filament located behind the puck. The temperature of the filament was electronically stabilized so that the sample temperature could be held constant within ± 2K. After annealing, the sample was then cooled slowly (0.5K/sec) to ~500K, at that point the heating was switched off and the sample was allowed to cool down to the room temperature. During cooling, the oxygen exposure was stopped around 550K and the chamber was pumped out to the pressure of ~1×10^{-9}Torr. To measure the temperature of the sample, a W-5% Re / W-26% Re thermocouple was spot-welded to the post near where the sample puck was held.

A3. Thickness Measurement: Attenuation of 3*p* Core Levels

During deposition, the ion current to the substrate was monitored and was observed to be ~1 nA. The product of the evaporation time and this ion current was used as a rough indicator of the film thickness. We also mounted a quartz crystal oscillator to measure evaporation rates. Core level spectra of the overlayer and substrate were used to determine the film thicknesses. As the film thickness increases, the intensity of the substrate peak decreases as the photoemitted electrons are attenuated by the overlayer. The ratio of the intensities of the corresponding overlayer core level peaks to those of the substrate can be used to estimate the film thickness.

Let I_{Co} and I_{Cu} be the intensities of the Co and Cu core level peaks respectively. Then

$$I_{Cu} = Io_{Cu} e^{-d/\lambda} \qquad \text{(A3.1)}$$

where I_O is the total photoemission intensity, d is the film thickness and λ is the inelastic mean free path in Co. This is just Beer's law. Correspondingly, I_{Co} is given by

$$I_{Co} = Io_{Co}(1 - e^{-d/\lambda}) \qquad \text{(A3.2)}$$

where we have used the same mean-free path since, for the kinetic energies used, the mean-free paths for the two core levels are approximately the same. Solving for d from the above two equations gives

$$d = \lambda \ln\left[1 + \frac{(I_{Co} / Io_{Co})}{(I_{Cu} / Io_{Cu})}\right] \approx \lambda \ln\left[1 + \frac{I_{Co}}{I_{Cu}}\right] \qquad \text{(A3.3)}$$

where the approximation arises from the assumption of similar cross-sections for the 3*p* levels from transition elements nearby in the periodic table. The thicknesses may be estimated from the ratio of the peak intensities from the core level spectra, provided

the value λ, the inelastic mean free path is known. The electron inelastic mean free path (IMFP) in solids fall on a so-called universal curve, roughly independent of the material.[96] It depends only on the electron's kinetic energy and has a minimum of 3 - 5 Å. For electrons of ~100 eV kinetic energy, $\lambda \sim 5.6$ angstroms which translates to about 2.7 ML for the system of interest.

Vita

Alexey Koveshnikov was born on November 13, 1964, in Bukhara, Uzbekistan, to Nikolai and Nadezhda Koveshnikov. Graduating from the Secondary School #142 in Kiev, Ukraine, he attended Moscow Institute of Physics and Technology, Russia, and graduated with Higher Education Diploma (equivalent to a master's degree) in physics and electrical engineering in July of 1988.

In the summer of 1988, he began to work as a research associate in the Institute for Surface Chemistry, Ukrainian Academy of Science, Kiev, Ukraine.

In the fall of 1995, he entered Louisiana State University. He began his research in surface science and condensed matter physics under his major professors, Richard L. Kurtz and Roger L. Stockbauer in 1996 and is currently a candidate for the degree of Doctor of Philosophy.

He was married to Irina Knyazeva in October of 1990. They have two sons named Ilya and Daniel Koveshnikov.

He is a member of the American Physical Society and of the American Vacuum Society.

DOCTORAL EXAMINATION AND DISSERTATION REPORT

Candidate: Alexey Koveshnikov

Major Field: Physics

Title of Dissertation: Studies of Ultrathin Magnetic Films Using Synchrotron Radiation: Resonant Photoemission, Circular and Linear Magnetic Dichroism

Approved:

Major Professor and Chairman

Dean of the Graduate School

EXAMINING COMMITTEE:

Date of Examination:

June 6, 2001